Department of Physics and Astronomy
University of Heidelberg

Bachelor Thesis in Physics
submitted by

Barbara Susanne Scherpe

born in Mannheim (Germany)

2016

Determination of the Prompt Fraction of D^0 Mesons in proton-proton Collisions with ALICE at $\sqrt{s} = 7$ TeV

This Bachelor Thesis has been carried out by Barbara Susanne Scherpe at the
Physikalisches Institut of the University of Heidelberg
under the supervision of
PD Dr. Kai Schweda

Abstract

The prompt fraction of D^0 mesons was determined from data recorded with the ALICE detector in proton-proton collisions at $\sqrt{s} = 7$ TeV. The measured raw yields of D^0 mesons contain contributions from both prompt charm production and feeddown from B hadrons. The prompt fraction of D^0 mesons for two data sets is determined using FONLL pQCD predictions to subtract the feeddown fraction. The propagation of systematic uncertainties is performed taking into account the correlations between the different sources of uncertainty. In this thesis the prompt fraction of the data using topological cut selection ranges between 0.82 and 0.91 with a maximum relative systematic uncertainty at 36%. This means a gain of 20% of precision in comparison to the published prompt fraction in [1]. The prompt fraction of the data without topological selection cuts ranges between 0.87 and 0.96 with a maximum relative systematic uncertainty at 17%. The systematic uncertainties are increased compared to [2] but the precision of the prompt fraction of the non-topological analysis is a factor of two higher than that of the topological analysis.

Kurzdarstellung

Der prompte Anteil von D^0-Mesonen wurde bestimmt für Daten, die mit dem ALICE Detektor in Proton-Proton-Kollisionen bei $\sqrt{s} = 7$ TeV aufgenommen wurden. In den gemessenen Rohdaten befinden sich D^0-Mesonen, die sowohl aus der direkten charm Produktion als auch aus dem Zerfall von B-Hadronen stammen. Mithilfe von FONLL pQCD Vorhersagen wird der Feeddown-Anteil von den gemessen Daten abgezogen und der prompte Anteil an D^0-Mesonen für zwei verschiedene Datensätze bestimmt. Die systematischen Unsicherheiten werden unter Berücksichtigung von Korrelation zwischen den einzelnen Fehlerquellen propagiert. In dieser Arbeit liegt der prompte Anteil der Daten aus topologischer Selektion zwischen 0.82 und 0.91. Die größte relative systematische Unsicherheit beträgt 36%. Im Vergleich zu den in [1] veröffentlichten Daten erhöht das die Genauigkeit um 20%. Der prompte Anteil der nicht-topologisch selektierten Daten liegt zwischen 0.87 und 0.96. Der größte relative systematische Fehler beträgt 17%. Die systematischen Unsicherheiten sind im Vergleich zu [2] größer. Die relativen Fehler des prompten Anteils der nicht-topologischen Analyse sind jedoch nur etwa halb so groß wie die relativen Fehler des prompten Anteils der topologischen Analyse.

Contents

1 Introduction

Particle physics concentrates on the fundamental building blocks of matter and their interactions by exchanging "force particles" called gauge bosons. The Standard Model of particle physics describes the fundamental particles and the forces between them by the electroweak and strong interactions with their corresponding gauge bosons, providing a successful bridge between theory and experiment. The strong interaction is characterized by the theory of quantum chromodynamics (QCD). It is not only responsible for binding neutrons and protons together in the atomic nucleus but also for the confinement of quarks into hadrons. The strong force is mediated by the gauge bosons called gluons. Amongst the fundamental matter particles, only quarks are subject to the strong force.

The different quarks with their electric charge and their masses are listed in Tab. 1.1. The masses are rounded values from the recently published Review of Particle Physics [3] and shall only give a rough overview of the mass range. Every quark carries one of the three possible color charges (red, green or blue) and all quarks have antiparticles called antiquarks holding the opposite charges. So the six different quarks in the table below are only representatives for overall 36 quarks and antiquarks in 3 different colors.

quark type	charge (e)	mass (GeV/c^2)
d	$-1/3$	0.005
u	$+2/3$	0.002
s	$-1/3$	0.1
c	$+2/3$	1.3
b	$-1/3$	4.2
t	$+2/3$	173

Table 1.1: Overview of the quarks, their electric charges and their masses [3].

The up, down and strange quarks are classified as light quarks, the charm, bottom and top quark as heavy quarks. The QCD scale parameter $\Lambda_{\mathrm{QCD}} \approx 0.2$ GeV/c^2 determines the mass division in light and heavy, as $m_{\mathrm{c}}, m_{\mathrm{b}}, m_{\mathrm{t}} \gg \Lambda_{\mathrm{QCD}}$. Since for this analysis only charm and bottom quarks are relevant the notation "heavy quark" refers as from now on only to charm and bottom quarks. Hadrons containing one heavy quark are also denoted as open heavy-flavored or as open-charm respectively open-bottom.

Although quarks can be proven experimentally, they have not yet been observed as free particles [3]. This experimental fact is explained by the hypothesis of color confinement. Due to this, quarks can only be observed in bound states (hadrons) with zero color charge. The energy that is stored in the strong field grows linearly with the distance of the quarks as soon as they leave the confined state in the hadron. The large attractive force between two deconfined quarks at the order of $\mathcal{O}(10^5)$N [4] is independent of the distance. This keeps a quark from being isolated.

Another effect in QCD is the asymptotic freedom: The strong coupling constant α_s is large at low energy scales. It is of the order $\mathcal{O}(1)$. At high energy scales of the interactions the coupling constant α_s becomes small and at some point the quarks reach a quasi-free state. This property provides the applicability for perturbative QCD (pQCD) calculations for high energy scales. The following equation shows the dependency of the strong coupling constant on the energy scale Q^2:

$$\alpha_s(Q^2) = \frac{12\pi}{(33 - 2N_f)\log(Q^2/\Lambda_{\mathrm{QCD}}^2)}. \tag{1}$$

N_f is the number of active quark flavours and Λ_{QCD}^2 is the QCD scale parameter. For energy scales above the QCD scale parameter $\Lambda_{\mathrm{QCD}}^2 \approx 200$ MeV$/c^2$ [3], pQCD calculations can be used although higher-order corrections must be considered.

At extremely high temperatures and/or pressures, quarks occur in a deconfined and thermalized state of matter known as quark-gluon plasma (QGP). This is a new state of matter where quarks can move freely. The ALICE, ATLAS and CMS experiments at the Large Hadron Collider (LHC) at CERN in Geneva are dedicated to explore the QGP and its properties by the analysis of proton-proton (pp), proton-lead and lead-lead collisions. Recently, LHCb has also joined these efforts.

If light quarks are produced in these collisions, the momentum defines the energy scale and perturbative calculations can only be applied for sufficiently high momenta. Heavy quark production is unique because it can also be calculated perturbatively in the lowest p_T range as the high masses m_c and m_b set a high energy scale independent of the momentum. Measurements of heavy-flavor production are not only an opportunity to give proof of pQCD, but also to examine the properties of the quark-

gluon plasma. Even though the conditions for the QGP to be formed are only given in ultra-relativistic heavy-ion collisions the measurements of heavy-flavored hadrons containing a charm or bottom quark in proton-proton (pp) collisions supply a good foundation for the analysis of heavy-flavor particles in heavy-ion collisions [5].

Data recorded with ALICE at $\sqrt{s} = 7$ TeV were analyzed in [1] to determine the p_T-differential inclusive production cross sections of the prompt charmed mesons D^0, D^+, and D^{*+}. As the measured raw yields of the D mesons contain contributions from both prompt charm production and feeddown from B hadrons, the feeddown contributions are subtracted using pQCD predictions. These predictions carry systematic uncertainties from different sources that must be propagated with respect to possible correlations. The prompt fraction of the D^0 mesons was calculated in [1] without consideration of all possible correlations of the systematic uncertainties. Therefore, this thesis determines the prompt fraction of the D^0 mesons that are produced at central rapidity at $\sqrt{s} = 7$ TeV and focuses on the influence and propagation of the different uncertainties considering correlations of the uncertainty sources. The data were selected in [1] applying topological selection cuts. In [2] the same data sample as in [1] was analyzed without topological selection. Therefore, in this thesis the prompt fraction for both data sets given in the topological analysis in [1] and in the non-topological analysis in [2] is calculated with the associated uncertainties and the results are discussed.

The organization of this thesis is as follows. A short overview of ALICE is given in Sect. 2. The properties of heavy quarks and the open heavy-flavored hadrons are introduced in Sect. 3, and the most important production processes of heavy quarks at the LHC are presented in Sect. 4. A detailed explanation of the FONLL framework can be found in Sect. 5. The data and theoretical predictions used in this thesis are explained in Sect. 6, and the influence of the pseudorandom number generators is evaluated in Sect. 7. The decay routine is outlined in Sect. 8 and the prompt fraction with the associated uncertainties is determined in Sect. 9. The results are presented in Sect. 10. The comparison to previous results of the prompt fraction and the comparison between the results of the topological and non-topological analysis are drawn in Sect. 11. Finally, Sect. 12 gives a summary and outlook.

2 ALICE at the LHC

A Large Ion Collider Experiment (ALICE) at the LHC analyzes the properties of the QGP which is generated within lead-lead collisions. Measurements from proton-proton and proton-lead collisions are compared to distinguish between cold-matter properties and QCD-matter signals [6].
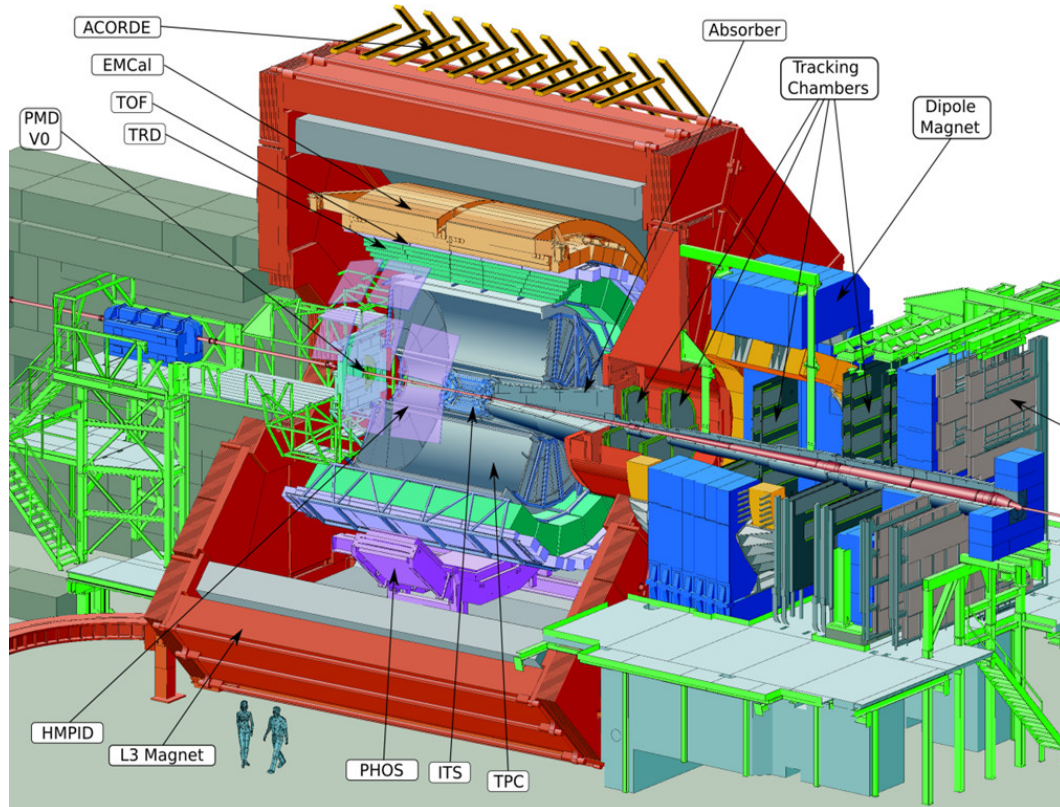
Figure 2.1: Schematic view of ALICE [6].

As mentioned in Sect. 1, charm and bottom production is of great importance for studying the properties of the QGP. Investigations of the D mesons and their decay products are the basis for the reconstruction of charm production. The decay products measured at ALICE for this purpose are hadrons such as kaons and pions. The detection of those particles mostly takes place in the Inner Tracking System (ITS), the Time Projection Chamber (TPC) and the Time Of Flight (TOF). The ITS tracks charged particles with an excellent resolution of secondary vertices even for the short decay length (123μm $\leq c\tau \leq 312\mu$m) of D mesons [7]. The TPC

provides tracking and momentum measurements of charged particles and identifies particles by their specific energy deposit $\mathrm{d}E/\mathrm{d}x$. The TOF identifies charged particles by measuring their flight times at the low-to-intermediate momentum range (< 2.5 GeV/c for kaons and pions) [8]. Supplementary to this, the Transition Radiation Detector (TRD) serves to improve the tracking reconstruction [7] and identifies electrons.

Figure 2.2: ALICE detector during the shut-down. Photo was taken at a visit in October 2014.
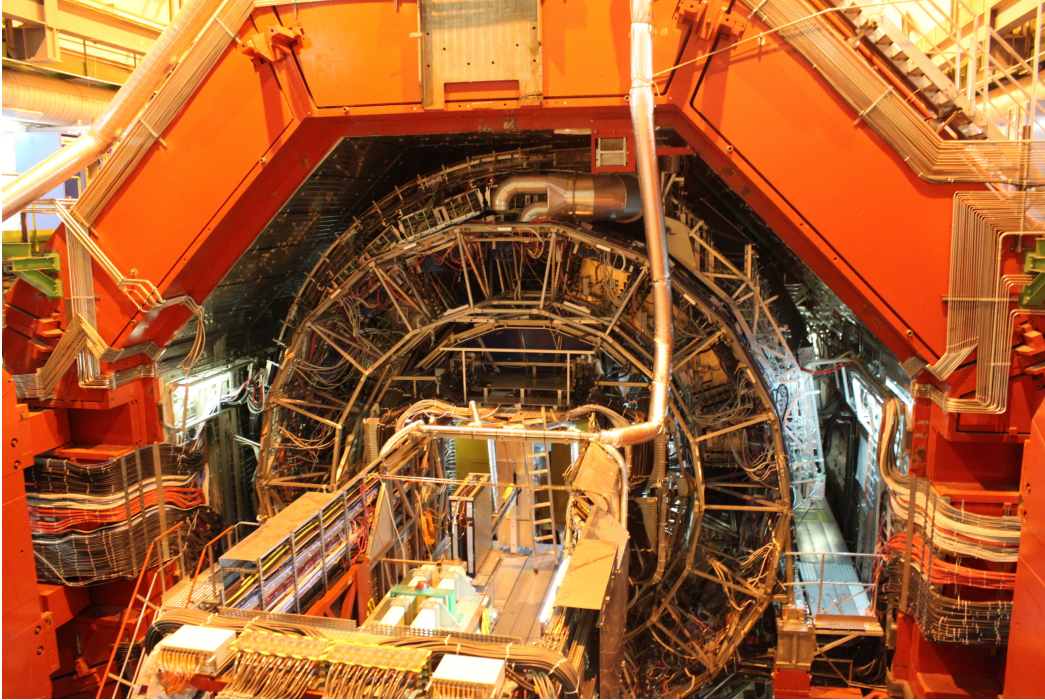
3 Properties of open-charm and open-bottom hadrons

Quarks can only be measured in hadronized states. Hadrons are classified into two groups: mesons and baryons. Mesons contain a quark and an antiquark, baryons consist of three quarks, and antibaryons consist of three antiquarks. The quarks are always combined in such a way, that the hadrons are color-neutral and carry an integral electric charge. Another distinction of the hadrons is made by their origin. If they arise directly from the confinement of charm or bottom quarks, that were produced in the collision, they are called "prompt" hadrons. If they stem from the decay of other hadrons they are denoted as "feeddown" hadrons. Conclusions can be made about important properties of charm and bottom quarks from open heavy-flavored hadrons. Hence it is important to take a closer look at open-charm and open-bottom hadrons.

Soon after their formation, quarks are confined into hadrons. This process is also called fragmentation or hadronization. The fragmentation fraction $f(q \to H_q)$ describes the probability for a particular quark q to hadronize into a certain hadron H_q. All bottom fragmentation fractions sum up to unity just as it is expected for all charm fragmentation fractions. Furthermore, it is observed that the fragmentation fractions are independent of the production process.

The heavy quarks are always produced as charm-anticharm and bottom-antibottom pairs in pp collisions. They hadronize not only into open heavy-flavored mesons and baryons but they also form quarkonia. As this contributes only about 1% to the overall relative abundances it will be neglected in the following.

3.1 Bottom fragmentation fractions

The bottom quark is confined with lighter quarks to either B-mesons (B^0, B^+, B_s^0) or b-baryons such as Λ_b^0. Their quark content is specified in Tab. 3.3. The values given in Fig. 3.1 assume

$$f(b \to B^0) + f(b \to B^+) + f(b \to B_s^0) + f(b \to \Lambda_b^0) = 100\% \qquad (2)$$

and that fragmentation fractions are the same at LEP, Tevatron and LHC [3].

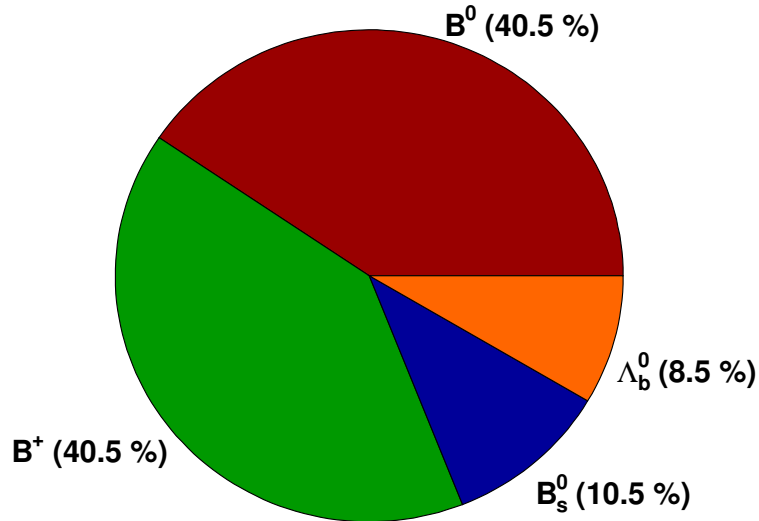Figure 3.1: Probabilities of a bottom quark to hadronize into a certain hadron $f(\mathrm{b} \rightarrow H_{\mathrm{b}})$. These values are given assuming that fragmentation fractions are the same at LEP, Tevatron and LHC in [3].

These are the current results published in the Review of Particle Physics 2014 as cited above. The analysis results of this thesis are compared to the results of the publication "Measurement of charm production at central rapidity in proton-proton collisions at $\sqrt{s} = 7\,\mathrm{TeV}$" [1] where values for the fragmentation fractions $f(\mathrm{b} \rightarrow H_{\mathrm{b}})$ from 2009 are used. These are listed in Tab. 3.1 in comparison to the recent release. As there are no significant deviations the choice of dataset should carry no weight. Consequently the up-to-date fragmentation fractions are chosen whose relative errors are in the range from 1.5% to 12.9% (1.5% (B^0, B^+), 4.8% (B_s^0), 12.9% (Λ_b^0)).

Hadron type	$f(\mathrm{b} \rightarrow H_{\mathrm{b}})(\%)$ current values	$f(\mathrm{b} \rightarrow H_{\mathrm{b}})$ (%) values from 2009
B^0	40.5 ± 0.6	40.0 ± 1.2
B^+	40.5 ± 0.6	40.0 ± 1.2
B_s^0	10.5 ± 0.5	11.4 ± 1.2
Λ_b^0	8.5 ± 1.1	8.6 ± 2.1

Table 3.1: Fragmentation fractions for bottom quark, current [3] values and values published in 2009 [9] with uncertainties.
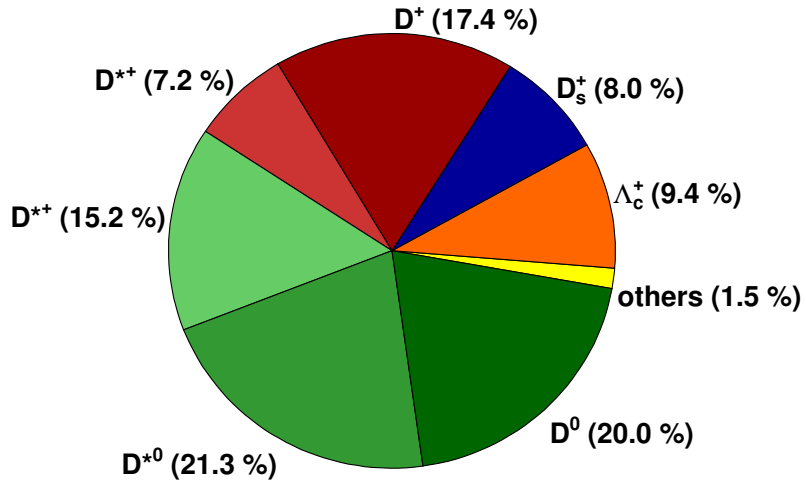
3.2 Charm fragmentation fractions

The charm quarks also unite with lighter quarks to form the Λ_c^+-baryon and the D^0, D^+ and the D_s^+ mesons. The D^{*+} and D^{*0} denote the excited states $D^*(2010)^+$ and $D^*(2007)^0$ with a very short lifetime (see Tab. 3.3). Some of the charm quarks fragment to these so-called resonances before they decay further to the D^0 and D^+ mesons. Due to the very short lifetimes of the resonances, their decay products are still included in the prompt fraction of D mesons.

The measurements concerning the charm fragmentation fractions are spread over a wider range than those of the bottom quark. Unfortunately in the publication [1] it is not mentioned which fragmentation fractions $f(c \rightarrow H_c)$ are used. An often used reference from 2007 [10] is displayed in Fig. 3.2a. These fragmentation fractions are combined results of measurements near the $\Upsilon(4S)$ resonance in e^+e^- annihilation. They are for example applied in the recently published paper "Measurements of prompt charm production cross-sections in pp collisions at $\sqrt{s} = 13$ TeV" from LHCb [11]. So this data set is used in this thesis as well.

Recently the release "Combined analysis of charm-quark fragmentation-fraction measurements" [12] with average values of the fragmentation fractions from different measurements was published entailing smaller uncertainties than the results from 2007. Both datasets are shown in Fig. 3.2 and Tab. 3.2 to give an overview of possibly occuring deviations.

The green pie slices all add up to the fragmentation fraction assigned to the D^0 meson. The red pie slices are counted among the fragmentation fraction of the D^+ meson. The $D^*(2007)^0$ resonance fully decays into D^0 mesons, whereas the $D^*(2010)^+$ resonance contributes to both the D^0 and the D^+ fraction. The branching ratios and lifetimes of the resonances, the D mesons and the Λ_c^+ baryon are listed in Tab. 3.3. The slice "others" contains mainly poorly examined Ξ_c and Ω_c states [12].

(a) Charm-quark fragmentation fraction from e^+e^- annihilation measurements near the $\Upsilon(4S)$ [10].
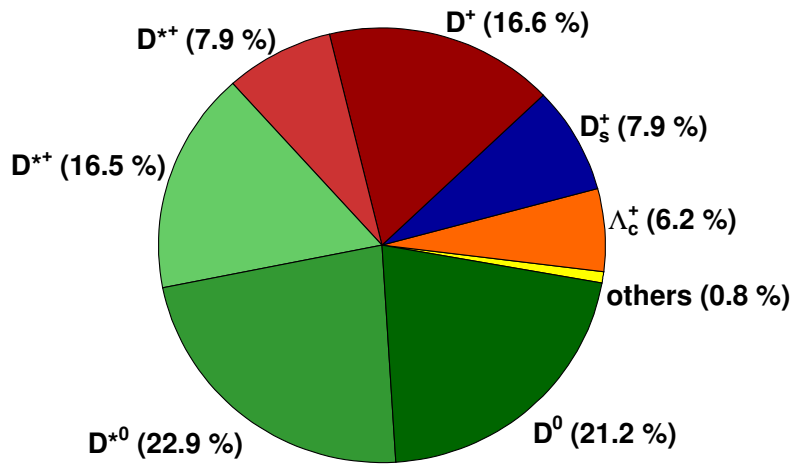
(b) Recently published combined analysis of charm-quark fragmentation fraction measurements in e^+e^-, $e^\pm p$, and pp collisions [12].

Figure 3.2: Probability for a charm quark to hadronize into a certain charmed hadron.

Hadron type	$f(\mathrm{c} \to H_\mathrm{c})(\%)$	$f(\mathrm{c} \to H_\mathrm{c})\ (\%)$
	$\mathrm{e}^+\mathrm{e}^-$ values (2007)	average values (2015)
D^0	56.5 ± 3.2	60.58 ± 0.76
D^+	24.6 ± 2.0	24.49 ± 0.65
D_s^+	8.0 ± 1.7	7.94 ± 0.47
Λ_c^+	9.4 ± 3.5	6.15 ± 0.46
D^{*0}	21.3 ± 2.4	22.86 ± 3.13
D^{*+}	22.4 ± 2.8	24.36 ± 0.50

Table 3.2: Fragmentation fractions for charm quarks. Data from $\mathrm{e}^+\mathrm{e}^-$ annihilation combined in 2007 [10] and current values combined from $\mathrm{e}^+\mathrm{e}^-$, $\mathrm{e}^\pm\mathrm{p}$ and pp collisions [12] with uncertainties.

3.3 Open-bottom and open-charm hadrons

Open heavy-flavor hadrons and their decay products deliver insight into charm and bottom production in collider experiments. The most important open-charm and open-bottom hadrons are listed in Tab. 3.3 with some fundamental properties such as the quark content, the masses m, the decay length $c\tau$ and the most important decay channels with their branching ratios $\mathcal{B}$.

For the resonances $\mathrm{D}^*(2010)^+$ and $\mathrm{D}^*(2007)^0$ the decay lengths are determined from the full decay width Γ given in [3] according to

$$c\tau = \frac{\hbar c}{\Gamma},\tag{3}$$

with $c = 299792458$ m/s and $\hbar = 6.582 \cdot 10^{-16}$ eVs. They give an impression of the large difference in magnitude between the decay length of the resonances and the other charmed hadrons. The branching ratios of the resonances show that they decay completely to the D^0 and the D^+ meson.

The listed decay channels of the D mesons D^0, D^+ and D_s^+, the baryon Λ_c^+ and the $\mathrm{D}^0\pi^+$ channel of the $\mathrm{D}^*(2010)^+$ resonance are representative channels for reconstruction of the individual charmed hadrons at ALICE. The ϕ in the D_s^+ decay channel decays further to $\phi \to \mathrm{K}^-\mathrm{K}^+$ and the D^0 in the $\mathrm{D}^*(2010)^+$ channel decays to $\mathrm{K}^-\pi^+$ before detection. The branching ratios with an "X" sum up over all possible decay channels containing the specifically mentioned particle(s) and arbitrary other particles (denoted with the "X") that arise. The branching ratios listed for the

10

b-flavored hadrons refer to the total $B^\pm/B^0/B_s^0/\Lambda_b^0$ admixture and not to single B meson types. They are taken from the $B^\pm/B^0/B_s^0/\Lambda_b^0$ admixture listing in [3]. More branching ratios for bottom-flavored hadrons are given in Tab. 8.2, where they are compared to the analysis results.

hadron types	quark content	mass (MeV/c^2)	$c\tau(\mu\mathrm{m})$	decay channel	$\mathcal{B}$ (%)
D^0	$c\bar{u}$	1864.8 ± 0.1	122.9 ± 0.4	$K^-\pi^+$	3.93 ± 0.04
D^+	$c\bar{d}$	1869.6 ± 0.1	311.8 ± 2.1	$K^-\pi^+\pi^+$	9.46 ± 0.24
D_s^+	$c\bar{s}$	1968.3 ± 0.1	149.9 ± 2.1	$\phi\,\pi^+$	2.27 ± 0.08
$D^*(2007)^0$	$c\bar{u}$	2007.0 ± 0.1	$< 9.4 \cdot 10^{-8}$	$D^0 X$	100.0 ± 4.1
$D^*(2010)^+$	$c\bar{d}$	2010.3 ± 0.1	$\approx 2.4 \cdot 10^{-6}$	$D^0\pi^+$	67.7 ± 0.5
				$D^+ X$	32.3 ± 0.6
Λ_c^+	udc	2286.5 ± 0.1	60.0 ± 1.8	$pK^-\pi^+$	$6.84 \begin{smallmatrix} +\,0.32 \\ -\,0.40 \end{smallmatrix}$
B^0	$d\bar{b}$	5279.6 ± 0.2	455.7 ± 1.2		
B^+	$u\bar{b}$	5279.3 ± 0.2	491.1 ± 1.2	$\overline{D^0}X$	59.0 ± 2.9
B_s^0	$s\bar{b}$	5366.8 ± 0.2	452.7 ± 1.5	$D^- X$	22.5 ± 1.7
Λ_b^0	udb	5619.5 ± 0.2	439.5 ± 3.0		

Table 3.3: Properties of open heavy-flavor hadrons. The $c\tau$ of the resonances $D^*(2010)^+$ and $D^*(2007)^0$ was calculated from the decay widths according to equation 3. The branching ratios (gray background) of the bottom-flavored hadrons refer to the $B^\pm/B^0/B_s^0/\Lambda_b^0$ admixture. Values are taken from [3].

The quark content of each hadron leads to integral electric charges. The heavy quarks hadronize with lighter antiquarks and the heavy antiquarks hadronize with lighter quarks in the mesons. Considering the small contribution of the valence quarks to the proton mass (1%) it must be mentioned that the valence quarks contribute about 70% to the D-meson masses and even up to 80% to the B-meson masses. The heavy quarks themselves receive their masses mainly by coupling to the Higgs field, hence they remain heavy under the conditions of the QGP and grant access to the properties of QGP [13].

This thesis focuses on the distinction between prompt and feeddown D mesons. The fragmentation fractions f refer to the formation of prompt hadrons but the branching ratios of the decay channels which are used for the reconstruction are valid for both prompt and feeddown D mesons. Prompt and feeddown hadrons are

merged together in the reconstructed raw yield. The feeddown D mesons stem from prompt B hadrons. These have an up to 4 times longer lifetime than the D mesons. Before decaying, B mesons travel further away from the primary vertex where the collision took place than the prompt D mesons. If the jets of the decay products of the bottom-flavored hadrons are reconstructed with sufficient resolution a secondary vertex next to the collision vertex shows up. So the b-quarks can be tagged and the discrimination between prompt and feeddown, namely stemming from the tagged bottom quarks, D mesons is possible.

In this thesis only data from the raw yield of D^0 mesons is provided. The prompt and feeddown D meson spectra are obtained by means of theoretical predictions. The prompt D meson and $B^\pm/B^0/B_s^0/\Lambda_b^0$ admixture spectra can be computed by the FONLL theoretical framework [14], which is publicly accessible. The $B^\pm/B^0/B_s^0/\Lambda_b^0$ spectrum is then sent through a decay routine to simulate the feeddown distribution of the D mesons. Finally the results are combined to determine the prompt fraction of the produced D^0 mesons.

4 Heavy quark production at the LHC

4.1 Leading order processes

If two hadrons collide, their partons, the constituents of the hadrons, interact with each other. In this strong interaction heavy quarks can be generated. Heavy quark production yields always a heavy quark-antiquark pair. Some of the leading-order Feynman diagrams are displayed in Fig. 4.1. 'Leading-order' means the smallest possible number of interaction vertices. The interaction strength is determined by the strong coupling constant $g_s \propto \sqrt{\alpha_s}$. The interaction probability is $\propto g_s^2 \propto \alpha_s$ for each vertex. So the total interaction probability for the interactions displayed in Fig. 4.1 is $\propto g_s^4 \propto \alpha_s^2$.
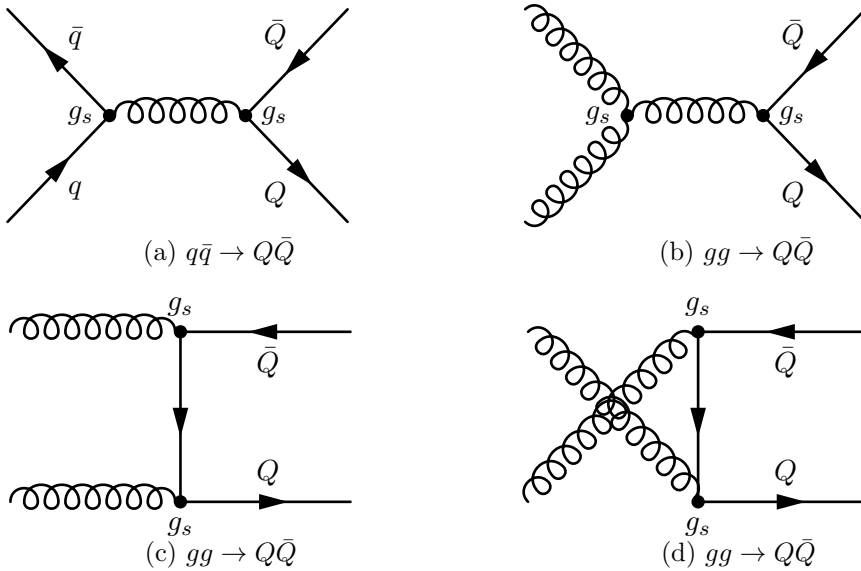

Figure 4.1: Leading order (LO) Feynman diagrams showing heavy-quark pair production. The curly lines represent gluons, the heavy (anti)quarks are denoted as $Q\,(\bar{Q})$ and the light quarks (antiquarks) are denoted as $q\,(\bar{q})$.

The quarks (antiquarks) in Fig. 4.1 are labeled with a $q\,(\bar{q})$, heavy quarks are specified by $Q\,(\bar{Q})$. The gluons are represented by curly lines. With increasing energies the contribution of the quark-antiquark annihilation (see Fig. 4.1a) diminishes and gluon-gluon fusion dominates the heavy quark pair production. At LHC energies the contribution from quark-antiquark annihilation can be neglected. Consequently, gluon-gluon pair production dominates heavy-quark pair production [2, 7].

4.2 Next-to-leading order processes

Next-to-leading order (NLO) interactions must also be considered as they contribute heavily to the amount of produced heavy quarks. The most important NLO processes are gluon-splitting in Fig. 4.2a and flavor excitation in Fig. 4.2b. The labelling is the same as in Fig. 4.1. The interaction probability for the interaction is now $\propto g_s^6 \propto \alpha_s^3$.

(a) gluon splitting   (b) flavor excitation
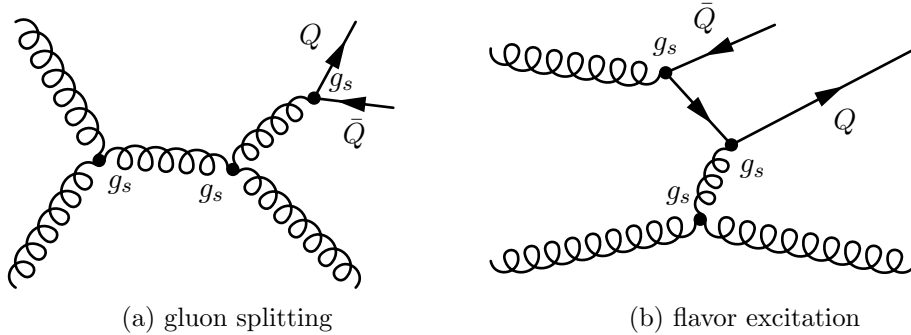
Figure 4.2: Next-to-leading order (NLO) Feynman graphs depicting the gluon splitting and the flavor excitation. The curly lines represent gluons, the heavy (anti)quarks are denoted as Q ($\bar{Q}$) [7, 15].

In the gluon splitting process depicted in Fig. 4.2a, two gluons from the scattering hadrons interact with each other and one of the outgoing gluons splits to a heavy quark-antiquark pair. During flavor excitation (shown in Fig. 4.2b), a gluon splits into a heavy quark-antiquark pair before the hard-scattering process with a gluon from the other hadron takes places. The other gluon then interacts with the heavy quark-antiquark pair. Both processes are associated with an outgoing gluon. The quarks and antiquarks are subject to confinement, and hadronize soon after their production.

In theoretical predictions, LO and NLO processes are combined to describe the production of heavy quarks appropriately. This can be done in perturbative calculations as the heavy quark masses exceed the QCD scale Λ_{QCD} significantly. Beyond that, the hadronization can be expressed in non-perturbative calculations. The FONLL framework provides a good description of the heavy quark production cross section over a large range of transverse momentum. The FONLL formalism is explained in the following section.

5 The FONLL framework

Although a heavy quark-antiquark pair is produced in hadron-hadron collisions, this thesis will now focus only on one of these heavy quarks to explain the theoretical predictions.

5.1 The NLO calculations

The production of a heavy quark Q in a hadron-hadron collision is described by

$$H_1(P_1) + H_2(P_2) \rightarrow Q(P_3) + X.$$

To calculate the cross sections of heavy quark production in the p_T range where p_T is of the order of the heavy quark mass m, perturbative calculations up to NLO $\mathcal{O}(\alpha_s^3)$ provide an appropriate approach. In fixed-order NLO calculations as provided in [16, 17], the differential cross section is given in the factorization approach by

$$\mathrm{d}\sigma^{\mathrm{FO}} = \sum_{i,j} \int \mathrm{d}x_1 \mathrm{d}x_2\, F_{H_1}^i(x_1, \mu_F)\, F_{H_2}^j(x_2, \mu_F)\, \mathrm{d}\hat{\sigma}_{ij}^{QX}(x_1 P_1, x_2 P_2, \mu_R, \mu_F) \tag{4}$$

where FO stands for the fixed-order NLO calculations [18]. Equation (4) was adapted from [15, 17, 18], and the production process is displayed schematically in 5.1 which was inspired from [15, 17].

The interacting partons i and j carry the fractions x_1 and x_2 of the four-momenta P_1 and P_2 of the colliding hadrons H_1 and H_2. The parton distribution functions (PDFs), $F_{H_1}^i(x_1, \mu_F)$ and $F_{H_2}^j(x_2, \mu_F)$, also known as structure functions, represent the probability density to find the parton i (j) in the hadron H_1 (H_2) carrying the fraction x_1 (x_2) of the four-momentum P_1 (P_2) of the hadron. The kernel cross sections $\mathrm{d}\hat{\sigma}_{ij}^{QX}(x_1 P_1, x_2 P_2, \mu_R, \mu_F)$ are massive NLO calculations that describe the probability that the heavy quark Q is produced in the interaction of the partons i and j. So in the factorization approach there is a distinction between the hard scattering processes represented in the kernel cross sections $\mathrm{d}\hat{\sigma}_{ij}^{QX}(x_1 P_1, x_2 P_2, \mu_R, \mu_F)$ and the soft processes concerning the hadrons represented by the PDFs. By these means, the hard processes can be calculated perturbatively as the soft interactions cannot be described by pQCD and must be provided by parametrization of experimental results.
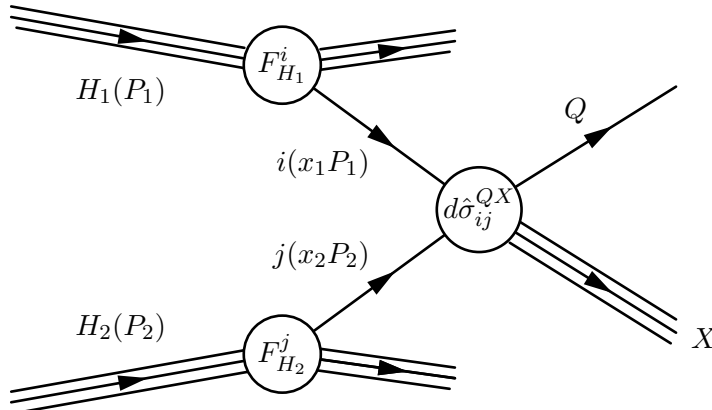
Figure 5.1: Schematic view of factorized heavy-quark production in hadron-hadron collisions. Each of the colliding hadrons H_1 and H_2 carries the four-momentum P_1 and P_2, respectively. The structure function $F^i_{H_1}$ ($F^j_{H_2}$) describes the probability density to find the parton i (j) holding the fraction x_1 (x_2) of the hadron's H_1 (H_2) four-momentum P_1 (P_2) within this hadron. The kernel cross section $d\hat{\sigma}^{QX}_{ij}$ indicates the probability for the interacting partons i and j to produce a heavy quark Q [15, 17].

The renormalization (μ_R) and factorization (μ_F) scales are introduced to handle the problem of occuring divergences caused by different effects at very high (ultraviolet) and very low (infrared) energy scales, respectively. As these parameters have no physical interpretation, the observables, e.g. the cross section, would be independent of μ_R and μ_F if the calculations were complete. However, they are limited to a finite order, so the results carry an uncertainty related to this scale dependence, which is estimated by a variation of the scales μ_R and μ_F around a central value.

If the transverse momentum p_T becomes much larger than the heavy quark mass m the NLO calculations diverge. This disturbance is caused by large logarithms of the ratio p_T/m. As a result, the predictions of the heavy quark distributions for $p_T \gg m$ fail. Therefore a new approach must be considered for this transverse momentum range.

5.2 Fragmentation function approach

The logarithmic terms can be classified as leading-logarithmic terms (LL) of the form $\alpha_s^2 (\alpha_s \log(p_T/m))^k$ and next-to-leading-logarithmic terms (NLL) of the form $\alpha_s^3 (\alpha_s \log(p_T/m))^k$. In the fragmentation function approach, these terms are resummed to all orders to obtain better predictions of the cross sections at large

16

p_T. This formalism disregards the role of the heavy quark mass in the production process as it is negligible in comparison to the high transverse momentum $p_\mathrm{T} \gg m$. Finally the massless partons fragment to massive quarks, which is described by the fragmentation function.

Again, this can be expressed in a factorized equation (taken from [19]) by

$$
\begin{aligned}
\mathrm{d}\sigma^{\mathrm{RS}} = \sum_{i,j,k} \int \mathrm{d}x_1 \mathrm{d}x_2 \mathrm{d}x_3 \Big[& F_{H_1}^i(x_1, \mu_F)\, F_{H_2}^j(x_2, \mu_F) \\
& \cdot \mathrm{d}\hat{\sigma}_{ij}^{kX}(x_1 P_1, x_2 P_2, \mu_R, \mu_F) D_k^Q(x_3 P_3, \mu_F) \Big],
\end{aligned}
\tag{5}
$$

where RS points to the resummation to all orders, and the partons i and j again carry the momentum fractions x_1 and x_2 of the momenta P_1 and P_2 of the initial hadrons with their allocated PDFs $F_{H_1}^i$ and $F_{H_2}^j$. This time the kernel cross section $\mathrm{d}\hat{\sigma}_{ij}^{kX}(x_1 P_1, x_2 P_2, \mu_R, \mu_F)$ describes the probability for the interacting partons to produce a massless parton k which can fragment to the massive heavy quark Q. This fragmentation process is specified in the fragmentation function $D_k^Q(x_3 P_3, \mu_F)$. The factorized fragmentation function formalism is depicted in Fig. 5.2.
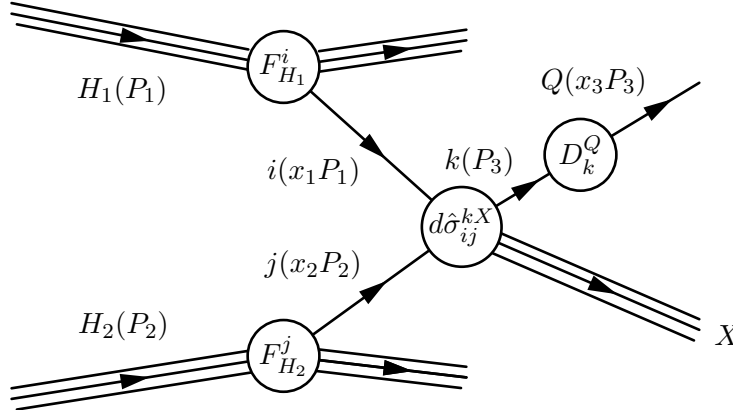

Figure 5.2: Schematic view of the factorized heavy quark production in hadron-hadron collisions in terms of the fragmentation function approach. The labels are the same as in Fig. 5.1, except for the kernel cross section $d\hat{\sigma}_{ij}^{QX}$, which now indicates the probability for the interacting partons i and j to produce a massless parton k. Its fragmentation to the heavy quark Q is described by the fragmentation function D_k^Q. The heavy quark Q carries the fraction x_3 of the virtual massless particle k with the momentum P_3. The main structure of the schematic view was taken from [15].

The NLO calculations provide a good description of the tranverse momentum range at $p_T \approx m$ and the fragmentation function approach describes the range of high transverse momenta $p_T \gg m$ very well. To obtain the cross sections of heavy quark production over a continuous range of tranverse momentum, the NLO perturbative calculations are merged with the NLL calculations from the fragmentation function formalism resummed to all orders.

5.3 FONLL

The FONLL framework [20, 21] uses the fixed order approach (FO) (Eq. (4)) for NLO calculations and combines it with the NLL resummed calculations (Eq. (5)). The acronym FONLL stands for "fixed order plus next-to-leading logarithms" [18].

The FONLL cross section for the production of heavy quarks is given by

$$d\sigma^{\text{FONLL}} = d\sigma^{\text{FO}} + G(m, p_T)(d\sigma^{\text{RS}} - d\sigma^{\text{FOM0}}) \tag{6}$$

where the definition of $d\sigma^{\text{FO}}$ is given in Eq. (4) and $d\sigma^{\text{RS}}$ is defined in Eq. (5). The cross section $d\sigma^{\text{FOM0}}$ is the massless limit of the FO approach for $m/p_T \to 0$ where some parts are kept and do not vanish in the massless limit. They prevent terms from occurring doubly from both FO and RS calculations [18, 20]. Finally $G(m, p_T)$ is given as

$$G(m, p_T) = \frac{p_T^2}{p_T^2 + a^2 m^2}, \quad \text{with} \quad a = 5 \tag{7}$$

to suppress the resummation correction $d\sigma^{\text{RS}} - d\sigma^{\text{FOM0}}$ for $m_T < 5m$, with the transversal mass $m_T = \sqrt{p_T^2 + m^2}$. The choice of the factor $a = 5$ is explained in [20].

In figure 5.3 the difference between the NLO calculations (red line) and the FONLL approach (blue line) can be seen using the example of the charm quark distribution.

The FONLL framework is freely accessible [14] and provides the possibility of calculating the cross sections of heavy quark production (charm or bottom) in pp or p$\bar{\text{p}}$ collisions. As only hadrons and their respective decay products are measured in experiments, the FONLL framework makes the cross sections of these heavy-flavored hadrons and their decay products available, too.
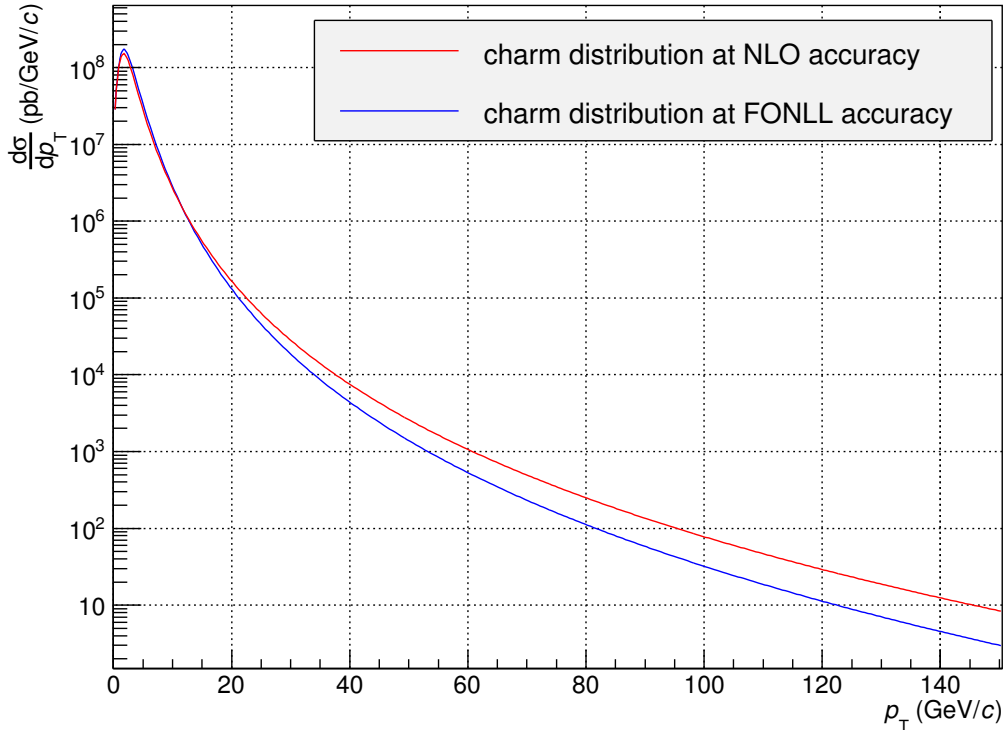
Figure 5.3: The charm quark cross section calculcated with NLO accuracy (red) and with the FONLL approach (blue). A large deviation can be seen, especially for $p_\mathrm{T} > 20$ GeV/c.

5.4   Non-perturbative fragmentation functions for bottom and charm quarks

The last step in the FONLL calculations that must be taken for this thesis is the description of the fragmentation of the heavy quarks into heavy-flavored hadrons. For this purpose the perturbative calculations mentioned above are numerically convolved with non-perturbative fragmentation functions $D^{\mathrm{NP}}_{q \to H_q}$. Their integrals are the fragmentation fractions $f(q \to H_q)$. The production cross section of the heavy-flavored hadrons is given by

$$\mathrm{d}\sigma^{\mathrm{FONLL}}_{H_Q} = \mathrm{d}\sigma^{\mathrm{FONLL}} \otimes D^{\mathrm{NP}}_{q \to H_q}. \tag{8}$$

The FONLL framework uses a Kartvelishvili et al. distribution [22] to parametrize

19

the fragmentation of bottom quarks to B hadrons:

$$D_{b \to H_b}^{NP} = (\alpha + 1)(\alpha + 2)z^{\alpha}(1 - z), \qquad (9)$$

where z is the fraction of the momentum of the initial heavy quark and α is a parameter which is chosen from the results of LEP data fittings [23] according to the bottom mass m_b. For the central mass value $m_b = 4.75$ GeV/c^2, $\alpha = 24.2$ is applied.
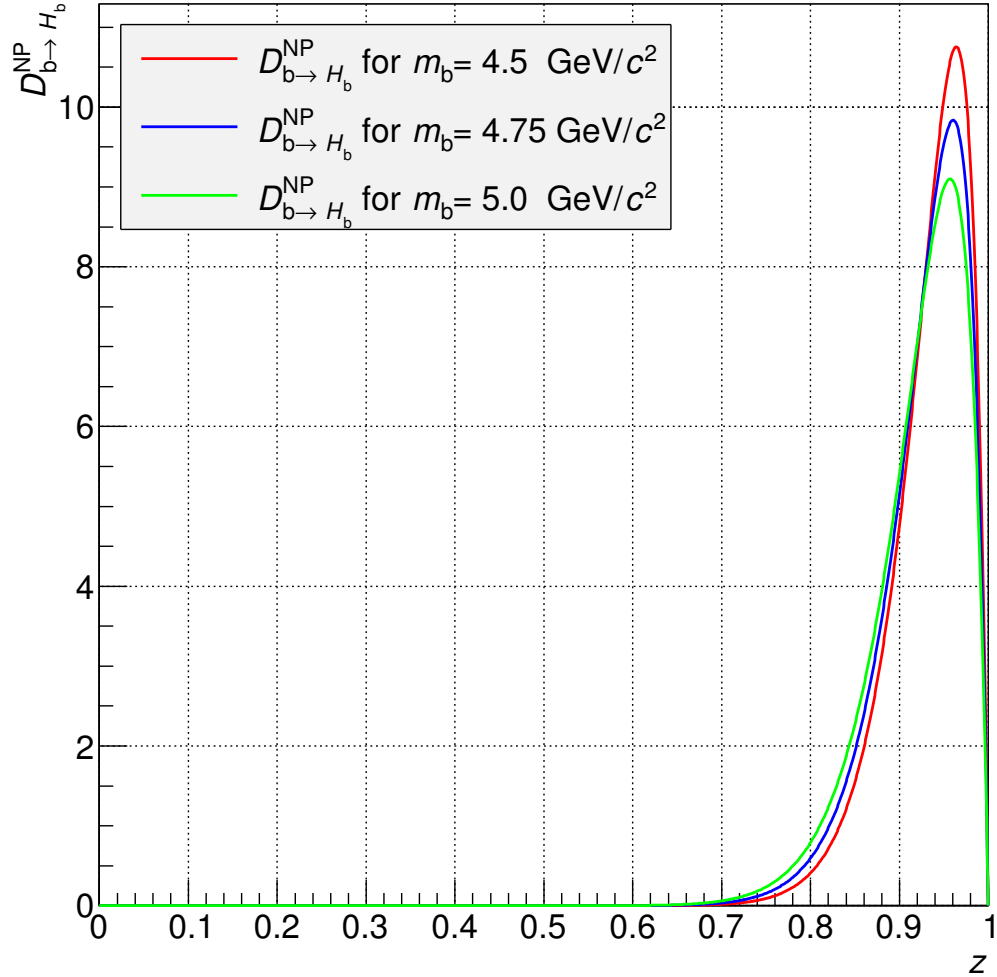

Figure 5.4: Non-perturbative fragmentation function for bottom production. The B hadrons carry the momentum fraction z of the initial b-quark.

To estimate uncertainties due to the bottom mass, $\alpha = 26.7$ (associated with

m_b = 4.5 GeV/c^2) and α = 22.2 (associated with m_b = 5.0 GeV/c^2) are included in the calculations. As $D^{NP}_{b \to H_b}$ describes the fragmentation process of the B$^\pm$/B^0/B^0_s/Λ^0_b admixture, it is normalized to unity in accordance with Eq. (2). The FONLL framework does not differentiate between the different B-hadron types.

The hadronization of charm quarks is more difficult to parametrize. As displayed in Fig. 3.2, a large fraction of the prompt D^0 and D$^+$ mesons originates from the resonances D^{*+} and D^{*0}. These resonances are vector mesons; the D^0 and D$^+$ mesons are pseudoscalar mesons. The fragmentation function from a charm quark to a vector mesons has to be modeled other than to a pseudoscalar meson. So for the D^0 and D$^+$ mesons both parametrizations must be combined. For the resonances the fragmentation function can be derived more easily by only considering one fragmentation formalism and the corresponding fragmentation fraction. The applied fragmentation fractions and branching ratios are derived from experimental data [24].

The computation of the fragmentation functions $D^{NP}_{c \to H_c}$ is explicitly given in the following. The fragmentation function for a charm quark to a pseudoscalar D meson is

$$
\begin{aligned}
D_{c \to P}(z) \; = \; 5 \, \frac{rz(1-z)^2}{(1-(1-r)z)^6} \Big(& 6 - 18(1-r)z + (21 - 74r + 68r^2)z^2 \\
& - 2(1-r)(6 - 19r + 18r^2)z^3 + 3(1-r)^2(1 - 2r + 2r^2)z^4 \Big),
\end{aligned}
\tag{10}
$$

and the fragmentation function for a charm quark to a vector D meson is

$$
\begin{aligned}
D_{c \to V}(z) \; = \; 15 \, \frac{rz(1-z)^2}{(1-(1-r)z)^6} \Big(& 2 - 2(3 - 2r)z + 3(3 - 2r + 4r^2)z^2 \\
& - 2(1-r)(4 - r + 2r^2)z^3 + (1-r)^2(3 - 2r + 2r^2)z^4 \Big).
\end{aligned}
\tag{11}
$$

These equations are the equations (31) and (32) from [25], and are derived from the equations (9) and (12) from [26]. The values 5 and 15 are taken from [23, 27]. The parameter r depends on the charm quark mass. It is $r = 0.1$ for $m_c = 1.5$ GeV/c^2, $r = 0.06$ for $m_c = 1.3$ GeV/c^2, and $r = 0.135$ for $m_c = 1.7$ GeV/c^2. The values are all extracted from experimental data [15, 24, 25].

In the following only the central mass value $m_c = 1.5$ GeV/c^2 corresponding to

$r = 0.1$ is considered. $D_{c \to P}(z)$ and $D_{c \to V}(z)$ are normalized to unity, so from now on the normalization is taken for granted. Then the fragmentation functions for the individual D mesons must be deduced. The fragmentation fractions

$$f(c \to D^0_{\text{prompt}}) = 0.168, \tag{12a}$$

$$f(c \to D^+_{\text{prompt}}) = 0.162, \tag{12b}$$

$$f(c \to D^*) = 0.233, \tag{12c}$$

and branching ratios

$$\mathcal{B}(D^{*0} \to D^0) = 1.0, \tag{13a}$$

$$\mathcal{B}(D^{*+} \to D^0) = 0.677, \tag{13b}$$

$$\mathcal{B}(D^{*+} \to D^+) = 0.323, \tag{13c}$$

are used in [28] from [24, 29].

The fragmentation fractions $f(c \to D^{*0}_{\text{prompt}})$ and $f(c \to D^{*+}_{\text{prompt}})$ are assumed to be equal, which is consistent within uncertainties with the values given in Tab. 3.2. The other fragmentation fractions are consistent with the data from 2007 in Tab. 3.2. The branching ratios are all consistent with actual data given in Tab. 3.3.

To determine the fragmentation functions $D^{\text{NP}}_{c \to D^0}$ and $D^{\text{NP}}_{c \to D^+}$ the normalized functions $D_{c \to P}(z)$ and $D_{c \to V}(z)$ are combined in regard of the corresponding fragmentations fractions and branching ratios. Beyond that, the range of validity must be considered for the combination of the different fragmentation functions. The fragmentation functions $D^{\text{NP}}_{c \to H_c}$ for all D mesons are given in [28] by

$$D^{\text{NP}}_{c \to D^0} = 0.168\, D_{c \to P}(z) + \ 0.39 \ \ \Theta\left(\frac{m_{D^0}}{m_{D^*}} - z\right) D_{c \to V}\left(\frac{m_{D^*}}{m_{D^0}}z\right) \frac{m_{D^*}}{m_{D^0}}, \tag{14}$$

$$D^{\text{NP}}_{c \to D^+} = 0.162\, D_{c \to P}(z) + 0.07526\, \Theta\left(\frac{m_{D^+}}{m_{D^*}} - z\right) D_{c \to V}\left(\frac{m_{D^*}}{m_{D^+}}z\right) \frac{m_{D^*}}{m_{D^+}}, \tag{15}$$

$$D^{\text{NP}}_{c \to D^*} = 0.233\, D_{c \to V}(z). \tag{16}$$

To derive the fragmentation functions for the pseudoscalar mesons, the fragmentation function of vector D mesons and z are scaled with $\left(m_{D^*}/m_{D^{0/+}}\right)$. The Heaviside function Θ limits the range of validity for $D_{c \to V}\left(m_{D^*}/m_{D^{0/+}} \cdot z\right)$ from 0 to $\left(m_{D^{0/+}}/m_{D^*}\right)$. The fragmentation fraction $f(c \to D^*)$ and the branching ratios

$\mathcal{B}(\mathrm{D}^* \to \mathrm{D}^{0/+})$ are combined to give

$$f(\mathrm{c} \to \mathrm{D}^*) \cdot \mathcal{B}(\mathrm{D}^{*0} \to \mathrm{D}^0) + f(\mathrm{c} \to \mathrm{D}^*) \cdot \mathcal{B}(\mathrm{D}^{*+} \to \mathrm{D}^0) = 0.39, \tag{17a}$$

$$f(\mathrm{c} \to \mathrm{D}^*) \cdot \mathcal{B}(\mathrm{D}^{*+} \to \mathrm{D}^+) = 0.07526, \tag{17b}$$

and the numerical values are yet inserted in Eq. (14), (15) and (16). The pseudoscalar meson fragmentation function is then combined with the vector meson fragmentation function.

According to [28] the experimentally determined uncertainties of the branching ratios and fragmentation fractions are neglected as they are insignificant compared with other uncertainties (e.g. the uncertainties from the charm mass).

For the D mesons, the fragmentation functions shown in Fig. 5.5 were normalized to one. Beforehand the normalization the integrals were determined as follows:

$$f(\mathrm{c} \to \mathrm{D}^0) = \int_0^1 D^{\mathrm{NP}}_{\mathrm{c} \to \mathrm{D}^0}(z) \, \mathrm{d}z = 0.566, \tag{18a}$$

$$f(\mathrm{c} \to \mathrm{D}^+) = \int_0^1 D^{\mathrm{NP}}_{\mathrm{c} \to \mathrm{D}^+}(z) \, \mathrm{d}z = 0.241, \tag{18b}$$

$$f(\mathrm{c} \to \mathrm{D}^*) = \int_0^1 D^{\mathrm{NP}}_{\mathrm{c} \to \mathrm{D}^*}(z) \, \mathrm{d}z = 0.233. \tag{18c}$$

These fragmentation fractions used by the FONLL framework are slightly different from those given in Tab. 3.2. Although they are consistent within uncertainties, in this thesis the fragmentation fraction $f(\mathrm{c} \to \mathrm{D}^0) = 0.565$ is used in the FONLL settings. The fragmentation functions of D^0 (blue) and D^+ (red) show a small and a large peak, revealing that one part stems from the decay of the resonances and the other stems from the hadronization of the charm quarks directly. This is different for the fragmentation function of the D^* resonances (violet), which features only one peak caused by the fragmentation of the charm quarks.

All of the fragmentation functions show that the open heavy-flavored mesons carry a large fraction of the momentum of the initial heavy quark. The mean values of the momentum fractions of the initial heavy quarks are $\langle z \rangle_\mathrm{b} \approx 0.93$ for the bottom-flavored hadrons and $\langle z \rangle_\mathrm{c} \approx 0.77$ for the D^0 meson. So the confinement with a lighter quark does not decelerate the heavy quark substantially. This is even

more appropriate for the $B^{\pm}/B^0/B_s^0/\Lambda_b^0$ admixture, where the peak is even closer to one than the peaks of the D meson fragmentation distributions.
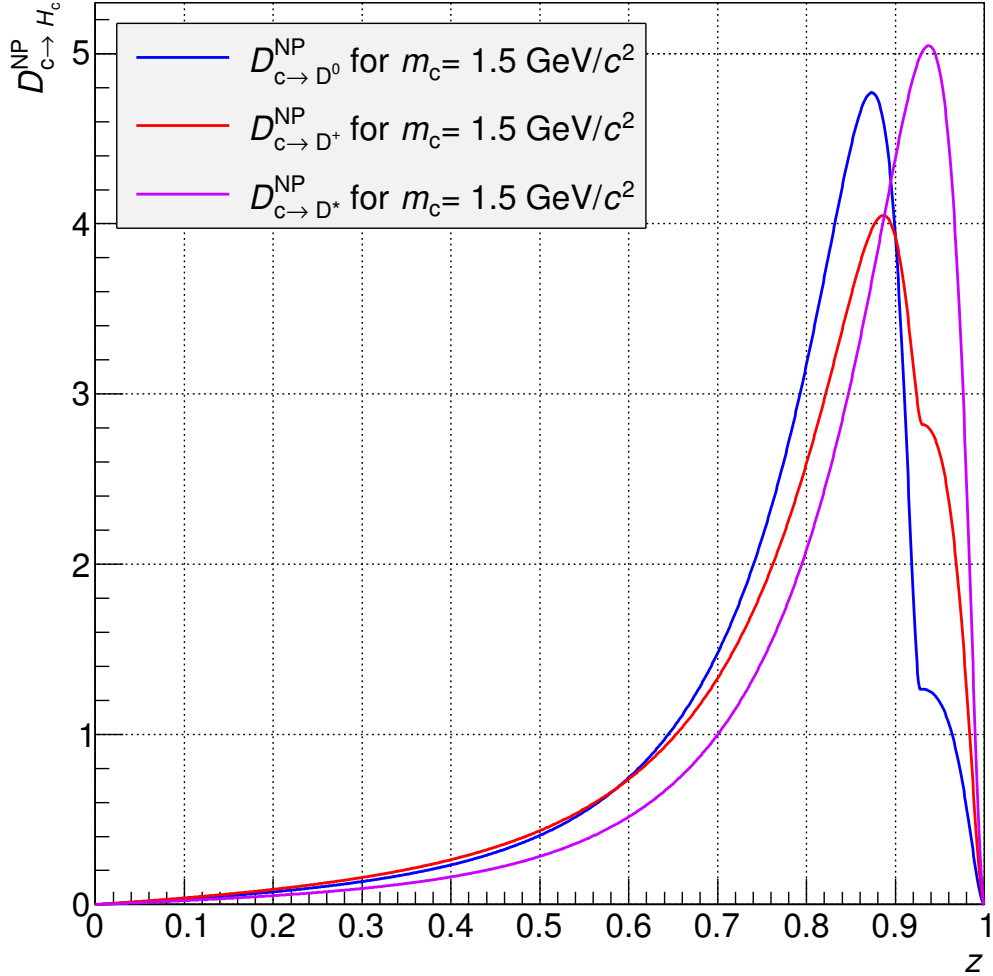

Figure 5.5: Non-perturbative fragmentation functions for charm production for the central mass value $m_c = 1.5\ \text{GeV}/c^2$. The D mesons carry the momentum fraction z of the initial charm quark.

5.5 FONLL uncertainties

The FONLL calculations are affected by a theoretical uncertainty [15, 27] caused by the renormalization and factorization scales μ_R and μ_F. Firstly a central value for these scales is determined at $\mu_R = \mu_F = \mu_0 = \sqrt{p_T^2 + m^2}$, where μ_0 is the transverse mass. To estimate the theoretical uncertainties, the relation $\xi_{R,F} \equiv \mu_{R,F}/\mu_0$ is used

to get seven evaluation sets

$$(\xi_R, \xi_F) \in \{(1,1), (0.5, 0.5), (2,2), (0.5, 1), (1, 0.5), (2, 1), (1, 2)\}, \qquad (19)$$

fulfilling the conditions $0.5 \leq \xi_{R,F} \leq 2$ and $0.5 \leq \xi_R/\xi_F \leq 2$. The differential cross sections $d\sigma$ are then evaluated for all seven combinations of the scales, while all other parameters are kept to their central values. The envelope of this evaluation is then taken and one gets a distribution of minimum differential cross sections $d\sigma_{min}^{sc}$ and of maximum differential cross sections $d\sigma_{max}^{sc}$ for the uncertainty band of the scale variation. For the propagation of errors the upper and lower error is determined as

$$\Delta d\sigma_+^{sc} = d\sigma_{max}^{sc} - d\sigma_{central}, \qquad (20a)$$

$$\Delta d\sigma_-^{sc} = d\sigma_{central} - d\sigma_{min}^{sc}. \qquad (20b)$$

For $d\sigma_{central}$, all data sets are at the central values given in this section.

There is also experimental data used in the FONLL calculations, which carries uncertainties [15, 27]. This concerns the heavy quark masses and the PDFs. The bottom mass is chosen as $m_b = (4.75 \pm 0.25)$ GeV/c^2, the charm mass as $m_c = (1.5 \pm 0.2)$ GeV/c^2. Consequently, the mass variations are accomplished for the bottom quark for the mass values $m_b = 4.5$, 4.75 and 5 GeV/c^2 and for the charm quark for the mass values $m_c = 1.3$, 1.5 and 1.7 GeV/c^2. These variations are also applied to the non-perturbative parameters described above. Keeping all other input parameters at their central values, the evaluation generates a minimum $d\sigma_{min}^{mass}$ and a maximum $d\sigma_{max}^{mass}$ differential cross section for the uncertainty band of the mass variation. The upper and lower error is:

$$\Delta d\sigma_+^{mass} = d\sigma_{max}^{mass} - d\sigma_{central}, \qquad (21a)$$

$$\Delta d\sigma_-^{mass} = d\sigma_{central} - d\sigma_{min}^{mass}. \qquad (21b)$$

The default PDF set is CTEQ6.6, which is maintained for all data in this thesis. Again the mass and scale parameters are fixed to their central values when the PDF uncertainties associated with the CTEQ6.6 set are propagated to get a minimum $d\sigma_{min}^{PDF}$ and a maximum $d\sigma_{max}^{PDF}$ differential cross section for the PDF uncertainty

band

$$\Delta d\sigma_+^{\mathrm{PDF}} = d\sigma_{\max}^{\mathrm{PDF}} - d\sigma_{\mathrm{central}}, \tag{22a}$$

$$\Delta d\sigma_-^{\mathrm{PDF}} = d\sigma_{\mathrm{central}} - d\sigma_{\min}^{\mathrm{PDF}}. \tag{22b}$$

The total uncertainty $\Delta d\sigma_\pm$ is given by

$$\Delta d\sigma_\pm = \sqrt{(\Delta d\sigma_\pm^{\mathrm{sc}})^2 + (\Delta d\sigma_\pm^{\mathrm{mass}})^2 + (\Delta d\sigma_\pm^{\mathrm{PDF}})^2}, \tag{23}$$

and the maximum $d\sigma_+$ and minimum $d\sigma_-$ differential cross sections are defined as

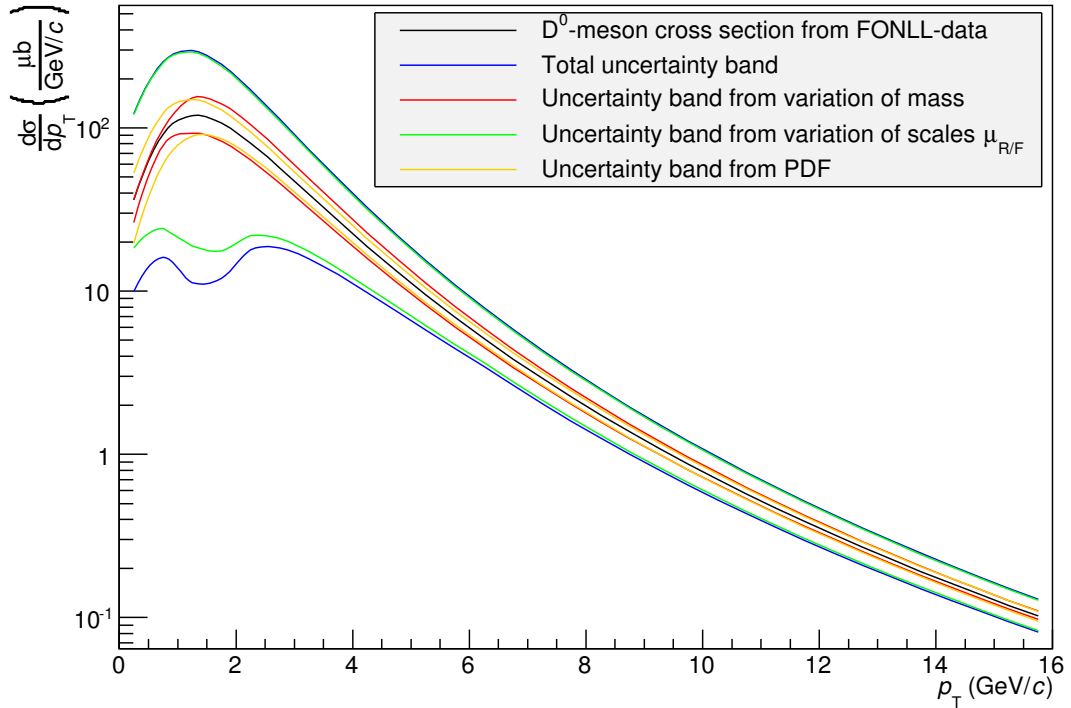$$d\sigma_\pm = d\sigma \pm \Delta d\sigma_\pm. \tag{24}$$

Figure 5.6: Prompt D^0 meson FONLL spectrum with all uncertainty bands. The variation of scales dominates the uncertainties. The p_T range is limited to 16 GeV/c as it will be in the available experimental data.

5.6 Settings of the FONLL framework

On the FONLL homepage [14] the following settings can be chosen:

1. **Collider:** Choice between RHIC (pp), HERA (p$\bar{\text{p}}$) and LHC (pp) runs at different $\sqrt{s}$. Setting in this thesis: LHC (pp) at $\sqrt{s} = 7$ TeV.

2. **Heavy quark:** Charm or bottom quark can be selected as the heavy quark.

3. **PDFs:** Different PDF sets available. The default setting (CTEQ6.6) is used in this work.

4. **Perturbative order:** Either FONLL (default) or NLO can be chosen.

5. **Final state:**

   - bare quark for both charm and bottom quark
   - B hadrons for bottom quark
   - D^0, D^+, D^* or $0.7\,D^0 + 0.3\,D^+$ admixture for charm quark

6. **Further decay:** (not set for this thesis)

   - not possible for bare quarks
   - for B hadrons: hadron to electron, B to D to electron, B to J/ψ, B to $\psi(2S)$, B to D, B to D^*
   - Hadron to electron for all D mesons.

7. **Cross section type:** Total cross section, p_{T}-, y-, η-differential cross section or double differential cross section selectable. Selection of included uncertainties and output.

8. **p$_{\text{Tmin}}$ and p$_{\text{Tmin}}$:** The p_{T} range is set here in GeV. The maximum depends on the chosen collider. If the values are filled into bins with the bin width w_{bin} the minimum should be chosen as $0.5 \cdot w_{\text{bin}}$.

9. **y($\boldsymbol{\eta}$)$_{\text{min}}$ and y($\boldsymbol{\eta}$)$_{\text{min}}$:** Selection between rapidity y and pseudorapidity η is possible by setting a marker on 'y' or 'eta'. Then the (pseudo)rapidity range can be determined.

10. **npoints:** The number of points n. It is related to the bin width w_{bin} and the p_{T} range: $n = \dfrac{1}{w_{\text{bin}}}(p_{\text{Tmax}} - p_{\text{Tmin}}) + 1$

11. **Non-perturbative settings:** Choice between different fragmentation functions and their parameters are possible. For this thesis only default settings are used.

12. **FF and BR:** Fragmentation fractions and branching ratios can be specified. This is required for the fragmentation for charm quarks to the D^0 mesons in this thesis.

6 Data sets

6.1 Experimental data

The experimental input data for this thesis are selected events from pp collisions at $\sqrt{s} = 7$ TeV. The data were recorded with ALICE in 2010. Many steps are taken between event selection and signal extraction, however, these are not explained in detail in this thesis as the input data was taken as raw yields of D^0 mesons from [1] and [2]. Both works use the same data sample as basis, but differ in the methods of event selection. The most significant difference is the application of topological cuts which is done in [1] but not in [2]. Topological cuts refer to the decay topology of the particles as criterion of discrimination from the background.

6.1.1 Raw yield with topological selection

The detailed data collection, reconstruction and selection for the determination of the raw yield $N_{\mathrm{raw}}^{\mathrm{top}}$ is explained in [1]. A distinctive characteristic of the D mesons is the decay length of $\sim 100\mu$m. Their displacement from the primary vertex (center of collision) is resolvable by the ITS for particles with $p_{\mathrm{T}} > 1$ GeV/c [2]. To distinguish the D mesons from the large combinatorial background this property serves as topological selection cut. This reduces the combinatorial background significantly. However, the D-meson selection is limited to a lower limit of $p_{\mathrm{T}} > 1$ GeV/c.

Several other particle identification (PID) criteria and kinematic cuts were applied before signal extraction. Of these, the fiducial acceptance cut $|y_{\mathrm{D}}| < y_{\mathrm{fid}}(p_{\mathrm{T}})$ will be important in this thesis. It has a smooth slope from 0.5 to 0.8 for $0 < p_{\mathrm{T}} \leq 5$ GeV/c and is constant at 0.8 for $p_T > 5$ GeV/c [1].

$$
|y_{\mathrm{D}}| = \begin{cases} \dfrac{0.2}{15} \dfrac{p_{\mathrm{T}}^2}{(\mathrm{GeV}/c)^2} + \dfrac{1.9}{15} \dfrac{p_{\mathrm{T}}}{\mathrm{GeV}/c} + 0.5 & p_{\mathrm{T}} \leq 5.0 \text{ GeV}/c; \\ 0.8 & p_{\mathrm{T}} > 5.0 \text{ GeV}/c. \end{cases} \tag{25}
$$

The fiducial acceptance is depicted in Fig. 6.1. The integrated luminosity is $\mathcal{L}_{int} = 5$ nb^{-1}, with a relative uncertainty of 3.4%.
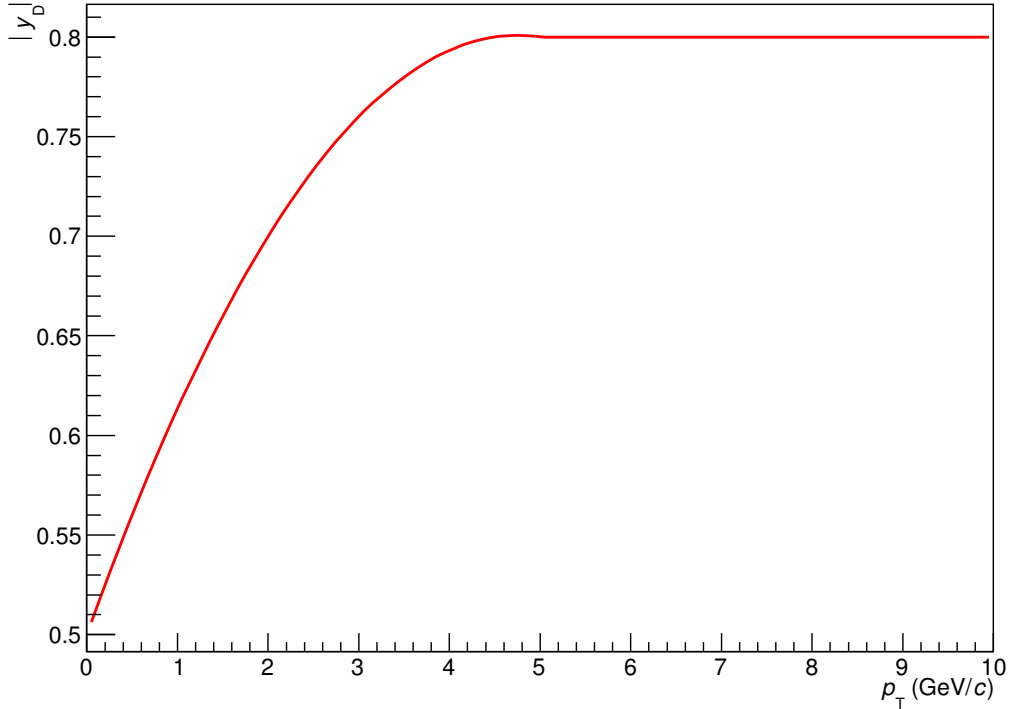
Figure 6.1: Fiducial acceptance cut $|y_D|$ as a function of p_T [30].

In the reconstruction and selection process, different acceptances and efficiencies for prompt (D^0_{pr}) and feeddown (D^0_{fd}) mesons occur. This gives rise to an efficiency correction describing the probability that a D^0 meson is detected, reconstructed and selected in the measurement and analysis. In the topological data analysis, efficiencies for vertex reconstruction, track reconstruction and selection, particle identification (PID) cuts and selection of secondary vertex topologies of the D^0-meson candidates are used [1]. The systematic uncertainties of the acceptance times efficiencies $\alpha \times \epsilon$ are derived from the relative systematic uncertainties of the track efficiency of 8% and the cut efficiency of 10%. These are only given for the lowest and the highest p_T interval in [1]. To get the systematic uncertainties also for the other p_T intervals it is assumed that these relative systematic uncertainties are valid over the whole p_T range in this thesis. They are then added quadratically, resulting in a total relative systematic uncertainty of 12.8% for $\alpha \times \epsilon$ [31]. The acceptance times efficiency values $\alpha \times \epsilon$ are depicted in Fig. 6.2 and listed together with the raw yield N^{top}_{raw} in Tab. 6.1.
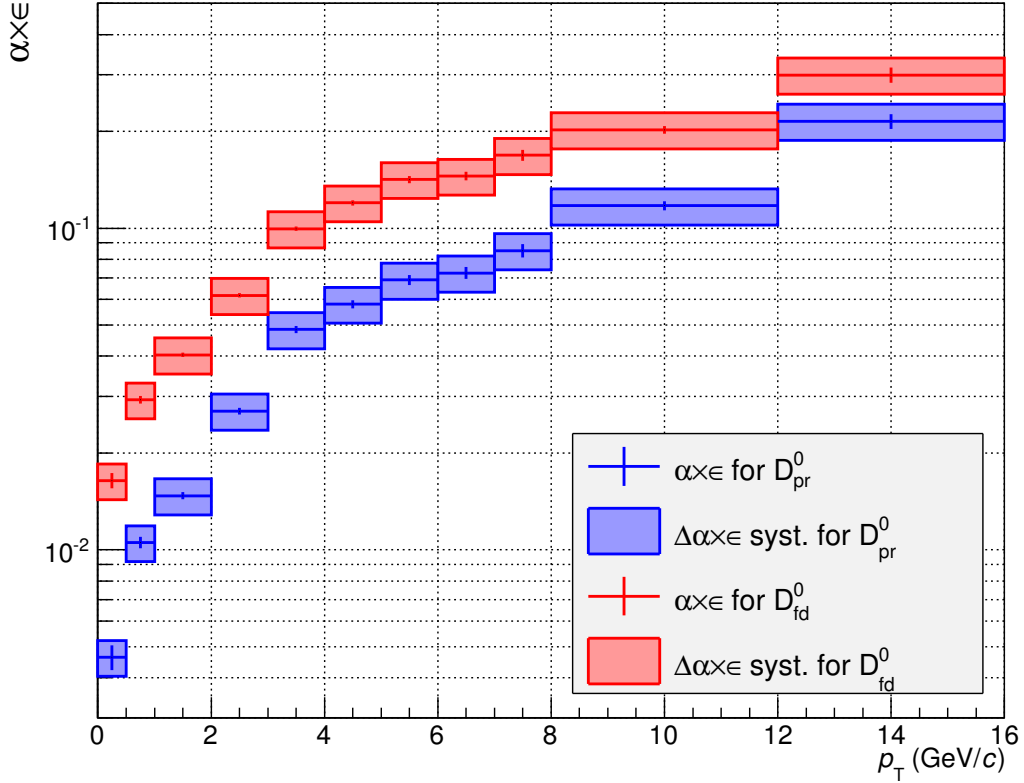
Figure 6.2: Acceptance times efficiency ($\alpha \times \epsilon$) for prompt and feeddown D^0 mesons related to the analysis applying the topological selection cut [1, 32].

As can be seen in Fig. 6.2 the acceptance times efficiency ($\alpha \times \epsilon$) for the feeddown D^0 mesons is larger than that of the prompt D^0 mesons. Due to the larger decay length of the B hadrons in comparison to the D mesons, the probability for detection and selection of the feeddown candidates is higher as their secondary vertex is displaced further from the primary vertex than the secondary vertex of the prompt fraction of D^0 mesons. The higher the transverse momentum of the different particles, the higher is the probability for the decay products to reach the detector. As a consequence, the $\alpha \times \epsilon$ increases with increasing p_T. The systematic uncertainties are shown as colored boxes and the statistical uncertainties are depicted as vertical lines in Fig. 6.2.

p_T range (GeV/c)	$N_{\text{raw}}^{\text{top}} \pm$ stat. $\pm$ syst.	$(\alpha \times \epsilon) \pm$ stat. $\pm$ syst. for D_{pr}^0	$(\alpha \times \epsilon) \pm$ stat. $\pm$ syst. for D_{fd}^0
0 − 0.5		$0.005 \pm 0.0004 \pm 0.001$	$0.016 \pm 0.001 \pm 0.002$
0.5 − 1		$0.011 \pm 0.0004 \pm 0.001$	$0.029 \pm 0.001 \pm 0.004$
1 − 2	$1531 \pm 233 \pm 340$	$0.015 \pm 0.0004 \pm 0.002$	$0.040 \pm 0.001 \pm 0.005$
2 − 3	$1978 \pm 168 \pm 190$	$0.027 \pm 0.001 \pm 0.004$	$0.062 \pm 0.001 \pm 0.008$
3 − 4	$1950 \pm 129 \pm 75$	$0.048 \pm 0.001 \pm 0.006$	$0.100 \pm 0.002 \pm 0.013$
4 − 5	$1184 \pm 78 \pm 40$	$0.058 \pm 0.002 \pm 0.007$	$0.120 \pm 0.002 \pm 0.015$
5 − 6	$623 \pm 50 \pm 25$	$0.069 \pm 0.003 \pm 0.009$	$0.142 \pm 0.004 \pm 0.018$
6 − 7	$339 \pm 32 \pm 13$	$0.073 \pm 0.003 \pm 0.009$	$0.145 \pm 0.005 \pm 0.019$
7 − 8	$199 \pm 25 \pm 14$	$0.085 \pm 0.004 \pm 0.011$	$0.169 \pm 0.006 \pm 0.022$
8 − 12	$427 \pm 38 \pm 30$	$0.117 \pm 0.004 \pm 0.015$	$0.202 \pm 0.006 \pm 0.026$
12 − 16	$139 \pm 27 \pm 14$	$0.215 \pm 0.011 \pm 0.028$	$0.300 \pm 0.017 \pm 0.038$

Table 6.1: Values for the raw yield $N_{\text{raw}}^{\text{top}}$ of D^0 mesons and acceptance times efficiency $\alpha \times \epsilon$ for prompt and feeddown D^0 mesons related to the topological selection cut with their corresponding bin width. The values were taken from [1, 32].

6.1.2 Raw yield without topological selection

When the raw yield $N_{\text{raw}}^{\text{not}}$ is determined without topological selection cuts in [2], the combinatorial background in the selected data set is considerably larger than with topological cuts. However, the analysis technique makes it possible to extract a raw yield down to $p_T = 0$ GeV/c. This is not possible in the topological analysis because of the limited resolution of secondary vertices in the low p_T region induced by too small Lorentz boosts. Nevertheless this non-topological analysis is important, considering that over 50% of the D^0 yield is predicted to be in the range of $p_T < 2$ GeV/c according to FONLL calculations [2]. This p_T region cannot be neglected for a proper determination of the charm production cross section. To reduce the combinatorial background, a like-sign technique is applied to the data set before signal extraction. Further explanations can be found in [2].

The fiducial acceptance is $y_{\text{fid}} = 0.8$ over the entire analyzed p_T range [2]. Abandoning the topological cuts leads to an acceptance times efficiency $\alpha \times \epsilon$ that is the same for prompt and feeddown D^0 mesons. They are listed in Tab. 6.2 and displayed in Fig. 6.3. The integrated luminosity is $\mathcal{L}_{\text{int}} = 5.25$ nb^{-1} with a relative uncertainty of 3.5% [2].
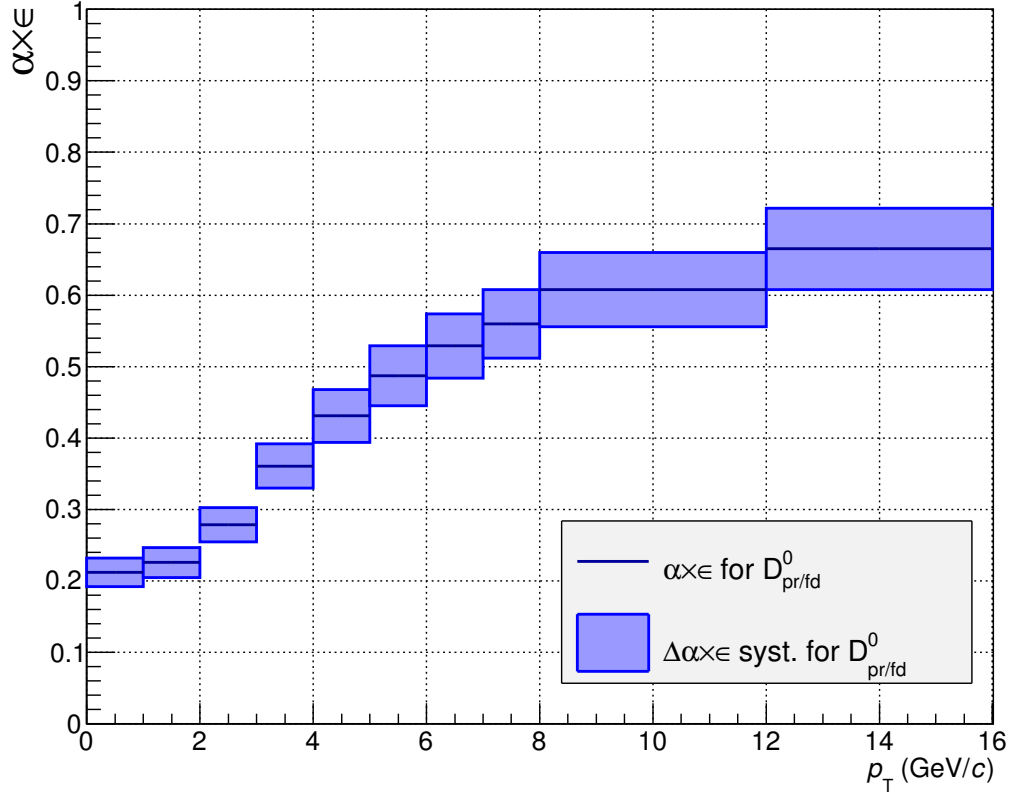
Figure 6.3: Acceptance times efficiency $\alpha \times \epsilon$ for D^0 mesons without a topological selection cut [2]. The systematic errors are shown as boxes. The statistical errors are too small to be depicted.

p_T range (GeV/c)	$N_{\text{raw}}^{\text{not}} \pm$ stat. $\pm$ syst.	$\alpha \times \epsilon \pm$ stat. $\pm$ syst.
0 − 1	$16060 \pm 5102 \pm 1588$	$0.212 \pm 0.001 \pm 0.020$
1 − 2	$27044 \pm 5648 \pm 4804$	$0.226 \pm 0.001 \pm 0.021$
2 − 3	$19294 \pm 3840 \pm 1995$	$0.279 \pm 0.001 \pm 0.024$
3 − 4	$13917 \pm 2244 \pm 2023$	$0.361 \pm 0.001 \pm 0.031$
4 − 5	$5906 \pm 1298 \pm\ \ 771$	$0.431 \pm 0.002 \pm 0.037$
5 − 6	$4418 \pm\ \ 785 \pm\ \ 599$	$0.487 \pm 0.002 \pm 0.042$
6 − 7	$2250 \pm\ \ 508 \pm\ \ 451$	$0.529 \pm 0.003 \pm 0.045$
7 − 8	$1502 \pm\ \ 356 \pm\ \ 291$	$0.560 \pm 0.003 \pm 0.048$
8 − 12	$1629 \pm\ \ 374 \pm\ \ 302$	$0.608 \pm 0.002 \pm 0.052$
12 − 16	$599 \pm\ \ 160 \pm\ \ 154$	$0.665 \pm 0.004 \pm 0.057$

Table 6.2: Values for the raw yield $N_{\text{raw}}^{\text{not}}$ and acceptance times efficiency $\alpha \times \epsilon$ of D^0 mesons without the topological selection cut with their corresponding bin width. The values were taken from [2].

6.2 Theoretical predictions

Theoretical predictions from the FONLL framework are used to estimate the prompt fraction of D^0 mesons in the raw yield. The predicted distributions of the B-hadron $(B^\pm/B^0/B_s^0/\Lambda_b^0)$ admixture shown in Fig. 6.4 are the basis for the simulation of feeddown D^0 mesons and the predicted distributions of prompt D^0 mesons shown in Fig. 8.9 are used for comparative calculations and for the determination of the uncertainties.
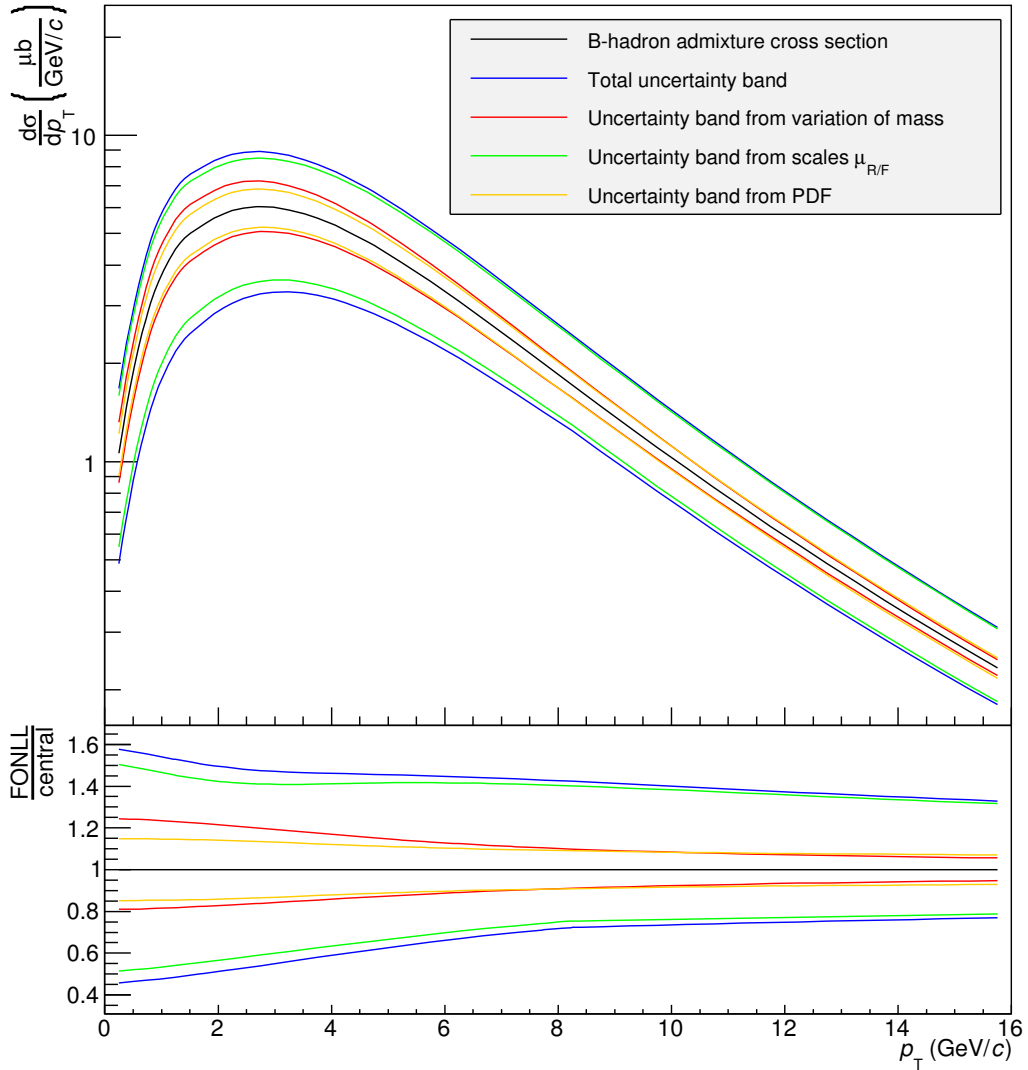

Figure 6.4: FONLL predictions of B-hadron admixture cross section with all uncertainty bands.
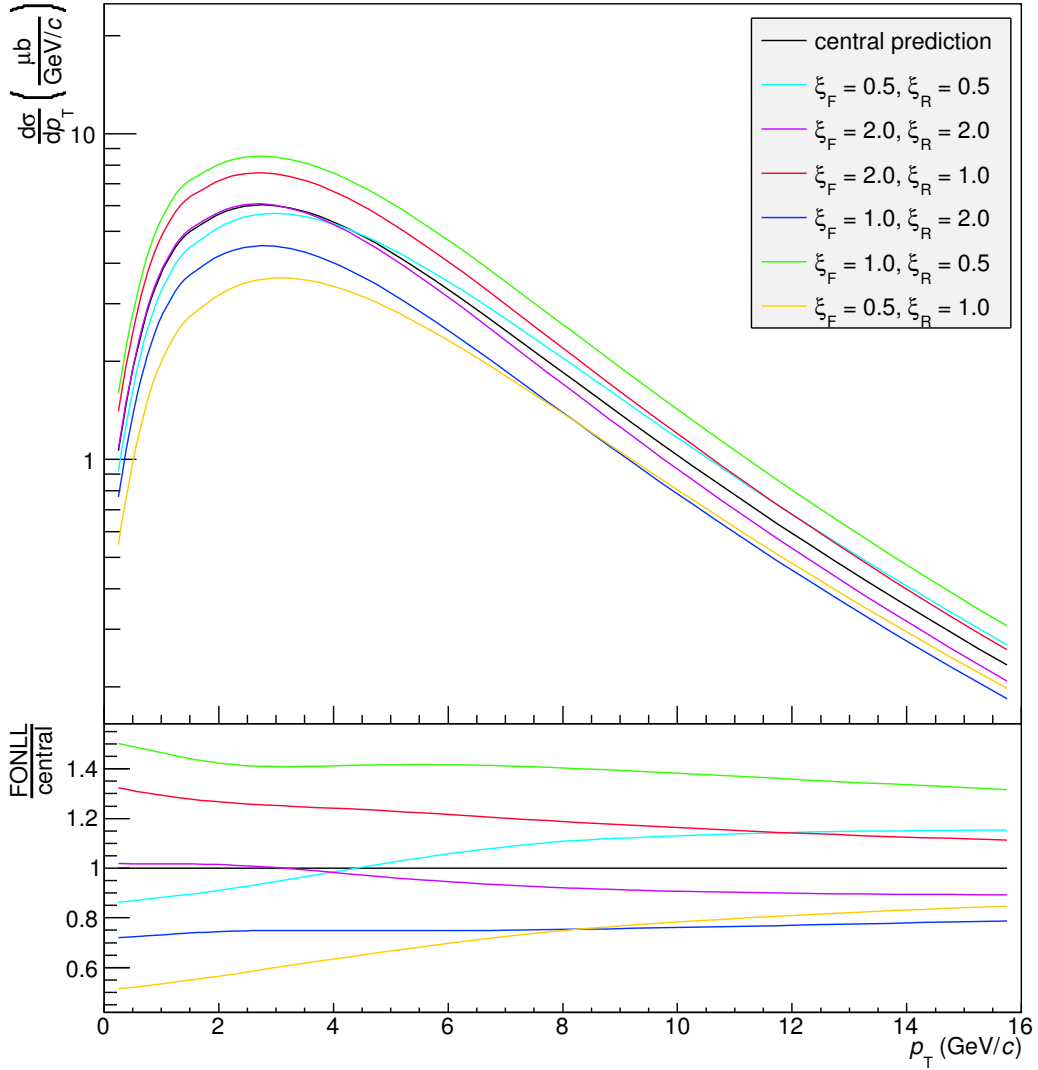
Figure 6.5: FONLL predictions of B-hadron admixture cross section showing the variation of scales.

All predicted distributions are shown in the range of $0 < p_T \leq 16$ GeV/c where the experimental data is provided. The cross section settings of the $B^{\pm}/B^0/B_s^0/\Lambda_b^0$ admixture were put to bottom quark with further decay to the final state of B hadrons at the perturbative order of FONLL. The output of the p_T-differential cross section includes all uncertainties starting at $p_{\text{Tmin}} = 0.25$ GeV/c. The maximum value is then set to high $p_T = 155.25$ GeV/c with 'npoints' at 311. The bin widths are 0.5 GeV/c starting at 0 GeV/c, with the associated values of the cross sections at the

bin center. The choice of a large p_T range is made due to the computation of more exact integrals. The rapidity is set to $|y| \leq 0.5$ as the experimental data is also given at mid-rapidity.

For the propagation of uncertainties it is important for the FONLL predictions of the B-hadron admixture to put out all curves associated with the different uncertainty variations. All of the uncertainty sources, and the total uncertainty as defined in Eq. (23), are depicted in Fig. 6.4. The variation of scales is shown separately in Fig. 6.5. The ratios of the different distributions over the central prediction are also displayed. The variation of scales dominates the total uncertainty band while the uncertainties from the PDFs and the bottom mass are at nearly the same order.

The set-up of the FONLL framework for the prediction of the prompt D^0 differential cross sections is very similar to that for the B-hadron admixture. The quark flavor is set to charm with a further decay to the final state of D^0 mesons. All other settings are the same as before except for the fragmentation fraction of the charm quark to the specific D-meson 'FF$(c \rightarrow D)$'. It is fixed to $f(c \rightarrow D^0) = 0.565$, according to the motivation given in Sect. 3.2.

The distributions of all uncertainty bands for FONLL predictions of the prompt D^0 cross section are shown in Fig. 8.9 and the distributions of the variation of scales in Fig. 6.6. Again the ratios of the different spectra over the central value are also depicted. The contribution of the variation of scales to the total uncertainty is even more dominant for the total uncertainty band of the prompt D^0 distribution than of the B hadrons. The uncertainty band of the prompt D^0 predictions reaches over a range of more than one order of magnitude in the low p_T region and is significantly wider than the uncertatinty band of the B-hadron cross sections.
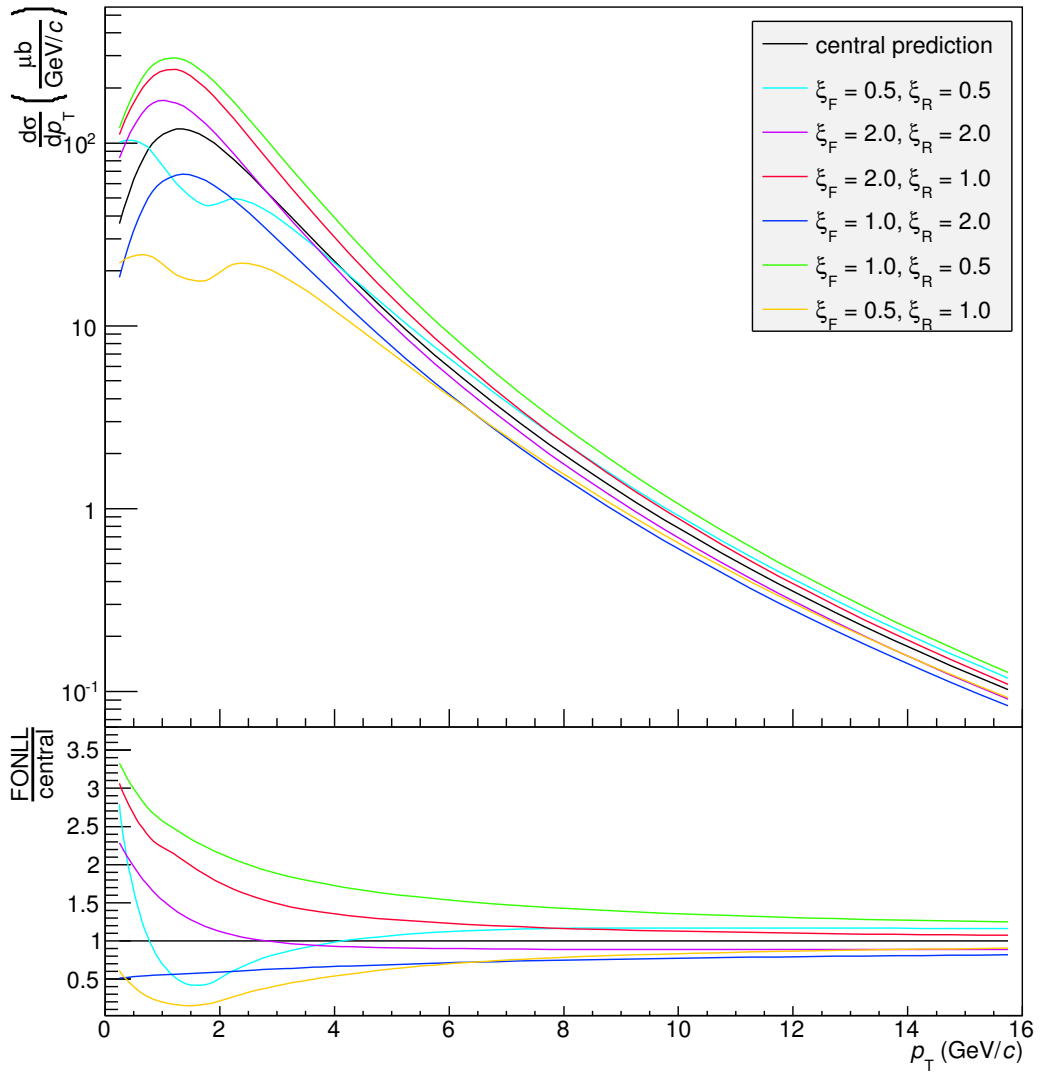
Figure 6.6: FONLL predictions of prompt D^0 meson cross section showing the variation of scales.

7 Pseudorandom number generators

The first step in the analysis of the theoretical data is the simulation of the decay process from the B admixture distribution to the feeddown D^0-meson distribution. The spectra of the B-hadron FONLL predictions are sent through a decay routine, which uses pseudorandom number generators to simulate different random selection processes. Pseudorandom number generators (PRNG) are numerical algorithms that produce uniformly distributed numbers. For an observer not knowing the algorithm the sequence of numbers seems to be random. Nevertheless algorithms are always deterministic and not random. Hence the generated numbers are called 'pseudorandom numbers' (PRN) [33]. The starting values of these PRNG are called 'seeds'.

The pseudorandom numbers are generated in sequences where each PRN is obtained through different transformations from the previous value of the sequence. The transformations should avoid the appearance of statistical autocorrelations. There exist many tests to examine the "randomness" of the PRNG. They evaluate the probability of the PRNG to produce sequences of numbers in a manner as true random number generators would do. True random number generators are based on random natural processes such as radioactive decays [33].

There are different characteristics inherent in a good PRNG [34]:

- large period length,

- uniform distribution,

- fast generation of random numbers,

- portability (same sequences produced independent of the system),

- repeatability, and

- unpredictability (forward and backward sense).

In the following there are two different PRNGs used: the Linear Congruential Generator (LCG) and the Mersenne Twister (MT).

7.1 Linear Congruential Generator

The Linear Congruential Generator was introduced by D.H. Lehmer in 1948 [33]. It is a very simple PRNG with a periodicity of about 10^9 (2^{31}). The recurrence

relation is

$$x_{n+1} = (a\,x_n + c)\,\mathrm{mod}\,m, \tag{26}$$

where x_{n+1} is the sequence of generated values, a is a multiplier with the condition $0 \leq a < m$ and is set to $a = 1103515245$ in the used implementation, c is the increment with the condition $0 \leq c < m$ and is set to $c = 12345$. All of this is modulo $m = 2^{31}$ to get a uniform distribution in the range $]0,1]$. The seed is set to $x_0 = 69069$.

The Linear Congruential Generator is applied in the routine 'GetRandom()' in the histogram class TH1 of the ROOT framework. It returns a PRN distributed in accordance with the initial distribution. Firstly the normalized integral over the bins of the histogram is determined and a PRN is generated by the LCG between 0 and 1. In a binary search the PRN is compared to the integrals of the initial distribution. For that purpose the endpoints of the interval of integration are set to a certain bin number starting with the first bin number. Then the bin number is gradually increased from 1 to the bin number where the integral is at least equal to the PRN or even exceeds it. This bin number is then chosen to ensure that the generated distribution agrees with the underlying distribution and the value of the lower edge of the next bin is selected as return value of the 'GetRandom()' routine.

It is known that the generated values are correlated [34] and therefore not suitable for a good statistical study. Although it is not recommended the LCG is used in the ROOT TH1 class. The application in the simulation of the decay routine in this thesis concerns the distribution which is sent through the decay routine. To evaluate the adaquateness of the LCG the pseudorandomly generated spectrum is compared to the initial spectrum in Sect. 7.3.

7.2   Mersenne Twister

The Mersenne Twister was introduced by M. Matsumoto and T. Nishimura in 1998 [35]. It is based on the principles of the twisted GFSR (general feedback shift register). The recurrence relation is

$$\mathbf{x}_{k+n} = \mathbf{x}_{k+m} \oplus (\mathbf{x}_k^u \mid \mathbf{x}_{k+1}^l)\,A, \qquad (k = 0, 1, ...) \tag{27}$$

where $\mathbf{x}$ denotes word vectors identified with machine words of size w. The generated sequence consists of word vectors uniformly distributed in the range between 0 and $2^w - 1$ and has to be taken modulo $2^w - 1$ to obtain a uniform PRN distribution in the interval [0,1]. The variables k, n, m and r are all integers. The degree of recurrence is given by n, while r and m are in the ranges $0 \leq r \leq w-1$ and $1 \leq m \leq n$, and A is a $w \times w$-matrix containing word vectors denoted with $\mathbf{a}$. The seeds are word vectors $\mathbf{x}_0, \mathbf{x}_1, \ldots, \mathbf{x}_{n-1}$. Firstly the word vector $\mathbf{x}_n$ is determined with $k = 0$. The following word vectors $\mathbf{x}_{n+1}, \mathbf{x}_{n+2}, \ldots$ are generated by gradually increasing $k = 1, 2 \ldots$ If the word vector is $\mathbf{x} = (x_{w-1}, x_{w-2}, \ldots, x_0)$, then $\mathbf{x}^u = (x_{w-1}, \ldots, x_r)$ and $\mathbf{x}^l = (x_{r-1}, \ldots, x_0)$ are the upper (u) and lower (l) bits of $\mathbf{x}$. The concatenation of the upper bits of $\mathbf{x}_k$ and the lower bits of $\mathbf{x}_{k+1}$ is then $(\mathbf{x}_k^u \mid \mathbf{x}_{k+1}^l)$. After the multiplication from right with the matrix A the resulting vector is added bitwise modulo two ($\oplus$) to $\mathbf{x}_{k+m}$ to obtain the successive word vector $\mathbf{x}_{k+n}$ [35].

The Mersenne prime $2^{19937} - 1$ gives not only the period length, but is also the reason for the name 'Mersenne' Twister. Besides the large periodicity of about 10^{6000}, the MT is fast due to only using bitwise operations [34]. It is the PRNG recommended in the ROOT framework reference guide [36]. In the analysis it is applied to randomize the selection of the specific B hadrons in the given $\mathrm{B}^{\pm}/\mathrm{B}^0/\mathrm{B}_\mathrm{s}^0/\Lambda_\mathrm{b}^0$ admixture and the distribution of the rapidity and provides a good level of "randomness".

7.3   Number of trials and statistical uncertainties

Based on the repeatability of the PRNGs the results for different numbers of trials are compared. The statistical behaviour is then analyzed and due to that the number of trials for the decay routine is ascertained. The maximal number of trials may not exceed the predefined limit of the periodicity of the LCG at 10^9. In the statistical analysis the uncertainties are determined by $\sqrt{N}$, where N denotes the number of events. These are counted per bin. The larger the number of trials, the larger the number of events per bin and the smaller the relative error $\sqrt{N}/N$ becomes.

Firstly the results of the LCG are examined. The statistical uncertainties of the experimental data are listed in Tab. 6.1 and 6.2. The smallest statistical uncertainties given are those from $\alpha \times \epsilon$ in Tab. 6.2, with a relative error of at least 0.28%. These relative uncertainties are negligible compared to the relative statistical uncertainties of the raw yields. Thus the statistical uncertainties caused by the PRNGs should

be of the same magnitude or even go below this value. At a number of trials of 10^6 the relative errors should be at the order of $\mathcal{O}(10^{-3})$. So the loop in the macro in which the PRNG is executed is repeated 10^6 times. The results produced by the LCG are compared to the FONLL predictions, which serve as a template for the generated PRNs. For this purpose the ratio of the LCG distribution over the FONLL predictions is formed and depicted in Fig. 7.1. The used values are listed in Tab. A.1 in App. A.

Figure 7.1: The ratio of the distribution produced by the LCG over the FONLL distribution for 10^6 trials. The green area is an approach of the 1σ-region arranged around 1, where an ideal ratio is expected. The black markers show the actual ratio with its statistical uncertainties.

If the number of trials were infinite, an ideal quotient of the result of the LCG over FONLL would be expected to be unity. The expected uncertainty band is calculated by the relative error of each bin

$$\Delta \left(\frac{\text{LCG}}{\text{FONLL}} \right)_{\text{exp}} = \frac{\sqrt{N}}{N}. \tag{28}$$

This is only one approach as it is derived from the number of events of the gener-

ated bins, which are not in accordance to the ideal distribution. It serves merely as orientation for the scattering of the produced distribution. The expected central value of 1 and its uncertainty band are depicted in Fig. 7.1 and 7.2 by the green area.

The quotient $\frac{\text{LCG}}{\text{FONLL}}$ of the generated LCG distribution over the FONLL predictions for each bin is depicted with black markers and statistical error bars. For every restart of ROOT it gives the same results due to the repeatability of the LCG. The associated statistical error is

$$\Delta\left(\frac{\text{LCG}}{\text{FONLL}}\right) = \left(\frac{\text{LCG}}{\text{FONLL}}\right)\frac{\sqrt{N}}{N}. \tag{29}$$

The uncertainty band at a number of 10^6 trials reaches the order of $\mathcal{O}(10^{-2})$ for the B-hadron distribution. The statistical uncertainties of the feeddown D^0 distribution are even larger at higher p_T, as there the number of events per bin is lower than that of the initial B-hadron spectrum. The number of trials is raised to 10^8 to reduce the statistical uncertainties.
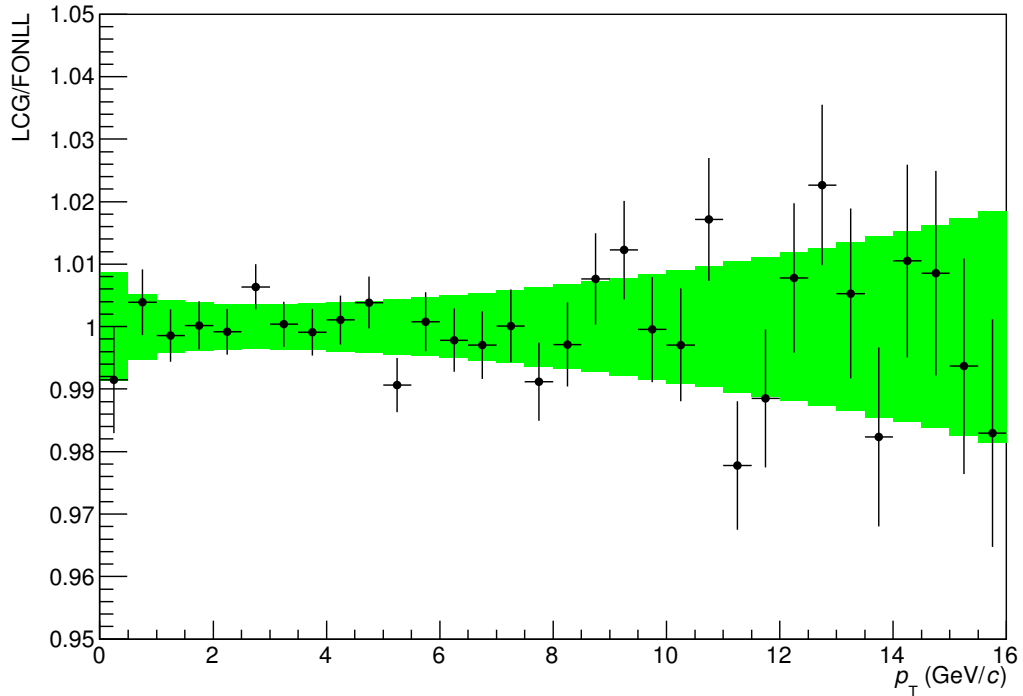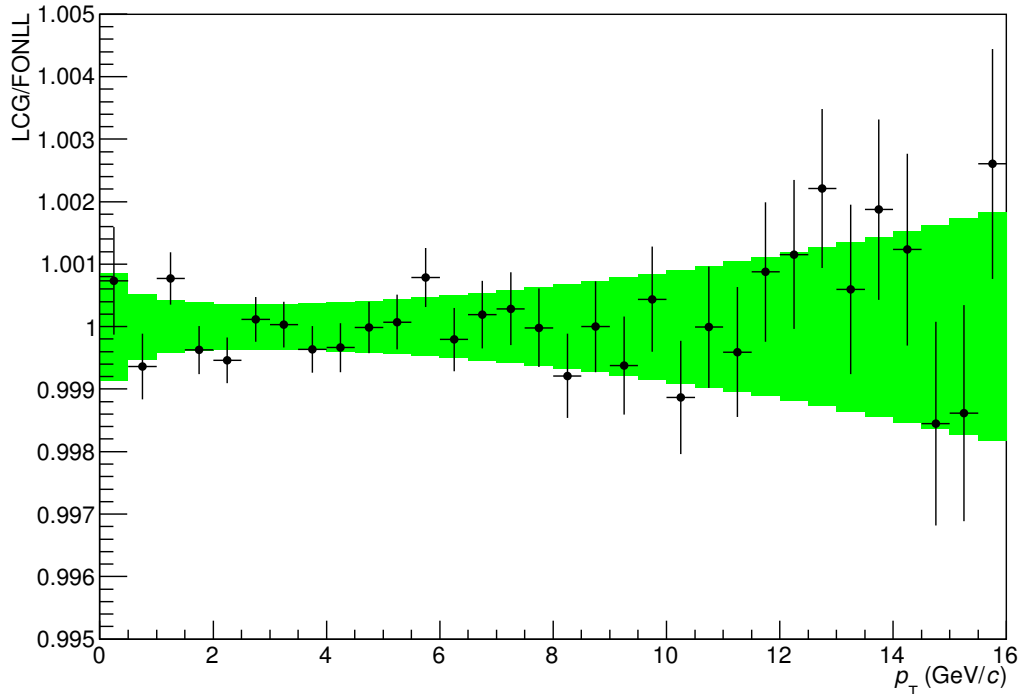

Figure 7.2: The ratio of the distribution produced by the LCG over the FONLL distribution for 10^8 trials.

The used values are again listed in App. A in Tab. A.2. Now the relative statistical uncertainties stay even at high p_T below 0.2%. Thus from the statistical observations of the LCG results a number of trials of 10^8 is chosen.

The distribution of the MT is regarded, too. The same numbers of trials are applied as before. The Mersenne Twister generates randomly distributed numbers between 0 and 1. The conditions to produce a certain B-hadron type are set to the fragmentation fractions given in Tab. 3.1 without consideration of their uncertainties. Then the generated specific B hadrons are separately collected and their distribution is divided bin-by-bin by the associated FONLL bin of the total admixture.
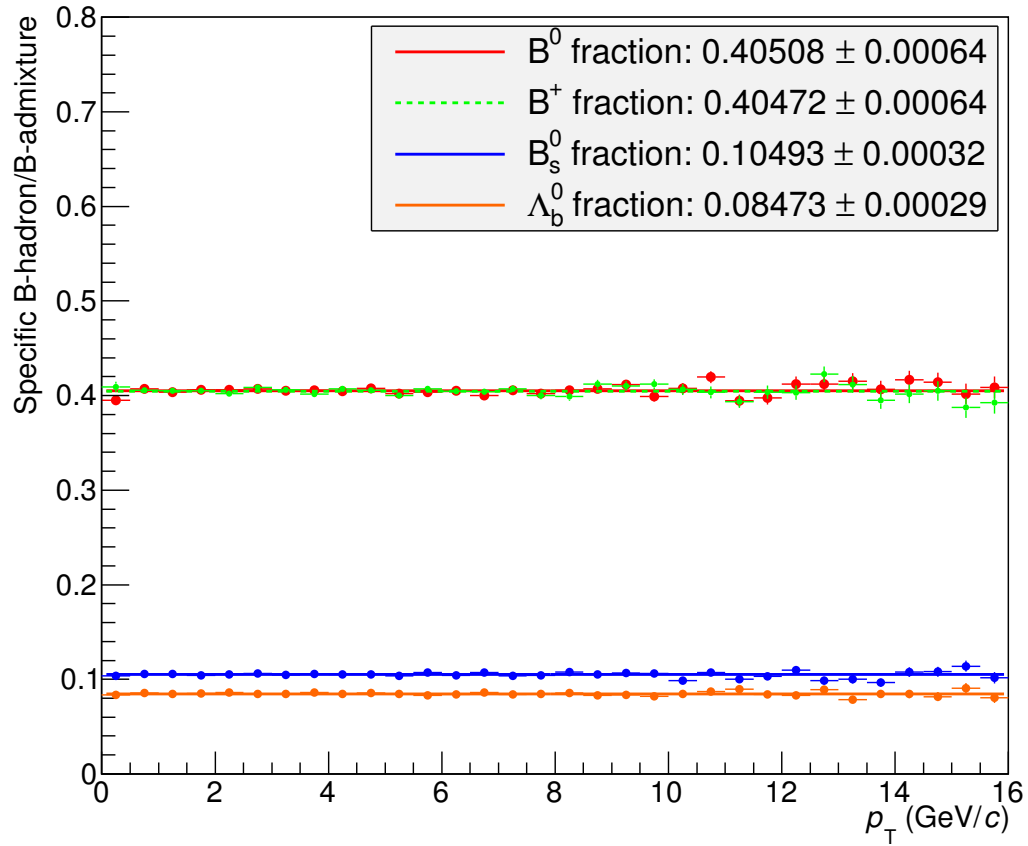

Figure 7.3: Ratio of the distributions of specific B hadrons generated by the MT over the FONLL B-hadron admixture for 10^6 trials. Constant functions are fitted to the ratios. The fit values and corresponding uncertainties are given in the legend.

A constant function is fit to each specific B-hadron ratio to compare the results to the preassigned fragmentation fractions. The fit values of the ratios f^{fit} with their uncertainties are given in the legends of Fig. 7.3 and 7.4, and in Tab. 7.1.
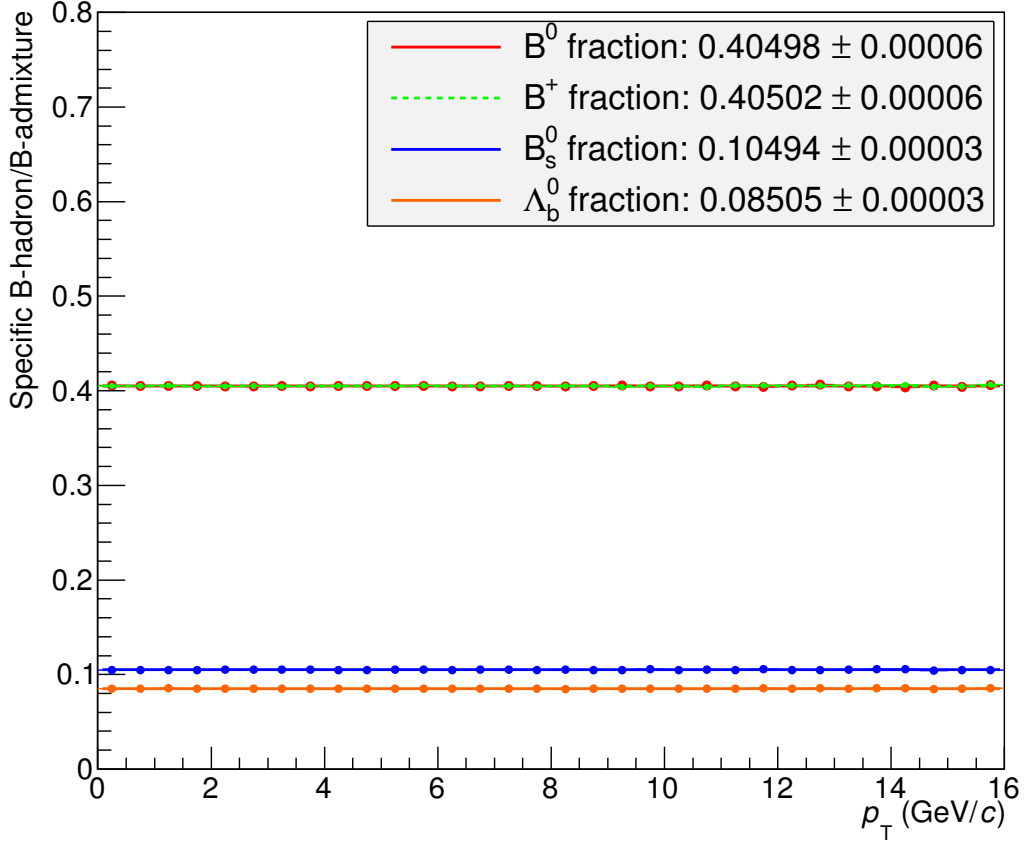
Figure 7.4: Ratio of the distributions of specific B hadrons generated by the MT over the FONLL B-hadron admixture for 10^8 trials. The fits are done in the same way as in Fig. 7.3.

The distribution of each particular B hadron is integrated from 0 to 155 GeV/c. As the distributions are randomized from the normalized $B^{\pm}/B^0/B_s^0/\Lambda_b^0$ admixture spectrum, the integrals directly give the fragmentation fractions f^{int}. The results are listed in Tab. 7.1. The distributions of the particular B hadrons generated from the normalized FONLL B admixture spectrum are depicted in Fig. 7.5.

fragmentation fraction	number of trials: 10^6		number of trials: 10^8	
	$f^{\text{fit}} \pm \text{stat.}$	f^{int}	$f^{\text{fit}} \pm \text{stat.}$	f^{int}
$f(\text{b} \to \text{B}^0)$	0.40508 ± 0.00064	0.40525	0.40498 ± 0.00006	0.40498
$f(\text{b} \to \text{B}^+)$	0.40472 ± 0.00064	0.40486	0.40502 ± 0.00006	0.40503
$f(\text{b} \to \text{B}_s^0)$	0.10493 ± 0.00032	0.10505	0.10494 ± 0.00003	0.10494
$f(\text{b} \to \Lambda_b^0)$	0.08473 ± 0.00029	0.08484	0.08505 ± 0.00003	0.08505

Table 7.1: Values of the fragmentation fractions of the specific B hadrons from the fit and the integrals for comparison and verification
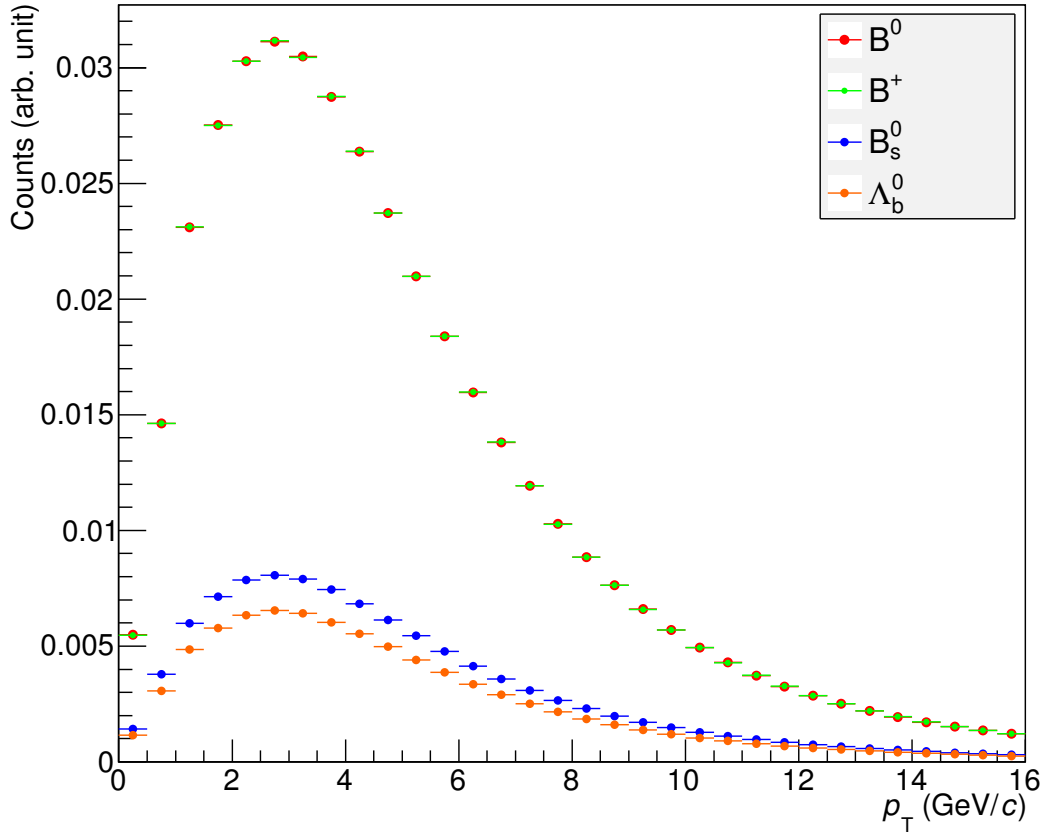

Figure 7.5: Distribution of specific B hadrons generated by the MT for 10^8 trials. The sum of the integrals of the distributions results is unity as the spectra are derived from the normalized FONLL distribution of the B-hadron admixture.

The relative statistical errors for the fit values and the fragmentation fractions are of the order of $\mathcal{O}(10^{-3})$ for 10^6 trials. For the higher number of 10^8 trials the statistical uncertainties diminish to the order of $\mathcal{O}(10^{-4})$. The results of the fits and the integrals agree very well. The Mersenne Twister generates the fragmentation fractions with a high accuracy and negligible statistical uncertainties.

The B^0 and B^+ distributions are nearly identical for 10^8 trials in Fig. 7.4 and 7.5, as expected from the equal fragmentation fractions. The statistical uncertainties (derived from $\sqrt{N}$) in the discrete bins are so small that they are no longer visible.

In conclusion a sample of 10^8 trials is large enough to neglect the statistical uncertainties due to the random generation processes. The pseudorandom number generators preprocess the data correctly for the subsequent decay routine.

8 Analysis of the theoretical predictions

After the introduction to the PRNGs and the evaluation of their contributions to the statistical uncertainties, the decay routine must be performed. Once the feeddown D^0 distribution is generated, it can be used to determine the prompt fractions of the different measured raw yields.

For the analysis the AliRoot framework is used. It is based on the ROOT framework and adapted for the requirements of ALICE. The analysis and presentation of the data in this thesis is mainly performed with ROOT classes. The macros specific for ALICE are only used in the simulation of the decay routine. ROOT is based on C++ and is a powerful tool to process data.

8.1 Decay routine for the feeddown simulation

To facilitate the interface between different analysis tools in particle physics [29] the particles are schematically numbered by the Monte Carlo particle numbering scheme. This allows a basis of communication between different computer programs to be retained. The so-called PDG codes for the decaying B hadrons are 511 (B^0), 521 (B^+), 531 (B_s^0) and 5122 (Λ_b^0). They are key for many further steps such as the read out of the associated masses and other particle properties from the PDG particle tables.

Several steps are taken to process the input data into the output of the feeddown distribution. A flowchart of the routine is shown in Fig. 8.1. The pink parallelograms enclose input and output steps. All the rectangles show the working processes operated within the used macro. Blue rectangles stand for the ROOT processes, the green ones depict AliRoot specific processes. The actual decay is simulated in the external PYTHIA decayer and the associated working flow is highlighted in yellow.

The macro used to generate the decay routine is arranged as follows: The FONLL B-hadron predictions are imported from text files and stored in ROOT histograms. The integrals are then calculated, saved and the B-hadron spectra are normalized. The next steps are all repeated in a loop over the number of 10^8 trials.
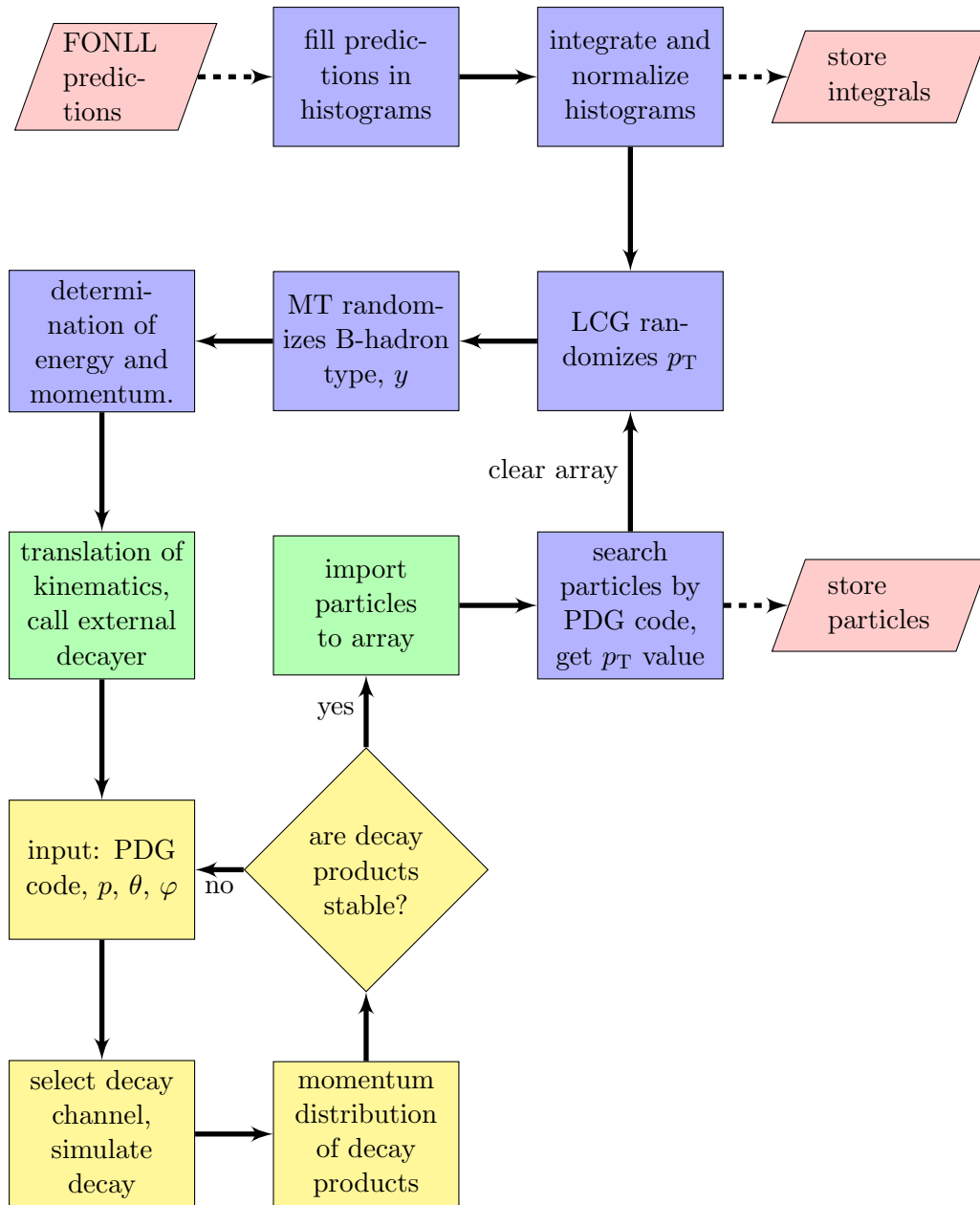
Figure 8.1: Flowchart of the decay routine. The pink parallelograms demonstrate input and output data, the rectangles show key steps of the used macro. The blue rectangles denote that only ROOT tools are applied, the green rectangles mean the use of AliDecayerPythia and the yellow rectangles depict the PYTHIA processes. The large loop is repeated until the number of trials is attained.

The normalized histograms are taken as patterns for the LCG routine to randomly select a certain p_T as the basis for the decay kinematics. The Mersenne Twister randomizes the B-hadron type by means of the PDG code. For the decay the mass of the bottom hadrons is obtained from the particle class TParticlePDG in which the static particle properties are listed. Furthermore the MT produces a PRN distribution for the rapidity in the range $-2 \leq y \leq 2$. The randomly selected p_T, y and PDG code with the associated mass m_{H_b} provide enough information to start the decay routine. For this purpose the general purpose four-vector class TLorentzVector is filled with the corresponding values from the momentum components p_x, p_y, p_z and the energy component E:

$$p_x = p_y = \frac{1}{\sqrt{2}} p_\mathrm{T}, \tag{30a}$$

$$p_z = \tanh y \sqrt{\frac{m_{H_\mathrm{b}}^2 + p_\mathrm{T}^2}{1 - \tanh^2 y}}, \tag{30b}$$

$$E = \sqrt{m_{H_\mathrm{b}}^2 + p_\mathrm{T}^2 + p_z^2}. \tag{30c}$$

To start the decay only the PDG code and the four-vector is needed. The four-vector components are transformed to the momentum and the azimuthal (φ) and polar (θ) angle by the class AliDecayerPythia and then the external PYTHIA6 decayer is called.

PYTHIA is a highly complex and powerful program to generate events in high energy physics. At this point only an outline of the decay routine concerning weak B-hadron decays is given. Further details are given in the "PYTHIA 6.4 Physics and Manual" [37]. Pythia uses a PRNG described in [38] at a periodicity of 10^{43}, which is in line with the chosen number of trials. The decay tables that are used for the feeddown routine in this thesis are given in App. B.

Bottom hadrons decay weakly in semileptonic or hadronic decay channels. All semileptonic and hadronic two-body decays are explicitly given in the program with the associated branching ratios, whereas more-body decays are handled separately. In the semileptonic decays the bottom quark b of the bottom meson H_b decays to an anticharm quark $\bar{\mathrm{c}}$ and two leptons ($l^+ \nu_l$). The spectator quark then combines with the charm quark to one single hadron (H_c). A semileptonic decay of the B^+ meson is depicted in Fig. 8.2. In this case, the up quark is the spectator quark and frag-

ments with the anti-charm quark to form a $\overline{D^0}$ meson. The branching ratio for this channel is given as $\mathcal{B} = (2.27 \pm 0.11)\%$ in [3] and is implemented as $\mathcal{B} = 2\%$ in the database.
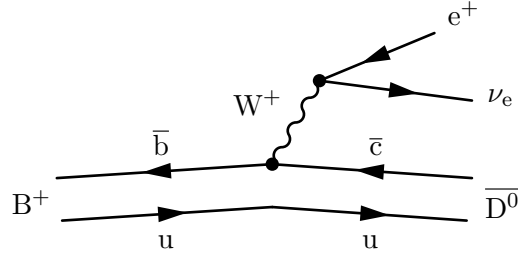

Figure 8.2: Semileptonic decay of a B^+ meson. It decays weakly to a $\overline{D^0}$, a positron and an electron neutrino. The up quark is the so-called spectator quark.

The two-body decays are handled similarly. After the generation of the decay products, their momenta are distributed appropriately in phase space; this process is also handled by the PYTHIA program. More-body decays are listed indirectly in terms of quark contents with their associated branching ratios. Again in the decay simulation the charm quark binds with the spectator quark. Then the momenta distribution for the hadron and the remaining quarks are determined. Thereafter the invariant mass of the remaining quarks is crucial if only one hadron (low invariant mass) or more hadrons (high invariant mass) are formed.

This PYTHIA routine (small loop amongst yellow blocks in Fig. 8.1) is repeated until all decay products are stable. 'Stable' in this case means that the particle is defined as such in the program. Either these are only the default particles (γ, $e^{\pm}$, $\mu^{\pm}$, $\pi^{\pm}$, $K^{\pm}$, K_L^0, p, $\overline{p}$, n, $\overline{n}$ and the neutrinos [37]), or particles that have a decay length $c\tau$ longer than the distance from the interaction point to the detector [39]. Then the particles are all called by the AliDecayerPythia command ImportParticles and stored in an array. Finally a search for the demanded decay products is run. They are filled in a new histogram as a function of their transverse momentum. The array in which the particle data is stored is cleared before the next loop starts.

In the following D^0 denotes both D^0 and $\overline{D^0}$ mesons. If a distinction is made between particle and antiparticle it will be mentioned.

To uncover the momentum distribution hidden in the decay routine the FONLL bottom hadron spectrum is now split into individual bins. Then for each of the first

32 bins the decay routine is executed separately. This is only done for 10^5 trials as it is a rather qualitative contemplation. Then in Fig. 8.3 the p_T distribution of the D^0 mesons is depicted as a function of the transverse momentum of the initial B hadrons. The darker the color in Fig. 8.3, the more D^0 mesons are created. As the D^0 mesons are always produced in conjunction with at least one hadron or two leptons the momentum is distributed amongst these decay products. There is a small probability that the D^0 mesons carry the major fraction of the invariant mass of the initial bottom hadron and arrive at even higher p_T than the initial B hadron.
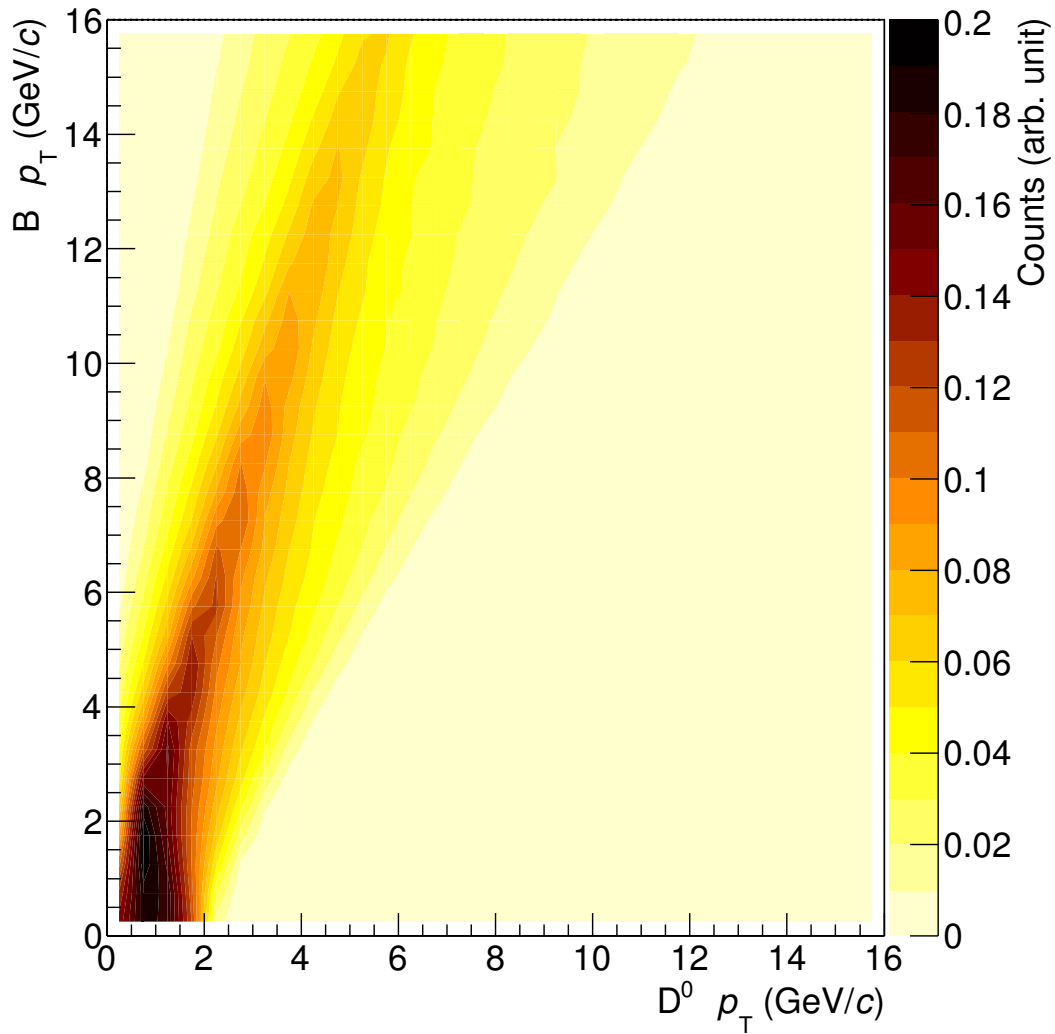

Figure 8.3: Momentum distribution of the feeddown D^0 mesons as a function of the transverse momentum of the initial B hadron.

After integrating over the whole distribution of B hadrons and D^0 mesons the branching ratio $\mathcal{B}(b \to D^0)$ can be determined by dividing the two integrals, resulting in

$$\mathcal{B}(b \to D^0) = 64\%. \tag{31}$$

The particle data booklet does not give an explicit branching ratio for the decay of the $B^{\pm}/B^0/B_s^0/\Lambda_b^0$ admixture but it provides some branching ratios for the specific B hadrons to either both D^0 and $\overline{D^0}$ mesons or explicitly only D^0 or only $\overline{D^0}$. To compare the results of the decay routine the feeddown D^0 mesons are classified by the initial B-hadron type (also called the mother particle). Furthermore they are split into explicitly only D^0 or only $\overline{D^0}$. The combined distributions of mesons and anti-mesons according to their mother particles are presented in Fig. 8.4. Apparently the B^0 and B^+ mesons contribute the major fraction of the D^0 production. Hence only for the total B-hadron admixture, for the B^0 and B^+ mesons the total feeddown production of D^0 mesons is divided into only D^0 and only $\overline{D^0}$ fractions which is shown in Fig. 8.5.
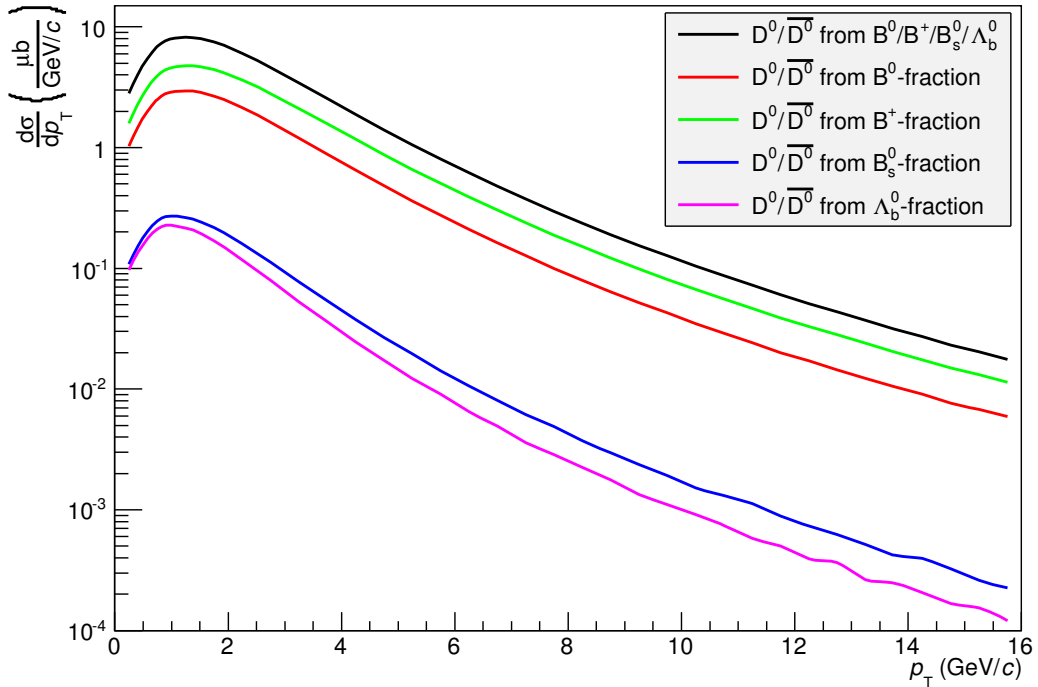
Figure 8.4: Production of both D^0 and $\overline{D^0}$ feeddown mesons as a function of the B-hadron type.
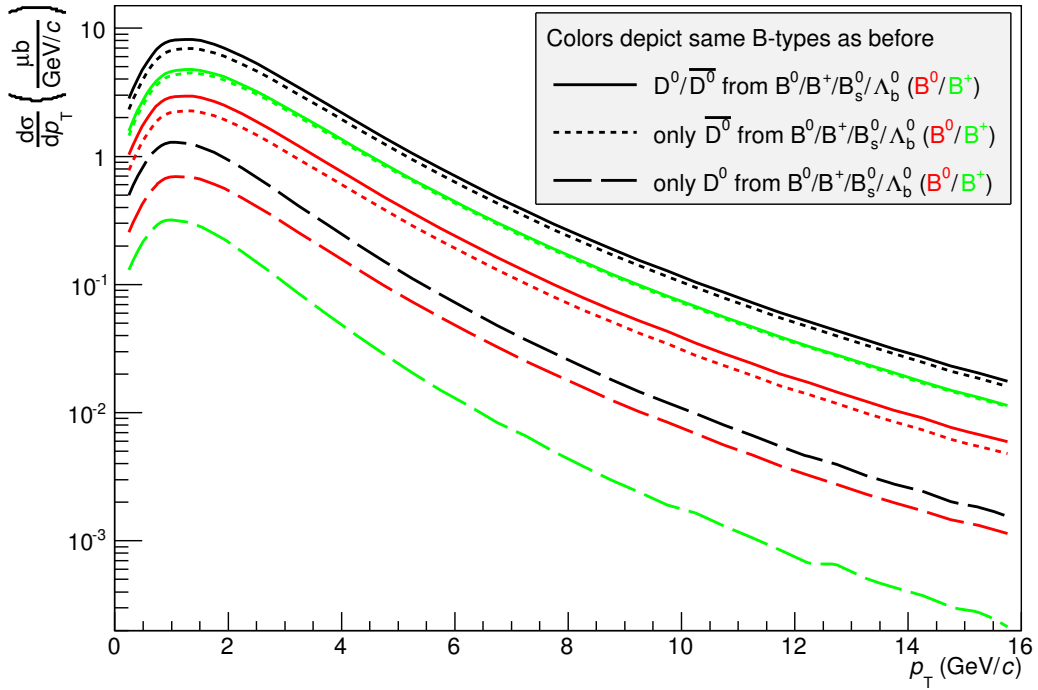
Figure 8.5: Production of both D^0 and $\overline{D^0}$, only D^0 and only $\overline{D^0}$ mesons as a function of the mother particles for the total B-hadron admixture (black), the B^0 (red) and the B^+ (green) mesons.

Again, the integrals of the different distributions are determined. For the total admixture of B hadrons and the D^0 mesons it is computed directly from the distributions. For the specific B hadrons it is scaled by their fragmentation fraction. The integrals are listed in Tab. 8.1.

	B hadron σ (μb)	D^0 and $\overline{D^0}$ σ (μb)	only $\overline{D^0}$ σ (μb)	only D^0 σ (μb)
$B^{\pm}/B^0/B_s^0/\Lambda_b^0$	78.55	50.43	43.48	6.95
B^0	31.81	17.88	13.88	4.01
B^+	31.81	30.08	28.50	1.59
B_s^0	8.25	1.39	0.70	0.69
Λ_b^0	6.68	1.07	0.41	0.66

Table 8.1: Integrals of different B-hadron and D^0 distributions at central rapidity $|y| < 0.5$.

The branching ratios are obtained by dividing the total cross section σ of the desired decay product by the total cross section σ of the mother particle. For the branching ratio of the B^0/B^+ admixture $\mathcal{B}(B^0/B^+ \to D^0/\overline{D^0})$ the literature assumes that the fragmentation fraction is $f(b \to B^0/B^+) = 100\%$. Thus the cross section of B^0/B^+ takes on the value of the cross section of the total B-hadron admixture. The cross sections of the decay from B^0 and B^+ to D^0 and $\overline{D^0}$ are added up and divided by the cross section of the total B admixture. The results are listed in Tab. 8.2.

$\mathcal{B}$ for decay channel	PYTHIA (%)	PDG 2015 (%)
$b \to \overline{D^0} + X$	55.4	59.0 ± 2.9
$B^0/B^+ \to D^0/\overline{D^0} + X$	61.1	61.8 ± 2.9
$B^0 \to \overline{D^0} + X$	43.6	47.4 ± 2.8
$B^0 \to D^0 + X$	12.6	8.1 ± 1.5
$B^+ \to \overline{D^0} + X$	89.6	79.0 ± 4.0
$B^+ \to D^0 + X$	5.0	8.6 ± 0.7
$B_s^0 \to D^0/\overline{D^0} + X$	16.8	
$\Lambda_b^0 \to D^0/\overline{D^0} + X$	16.0	

Table 8.2: Branching ratios of the different mother particles to the D^0 or $\overline{D^0}$ or both mesons where b is equivalent with the $B^\pm/B^0/B_s^0/\Lambda_b^0$ admixture. The values of the decay routine simulated with PYTHIA6 are compared to the recently published values of the PDG [3].

The branching ratios generated with PYTHIA are in agreement with the values from literature. Only the branching ratio $\mathcal{B}(B^+ \to D^0 + X)$ deviates from the value given in the PDG by more than 3σ. For B_s^0 and Λ_b^0 only a few decay channels with D^0 or $\overline{D^0}$ are listed in the PDG particle lists. Therefore no comparison can be made with the comparatively large fraction of simulated D^0 mesons. But as they contribute only 10.5% and 8.5% to the feeddown distributions, their fraction of the total D^0 feeddown distribution is only about 1–2%. Still one can take a closer look at the branching ratios used in the decay simulation.

In the PYTHIA6 decay routine a large number of D^0 mesons is produced in the more-body decays. The more-body decays account for about 62% of all decay channels of each of the four B hadrons. In the B^+ decays the up quark is the spectactor quark so a large number of D^0 mesons can be produced. According to the particle database (see App. B) at least 50% of all the decay channels of B^+ must be a more-

body decay with a spectator up quark that fragments with an anti-charm quark to a $\overline{\mathrm{D}^0}$ meson. As the spectator quarks of the other B hadrons can not form a D^0 meson, the other participiants in the more-body decay must also provide a large fraction of the D^0 mesons. Having a look at the remaining quarks in the more-body decays that do not hadronize with the spectator flavor a considerable number of decays could still produce a D^0 meson. These more-body decays that potentially produce D^0 mesons represent about 17.5% of all decay channels.

Obviously the more-body decay brings forth the large number of D^0 mesons in the B_s^0 and Λ_b^0 decays. This is experimentally proven for neither of the particles. However the simulation of the decay routine of the total B-hadron admixture provides a good result comparable to the branching ratios given in literature.

8.2 Comparison between feeddown results of PYTHIA and EvtGen

In the reference publication [1] the feeddown of the FONLL B distribution to D^0 mesons is simulated by the EvtGen particle decay simulation package [40] instead of PYTHIA. There it is stated that the differences between PYTHIA and EvtGen are negligible with respect to the systematic uncertainties from the FONLL predictions. This is taken as reference to compare both external decayers by the decay of only the central prediction of the FONLL B-hadron cross sections. As the computing time of the EvtGen package is significantly larger than for PYTHIA, only 10^6 trials are run for the EvtGen decay routine. This leads to larger statistical uncertainties. So while the statistical errors of the PYTHIA feeddown distribution (10^8 events) are neglected, those of the EvtGen feeddown distribution are propagated within the comparison.

Both feeddown D^0 distributions are shown in Fig. 8.6. At higher transverse momenta the EvtGen distribution fluctuates due to the smaller sample size. The values of the EvtGen feeddown cross sections are marginally lower than the values of the PYTHIA feeddown cross sections. This is evaluated by dividing the EvtGen distribution by the PYTHIA distribution as it is depicted in Fig. 8.7. The error bars are the statistical uncertainties $\Delta \frac{\mathrm{EG}}{\mathrm{PY}}$ propagated from the $\sqrt{N}/N$ of each bin of the EvtGen

distribution. This is done by

$$\frac{\text{EG}}{\text{PY}} = \frac{\dfrac{\mathrm{d}\sigma^{\text{EG}}}{\mathrm{d}p_{\text{T}}}}{\dfrac{\mathrm{d}\sigma^{\text{PY}}}{\mathrm{d}p_{\text{T}}}}, \tag{32a}$$

$$\Delta\frac{\text{EG}}{\text{PY}} = \frac{\sqrt{N}}{N} \cdot \frac{\text{EG}}{\text{PY}} = \sqrt{\frac{2 \cdot \sigma_{\text{tot}}^{\text{B}}}{10^6 \cdot \frac{\mathrm{d}\sigma^{\text{EG}}}{\mathrm{d}p_{\text{T}}}}} \cdot \frac{\text{EG}}{\text{PY}}, \tag{32b}$$

where $\frac{\mathrm{d}\sigma^{\text{EG}}}{\mathrm{d}p_{\text{T}}}$ denotes the cross sections of the EvtGen feeddown and $\frac{\mathrm{d}\sigma^{\text{PY}}}{\mathrm{d}p_{\text{T}}}$ the cross sections of the PYTHIA feeddown. The factor of 2 includes the p_{T} bin width of 0.5 GeV/c, $\sigma_{\text{tot}}^{\text{B}}$ is the total cross section of the input B spectrum and 10^6 is the number of trials in the EvtGen simulation.
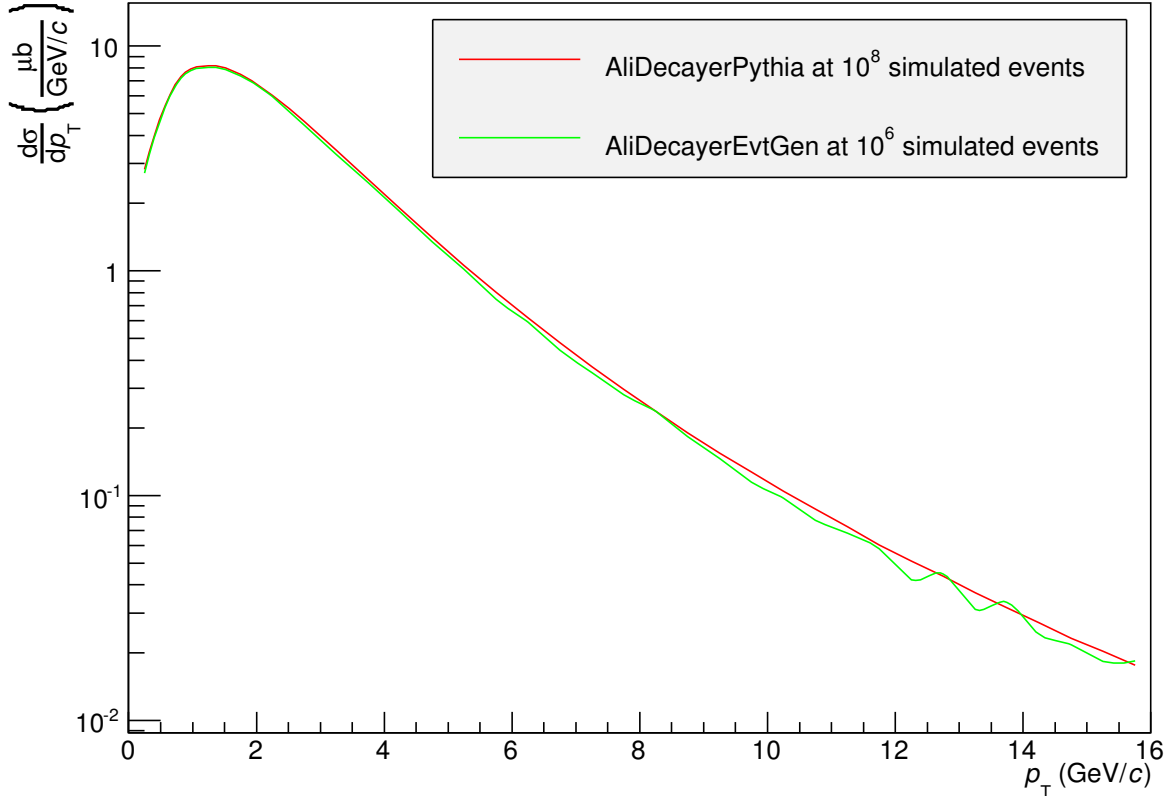

Figure 8.6: D^0 feeddown distributions from the EvtGen decay simulation (green) at 10^6 events and from the PYTHIA decay routine (red) at 10^8 events.
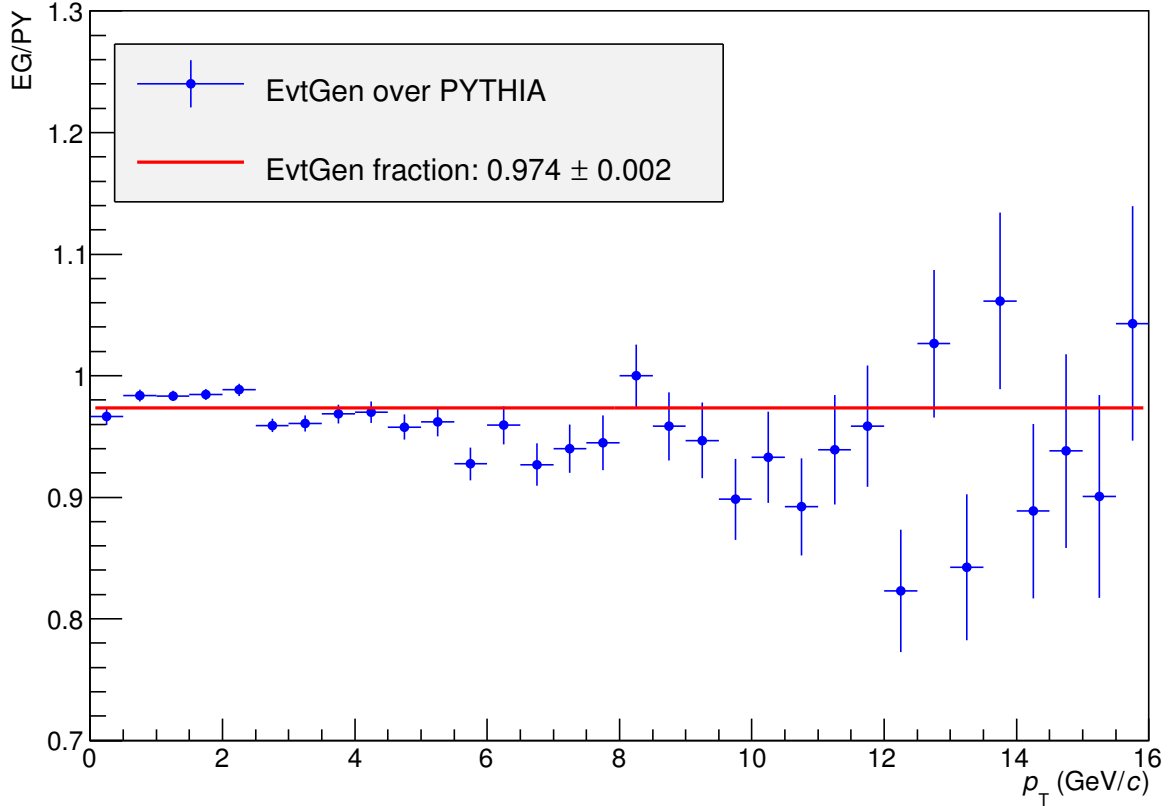
Figure 8.7: The ratio of the D^0 feeddown distributions of EvtGen over PYTHIA is depicted by the blue markers. Then a line of best fit is drawn in the ratio of the distribution to estimate the deviation of the EvtGen results from those generated by PYTHIA.

A line of best fit is drawn in the ratio plot to estimate the offset of the EvtGen results as compared to the PYTHIA results. The EvtGen package generates B-hadron decays to D^0 at cross sections that are about 3 % lower than those produced by the PYTHIA program. This offset tends to be smaller at low p_T and larger at higher p_T. Although this difference is effectively negligible compared to the large systematic uncertainties due to the theoretical predictions as stated in [1], one can have a closer look at the branching ratios generated by the EvtGen package. This was done for the PYTHIA routine in the section above with the branching ratios given in Tab. 8.2. For the EvtGen routine they are listed in Tab. 8.3. The total branching ratio including both D^0 and $\overline{D^0}$ is

$$\mathcal{B}(b \rightarrow D^0) = 62.5\%. \tag{33}$$

$\mathcal{B}$ for decay channel	EvtGen (%)	PDG 2015 (%)
$b \to \overline{D^0} + X$	51.0	59.0 ± 2.9
$B^0/B^+ \to D^0/\overline{D^0} + X$	60.5	61.8 ± 2.9
$B^0 \to \overline{D^0} + X$	41.4	47.4 ± 2.8
$B^0 \to D^0 + X$	17.8	8.1 ± 1.5
$B^+ \to \overline{D^0} + X$	82.0	79.0 ± 4.0
$B^+ \to D^0 + X$	8.2	8.6 ± 0.7
$B^0_s \to D^0/\overline{D^0} + X$	18.7	
$\Lambda^0_b \to D^0/\overline{D^0} + X$	0.2	

Table 8.3: Branching ratios of the different mother particles to the D^0 or $\overline{D^0}$ or both mesons where b is equivalent with the $B^{\pm}/B^0/B^0_s/\Lambda^0_b$ admixture. The values of the decay routine simulated with the EvtGen package are compared to the recently published values of the PDG [3].

All branching ratios of the EvtGen routine are in the 3σ confidence interval of the published data of the PDG [3] except for the branching ratio $\mathcal{B}(B^0 \to D^0 + X)$. The most remarkable difference between the EvtGen and the PYTHIA results (see Tab. 8.2) is the branching ratio of $\mathcal{B}(\Lambda^0_b \to D^0/\overline{D^0} + X)$. The Λ^0_b accounts for 8.5% of the total B-hadron admixture so this significant decrease in the branching ratio compared to PYTHIA reduces the share to the total D^0 feeddown production from about 1.3% (PYTHIA) to only about 0.02% (EvtGen).

The comparison between the EvtGen and the PYTHIA will be continued in the following section when the prompt fraction of the D^0 production is determined. Before, the analysis of the theoretical data has to be performed.

8.3 Comparison of feeddown and prompt FONLL data

The D^0 feeddown distribution retained after processing the decay routine at 10^8 trials is shown in Fig. 8.8 with the FONLL uncertainty bands. The envelope of the variations of scales and the spectra corresponding to the variation of the charm and bottom masses as well as to the variation of the cross sections due to the propagated PDF uncertainties were sent through the decay program individually. Beyond that all distributions due to the variations of scales were sent through the decay routine separately and the associated feeddown distributions are depicted as the lower distribution in the lower panel of Fig. 8.10.
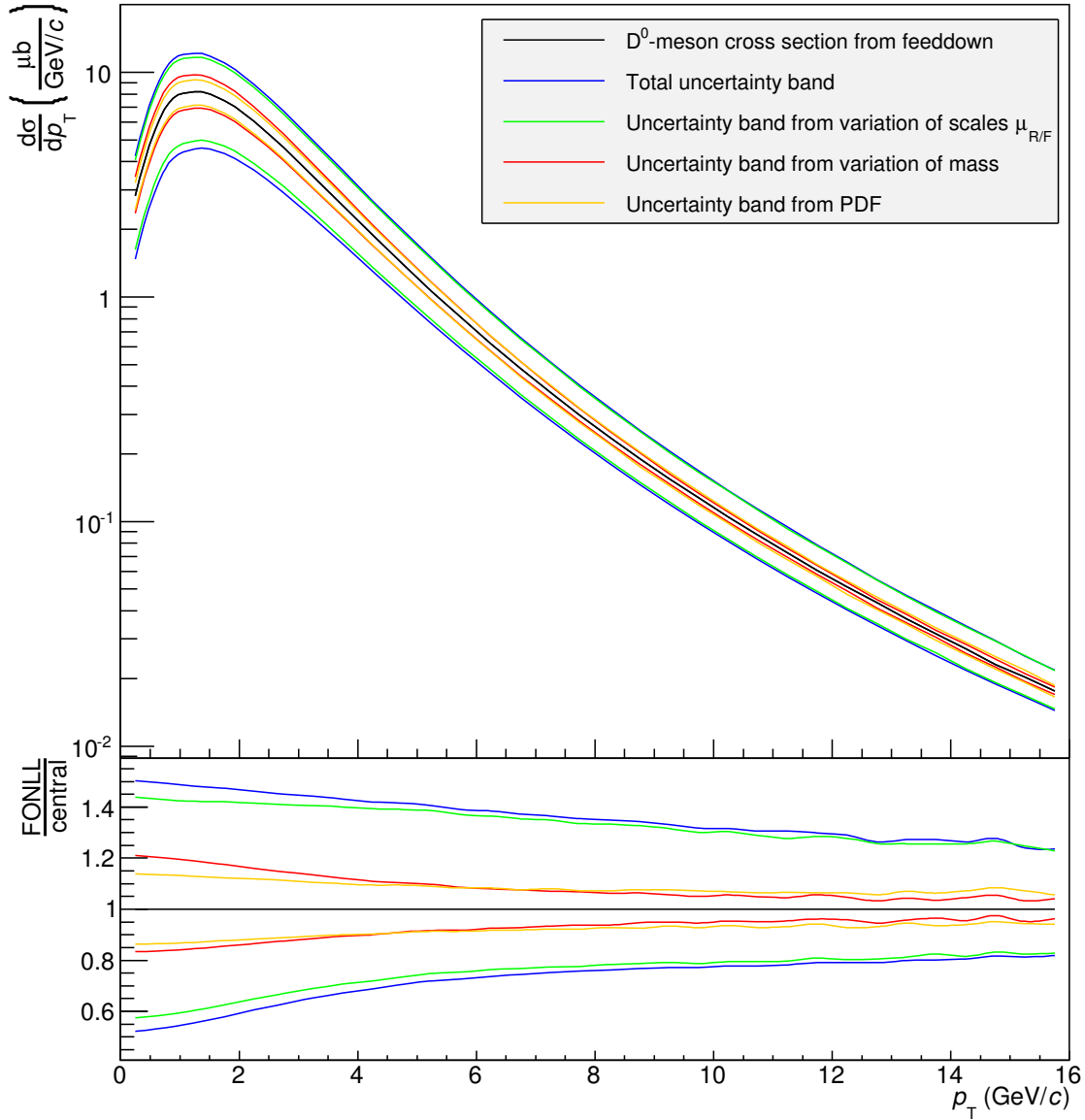
Figure 8.8: Distribution of feeddown D^0 mesons with uncertainty bands inherited from the FONLL B-hadron admixture distribution. All uncertainty bands were sent separately through the decay routine. The fluctuation at higher p_T is due to statistical effects of the simulation.

The statistical uncertainties are neglected. The ratios of the uncertainty bands over the central value give an overview of the relative upper and lower errors. The initial distributions of the B-hadron admixture from which the feeddown D^0 mesons stem

are shown in Fig. 6.4 in Sect. 6.2.

The relative uncertainties show fluctuations in the higher p_T region. These are statistical effects. To recheck the statistical uncertainty, the bin b_{32} with the lowest number of events N is chosen. Its bin center is at $p_T = 15.75$ GeV/c. The number of events is calculated from the p_T-differential cross section $d\sigma^{b_{32}}$ of this bin as follows

$$N = w^{b_{32}} \cdot \frac{d\sigma^{b_{32}}}{p_T} \cdot \frac{n_{\text{trials}}}{\sigma^B_{\text{tot}}}, \tag{34}$$

where $w^{b_{32}} = 0.5$ GeV/c is the bin width, $n_{\text{trials}} = 10^8$ is the number of trials, and σ^B_{tot} is the total cross section of the initial B admixture. This leads to $N = 22435$ events and a relative error of about 0.7%. Due to the rather large statistical errors from the experimental data as well as the large systematic uncertainties, the statisical uncertainties from the decay routine can be neglected.

The prediction of the distribution of prompt D^0 mesons is generated with the FONLL framework [14] and shown in Fig. 8.9 with the uncertainty bands. The individual variation of scales are contained as the upper distribution in the lower pad of Fig. 8.10. In comparison to the feeddown distribution, where the uncertainties are inherited from the B-hadron predictions, the uncertainties are spread over a significantly wider range. The prompt uncertainties deviate by more than one order of magnitude and vary in a large range. The feeddown uncertainty bands are not only smaller but also steadier showing only a little decrease with increasing momentum.

To get a general idea of the relation between the prompt and feeddown distributions and their uncertainty bands both are depicted together in Fig. 8.10. Making a rough estimate the feeddown fraction represents about 10% of the prompt fraction.

Two different methods of error propagation are applied for further analysis. When the feeddown spectrum is combined with experimental data the total uncertainty band as depicted in blue in Fig. 8.8 is propagated as the systematic uncertainty. When the feeddown data is combined with the prompt FONLL distribution the error propagation is more difficult and the different uncertainties are regarded separately to avoid correlations.
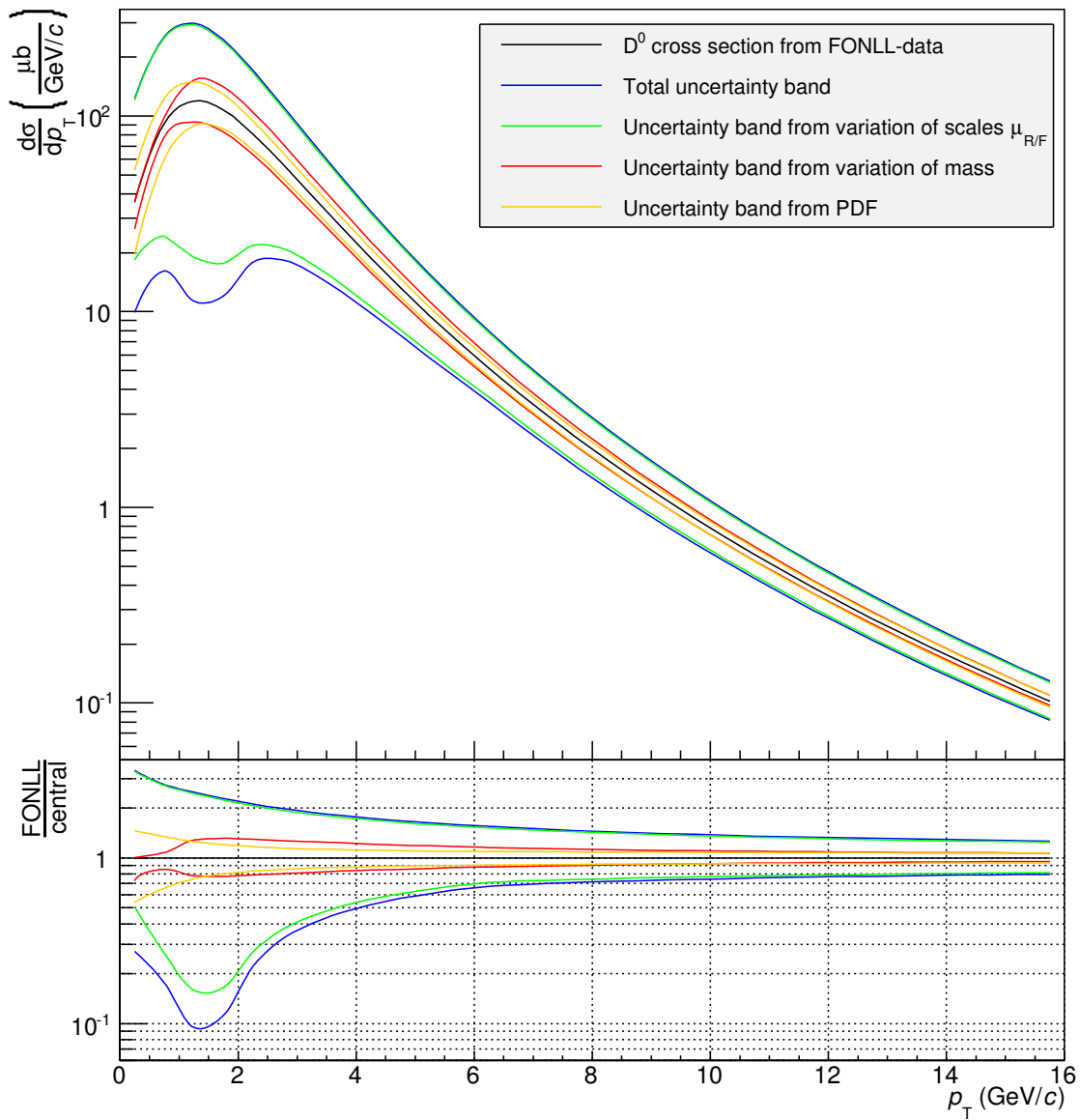
Figure 8.9: Distribution of prompt D^0 mesons with uncertainty bands predicted by the FONLL framework. Due to the variation of scales the uncertainties spread over more than one order of magnitude.
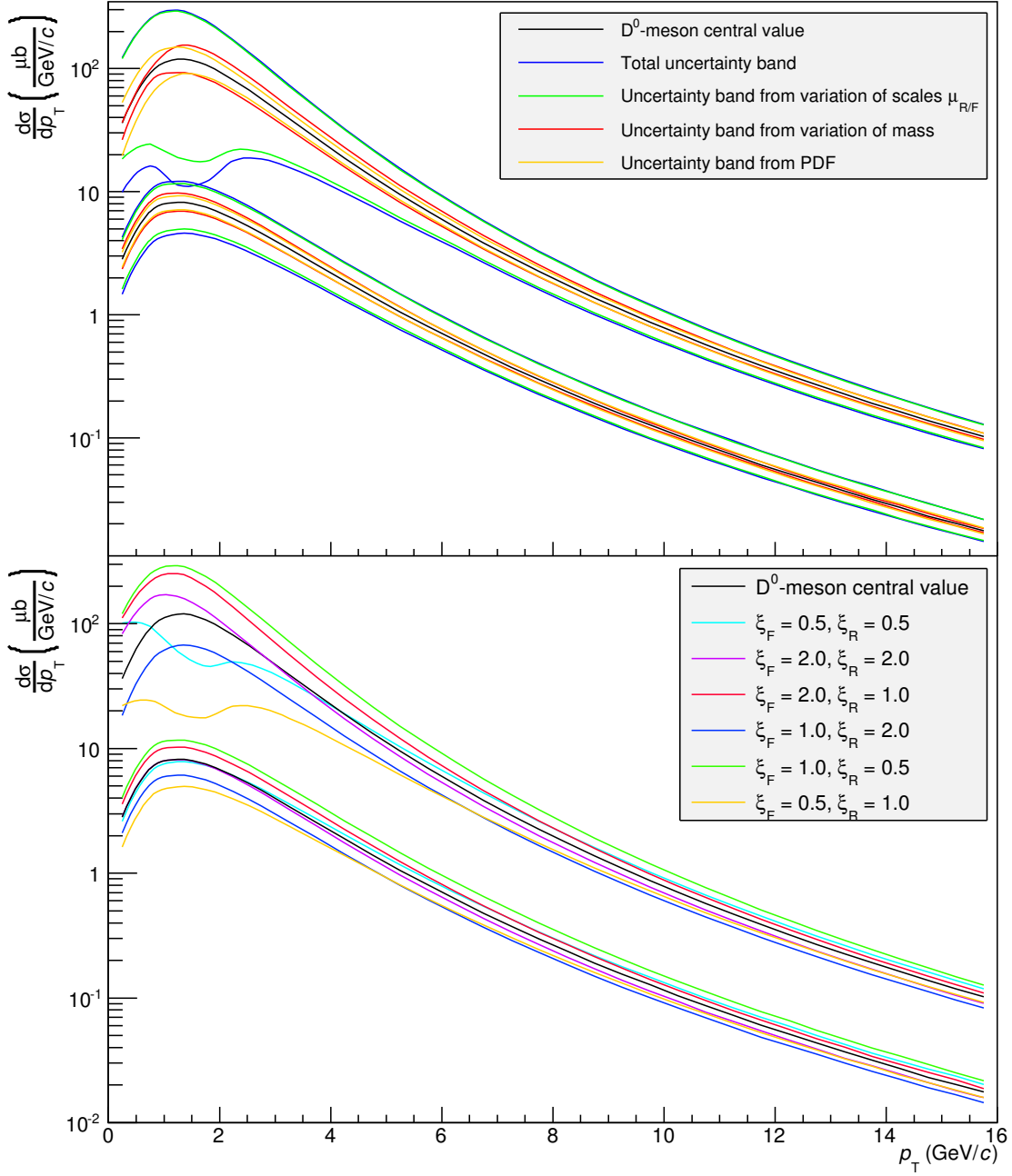
Figure 8.10: Overview of the distributions of prompt and feeddown D^0 mesons with uncertainty bands. In both panels the upper distributions are the prompt D^0 spectra from FONLL predictions and the lower distributions are the feeddown D^0 spectra. The upper panel contains the central prediction with all uncertainty bands while the lower panel shows the variation of scales.

9   Determination of the prompt fraction of D^0 mesons

D^0 mesons are measured based on the reconstruction of $D^0 \to K^-\pi^+$ (and their charge conjugates). The decay is shown in Fig. 9.1 and it has the branching ratio $\mathcal{B} = 3.93 \pm 0.04\%$ [3]. Kaons and pions are charged mesons that can be detected very well with the ALICE detectors. Particle identification (PID) takes place in the Time Of Flight detector (TOF) and in the Time Projection Chamber (TPC), which were mentioned in Sect. 2.
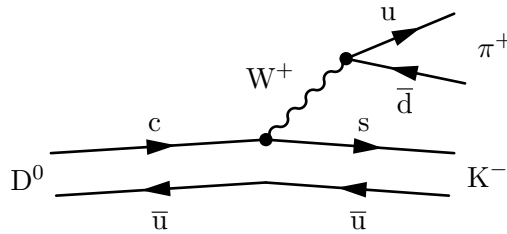

Figure 9.1: Measured and reconstructed decay channel of D^0 mesons. The D^0 meson decays weakly to a K^- and a π^+.

In the selection of data no proper distinction is made between D^0 mesons ($c\tau \approx$ 120 μm) from prompt charm quark production and the D^0 feeddown candidates from the decays of B mesons and the Λ_b^0 baryon. The topological cuts in the selection of one of the data sets only excludes secondary vertices that are closer ($< 100\mu$m) to the primary vertex than the D^0 vertices from prompt charm quark production are expected to be. As the B hadrons possess significantly larger decay lengths ($c\tau \approx 440$–490 μm) their contribution N_{fd} to the measured raw yield N_{raw} of D^0 mesons must be subtracted to obtain the prompt fraction f_{prompt} of the measured raw yield of D^0 mesons. If N_{pr} is the yield of prompt D^0 mesons produced in the collision, the prompt fraction is

$$f_{\mathrm{prompt}}^{\mathrm{data}} = \frac{N_{\mathrm{pr}}}{N_{\mathrm{raw}}} = \frac{N_{\mathrm{raw}} - N_{\mathrm{fd}}}{N_{\mathrm{raw}}} = 1 - \frac{N_{\mathrm{fd}}}{N_{\mathrm{raw}}}. \tag{35}$$

This relation is used to determine the prompt fraction in experimental data. The measured raw yields $N_{\mathrm{raw}}^{\mathrm{top}}$ of the topological analysis and $N_{\mathrm{raw}}^{\mathrm{not}}$ of the analysis without topological cuts are listed in Tab. 6.1 and 6.2. The feeddown contribution is defined by the distribution shown in Fig. 8.8. It is derived from the theoretical FONLL B-hadron cross section predictions via the decay routine and given as the

63

p_T-differential cross section $\dfrac{\mathrm{d}\sigma_{\mathrm{fd}}}{\mathrm{d}p_T}$ in the rapidity range $|y| < 0.5$. It is converted to the yield of feeddown D^0 mesons as follows:

$$N_{\mathrm{fd}}\big|_{|y|<y_{\mathrm{fid}}} = 2 \cdot 2\,|y_D| \cdot \Delta p_T \cdot (\alpha \times \epsilon) \cdot \mathcal{B} \cdot \mathcal{L}_{\mathrm{int}} \cdot \left.\frac{\mathrm{d}\sigma_{\mathrm{fd}}}{\mathrm{d}p_T}\right|_{|y|<0.5}. \tag{36}$$

The first factor of two is due to considering both particles (D^0) and antiparticles ($\overline{D^0}$). The fiducial acceptance cut $|y_D|$ is given in Eq. (25) and shown in Fig. 6.1 for the topological analysis and it is given as 0.8 for the non-topological analysis. The factor of two on $|y_D|$ is due to the rapidity of the cross section being scaled linearly from $|y| < 0.5$ to $|y| < y_{\mathrm{fid}}$, where y_{fid} varies between 0.5 and 0.8 in the topological analysis. The yield is determined in separate p_T intervals, with Δp_T denoting the bin width. The acceptance times efficiency $(\alpha \times \epsilon)$ is taken from the feeddown values given in Tab. 6.1 for the analysis where the topological cuts are made, and from the values given in Tab. 6.2 for the non-topological analysis. The branching ratio $\mathcal{B}$ is given above and the integrated luminosities are $\mathcal{L}_{\mathrm{int}} = 5.0 \text{ nb}^{-1}$ for the topological analysis, and $\mathcal{L}_{\mathrm{int}} = 5.25 \text{ nb}^{-1}$ for the non-topological analysis, as quoted in Sect. 6.1.

The prompt fraction of the produced D^0 mesons is determined from experimental data (N_{raw}) in combination with theoretical predictions (N_{fd}) in Eq. (35). To compare the results to the theoretical predictions and to estimate the systematic uncertainty as was done in [1], an alternative method is used to determine the prompt fraction:

$$f_{\mathrm{prompt}}^{\mathrm{FONLL}} = \left(1 + \frac{N_{\mathrm{fd}}}{N_{\mathrm{pr}}}\right)^{-1} = \left(1 + \frac{(\alpha \times \epsilon)_{\mathrm{fd}}}{(\alpha \times \epsilon)_{\mathrm{pr}}} \frac{\left.\frac{\mathrm{d}\sigma_{\mathrm{fd}}}{\mathrm{d}p_T}\right|_{|y|<0.5}}{\left.\frac{\mathrm{d}\sigma_{\mathrm{pr}}}{\mathrm{d}p_T}\right|_{|y|<0.5}}\right)^{-1}. \tag{37}$$

The p_T-differential cross sections $\dfrac{\mathrm{d}\sigma_{\mathrm{pr}}}{\mathrm{d}p_T}$ of the prompt D^0 mesons are the FONLL pQCD predictions which are shown in Fig. 8.9. The p_T-differential cross sections $\dfrac{\mathrm{d}\sigma_{\mathrm{fd}}}{\mathrm{d}p_T}$ are the same as in Eq. (35). Thus, only p_T-differential cross sections based on the pQCD predictions are considered for this method. They are combined with their respective $\alpha \times \epsilon$. In the analysis without topological cuts, the same acceptance and efficiencies $(\alpha \times \epsilon)$ for the prompt and feeddown D^0 mesons are applied. So the

ratio of acceptance times efficiencies cancels, and the remaining term contains only the p_T-differential cross sections of the prompt and feeddown FONLL distributions.

The theoretical predictions are given in a uniform binning. The experimental data and the acceptances times efficiencies are provided in a different binning of increasing bin widths. So the FONLL distributions are all rebinned before further calculations are done. The new bins are

$$b_n^r = \frac{w^o}{w^r} \sum_{m=i}^{nk} b_m^o, \qquad i = (n-1)k + 1 \qquad (38)$$

and have the bin width w^r. The old bins b^o have the bin width $w^o = 0.5$ GeV/c and the upper bound of the summation is $nk = n\frac{w^r}{w^o}$. The indices n and m give the number of the new and the old bin, respectively, and are integers. The ratio of the bin widths and accordingly k are also integers. If the width of the new bin changes, the old indices m and n have to be added to the new indices m' and n' (both starting at 1). The new bins are then $b_{n+n'}^r = \frac{w^o}{w^r} \sum_{m'=i}^{n'k} b_{m+m'}^o$ with $i = (n'-1)k+1$.

After the rebinning, the prompt fraction is determined bin-by-bin according to the formulas given above.

9.1 Propagation of statistical uncertainties

The statistical uncertainties are propagated by adding them in quadrature. For the analysis with topological selection cuts the statistical uncertainty of $f_{\text{prompt}}^{\text{data}}$ is

$$\Delta(f_{\text{prompt}}^{\text{data, stat.}}) = \frac{N_{\text{fd}}}{N_{\text{raw}}} \cdot \sqrt{\left(\frac{\Delta N_{\text{raw}}^{\text{stat}}}{N_{\text{raw}}}\right)^2 + \left(\frac{\Delta(\alpha \times \epsilon)_{\text{fd}}^{\text{stat}}}{(\alpha \times \epsilon)_{\text{fd}}}\right)^2}. \qquad (39)$$

In the case of the non-topological selection of events the statistical uncertainty of the acceptance times efficiencies is negligible and the last term in the square root is dropped.

The propagation of statistical uncertainties for $f_{\text{prompt}}^{\text{FONLL}}$ is only regarded in the analysis with topological selection as the FONLL predictions carry no statistical uncertainties, and the simulation uncertainties and the statistical uncertainties of the $\alpha \times \epsilon$ of the non-topological selection cuts are negligible. The statistical uncertainty

is

$$\Delta(f_{\text{prompt}}^{\text{FONLL, stat.}}) = (f_{\text{prompt}}^{\text{FONLL}})^2 \cdot \frac{(\alpha \times \epsilon)_{\text{fd}}}{(\alpha \times \epsilon)_{\text{pr}}} \cdot$$
$$\frac{\frac{d\sigma_{\text{fd}}}{dp_T}}{\frac{d\sigma_{\text{pr}}}{dp_T}} \cdot \sqrt{\left(\frac{\Delta(\alpha \times \epsilon)_{\text{pr}}}{(\alpha \times \epsilon)_{\text{pr}}}\right)^2 + \left(\frac{\Delta(\alpha \times \epsilon)_{\text{fd}}}{(\alpha \times \epsilon)_{\text{fd}}}\right)^2}. \quad (40)$$

The statistical uncertainties due to the decay routine will only be considered for the EvtGen cross sections in the comparison of the results of the PYTHIA decayer with those of the EvtGen Package (see Sect. 9.3). They are given as

$$\Delta(f_{\text{prompt}}^{\text{data, stat.}}) = \frac{N_{\text{fd}}}{N_{\text{raw}}} \cdot \sqrt{\left(\frac{\Delta N_{\text{raw}}^{\text{stat}}}{N_{\text{raw}}}\right)^2 + \left(\frac{\Delta(\alpha \times \epsilon)_{\text{fd}}^{\text{stat}}}{(\alpha \times \epsilon)_{\text{fd}}}\right)^2 + \left(\frac{\Delta\left(\frac{d\sigma^{\text{EG}}}{dp_T}\right)}{\frac{d\sigma^{\text{EG}}}{dp_T}}\right)^2}, \quad (41)$$

$$\Delta(f_{\text{prompt}}^{\text{FONLL, stat.}}) = (f_{\text{prompt}}^{\text{FONLL}})^2 \cdot \frac{(\alpha \times \epsilon)_{\text{fd}}}{(\alpha \times \epsilon)_{\text{pr}}} \cdot$$
$$\frac{\frac{d\sigma_{\text{fd}}}{dp_T}}{\frac{d\sigma_{\text{pr}}}{dp_T}} \cdot \sqrt{\left(\frac{\Delta(\alpha \times \epsilon)_{\text{pr}}}{(\alpha \times \epsilon)_{\text{pr}}}\right)^2 + \left(\frac{\Delta(\alpha \times \epsilon)_{\text{fd}}}{(\alpha \times \epsilon)_{\text{fd}}}\right)^2 + \left(\frac{\Delta\left(\frac{d\sigma^{\text{EG}}}{dp_T}\right)}{\frac{d\sigma^{\text{EG}}}{dp_T}}\right)^2}, \quad (42)$$

with the statistical uncertainty $\Delta\frac{d\sigma^{\text{EG}}}{dp_T}$ of the EvtGen simulation.

9.2 Propagation of systematic uncertainties

The systematic uncertainties of $f_{\text{prompt}}^{\text{data}}$ are propagated quadratically but separately for the upper and lower error:

$$\Delta(f_{\text{prompt}}^{\text{data, syst.}})^{\pm} = \frac{N_{\text{fd}}}{N_{\text{raw}}} \cdot$$
$$\sqrt{\left(\frac{\Delta N_{\text{raw}}^{\text{syst}}}{N_{\text{raw}}}\right)^2 + \left(\frac{\Delta(\alpha \times \epsilon)_{\text{fd}}^{\text{syst}}}{(\alpha \times \epsilon)_{\text{fd}}}\right)^2 + \left(\frac{\Delta\left(\frac{d\sigma_{\text{fd}}}{dp_T}\right)^{\mp}}{\frac{d\sigma_{\text{fd}}}{dp_T}}\right)^2 + \left(\frac{\Delta\mathcal{L}_{\text{int}}}{\mathcal{L}_{\text{int}}}\right)^2 + \left(\frac{\Delta\mathcal{B}}{\mathcal{B}}\right)^2}. \quad (43)$$

The systematic uncertainty of $f_{\text{prompt}}^{\text{FONLL}}$ must be determined differently. The uncertainties of the feeddown and prompt predictions are partially correlated. So their total uncertainty bands must not be combined directly. The different contributions are split up by calculating $f_{\text{prompt}}^{\text{FONLL}}$ for all the variation of scales, the variation of

the charm mass, the variation of the bottom mass and the PDF uncertainty band. For the analysis with topological selection cuts the central value of $f_{\text{prompt}}^{\text{FONLL}}$ is also varied according to the systematic uncertainties of the acceptance times efficiencies. The following figures illustrate this procedure using the example of the analysis with topological cuts.

The prompt fraction is varied in a similar way to the FONLL calculations. Firstly the variation of scales is performed by choosing the same seven value sets as given in Eq. (19). Therefore only the feeddown and prompt cross sections corresponding to the same scale setting are combined to determine $f_{\text{prompt}}^{\text{FONLL}}$. This leads to seven different distributions of $f_{\text{prompt}}^{\text{FONLL}}$, depicted in Fig. 9.2. Then the envelope $f_{\text{max/min}}^{\text{FONLL}}$ of these seven histograms is chosen and the upper and lower uncertainty

$$\Delta f_{\text{sc}\pm}^{\text{FONLL}} = |f_{\text{max/min}}^{\text{FONLL}} - \left(f_{\text{prompt}}^{\text{FONLL}} \text{central value} \right)| \tag{44}$$

are derived consistently with the FONLL method (see Eq. (20)).
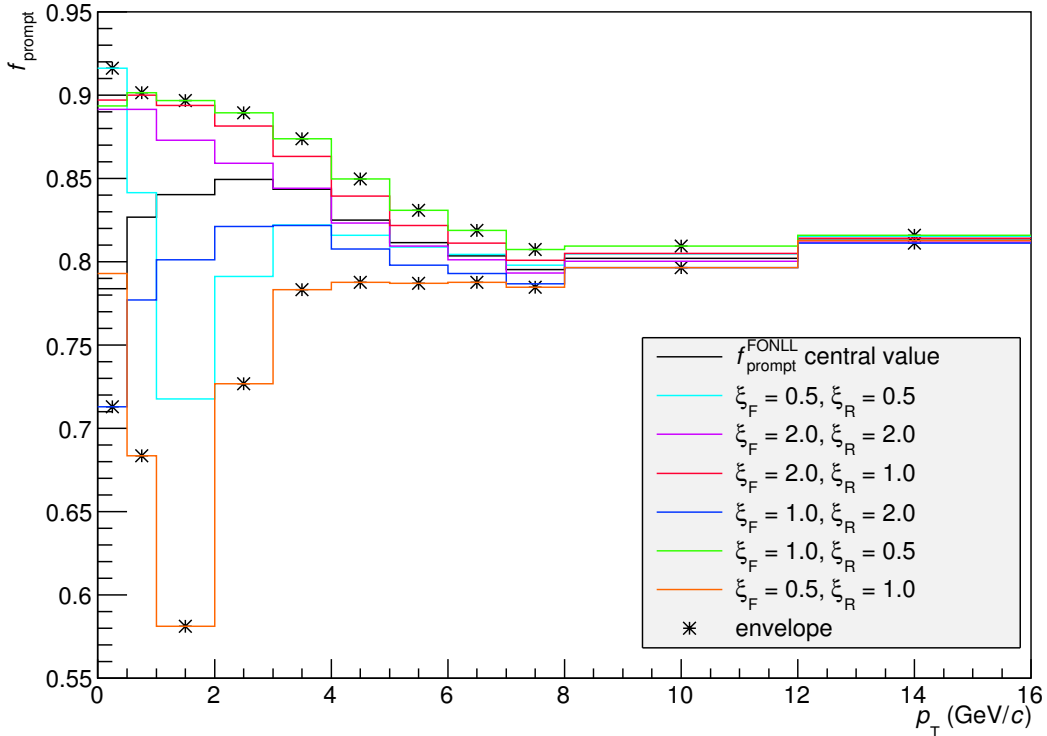

Figure 9.2: Variation of scales for the prompt fraction of the analysis with topological cuts.

Next, the variation of both the bottom and the charm mass is considered. The bottom mass is varied while keeping the charm mass at the central value and vice versa. For the bottom mass variation the corresponding predictions of the feeddown distribution are used to compute $f_{\mathrm{prompt}}^{\mathrm{FONLL}}$. The appropiate distributions are shown in Fig. 8.8 as the red uncertainty band of the variation of masses. For the charm mass variation the distributions of the uncertainty band of the variation of masses (shown in Fig. 8.9) are applied for the calculation of $f_{\mathrm{prompt}}^{\mathrm{FONLL}}$. Both variation of masses are contained in Fig. 9.3. From each of the two uncertainty bands, the upper and lower uncertainties are computed according to Eq. (21). So the upper and lower uncertainties due to the bottom mass variation are denoted as $\Delta f_{\mathrm{mb}\pm}^{\mathrm{FONLL}}$ and those due to the charm mass variation are denoted as $\Delta f_{\mathrm{mc}\pm}^{\mathrm{FONLL}}$.
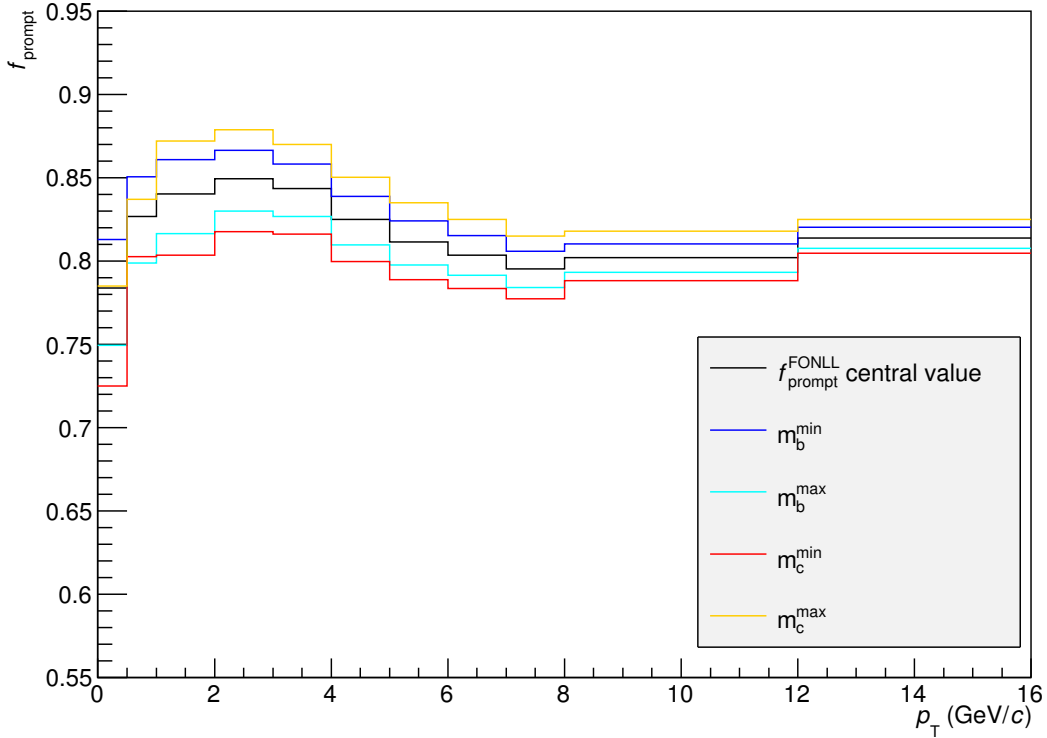
Figure 9.3: Variation of charm and bottom masses for the prompt fraction of the analysis with topological cuts.

The variation due to the uncertainties inherited from the PDFs is also studied. The parton distribution functions are the same for the calculation with bottom and charm quark yet they are evaluated at different points for the different quarks. Thus the uncertainties are correlated but the results of the evaluation for the different quarks

must be considered separately. Hence the prompt fraction is computed for the upper
and lower distribution of the PDF uncertainty band of the feeddown results shown
in Fig. 8.8, while keeping the prompt cross sections at their central predictions. The
central feeddown predictions are combined with the upper and lower distribution of
the PDF uncertainty band of the prompt results. These variations of the prompt
fraction are shown in Fig. 9.4. The envelope of the resulting distributions of the
prompt fraction is determined. It is marked with small stars at the bin centers in
Fig. 9.4. The upper and lower uncertainty $\Delta f_{\mathrm{PDF}\pm}^{\mathrm{FONLL}}$ are derived from the envelope,
as was done for the variation of scales.
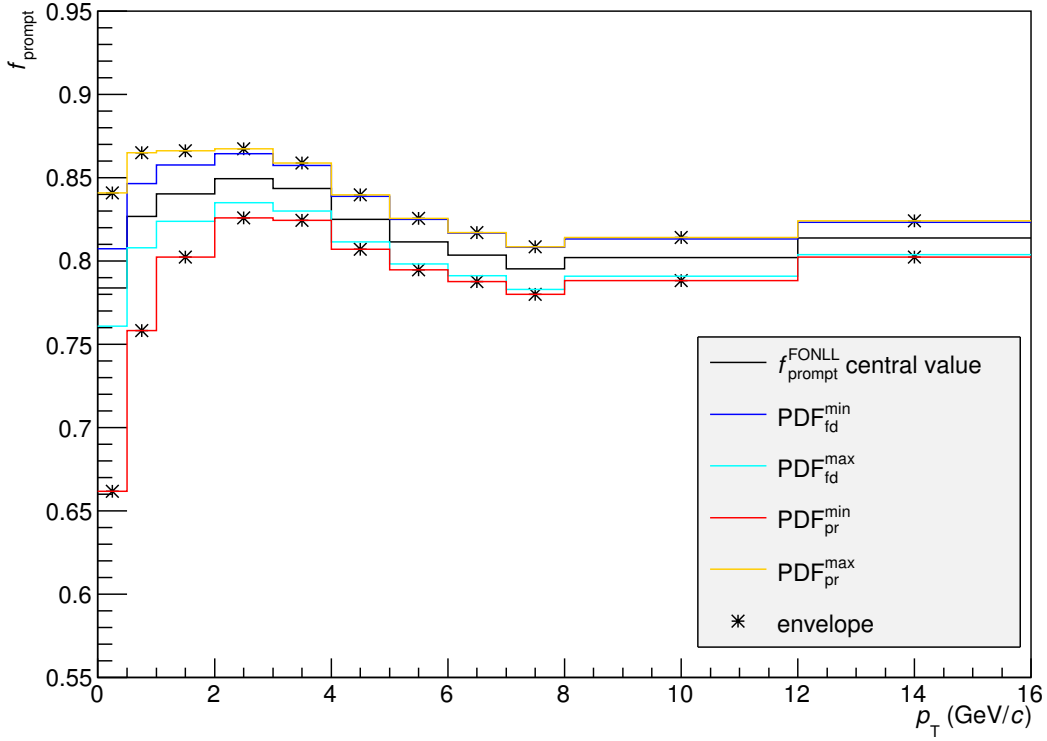
Figure 9.4: Variation of the prompt fraction of the analysis with topological cuts
due to the uncertainties of the PDFs.

For the topological analysis the systematic uncertainties of the acceptances times
efficiencies are also included. The relative systematic error of the acceptances times
efficiencies are the same, as they are derived from the relative errors of the tracking
and cut efficiencies. Hence they are considered to be correlated and are not combined
quadratically. The prompt fraction is determined for the upper $(\alpha \times \epsilon)_{\mathrm{fd}}^{\mathrm{max}}$ and lower
$(\alpha \times \epsilon)_{\mathrm{fd}}^{\mathrm{min}}$ border of the systematic uncertainty band of the feeddown acceptance

times efficiencies, while all the other values are kept to their central settings. The prompt fraction is computed with the upper $(\alpha \times \epsilon)_{\text{pr}}^{\text{max}}$ and lower $(\alpha \times \epsilon)_{\text{pr}}^{\text{min}}$ border of the systematic uncertainty band of the prompt acceptance times efficiencies. The results are shown in Fig. 9.5 and again the envelope is taken although the difference between the variation of prompt and feeddown contributions is rather marginal. The upper and lower error $\Delta f_{\alpha \times \epsilon \pm}^{\text{FONLL}}$ are deduced as before from the envelope.
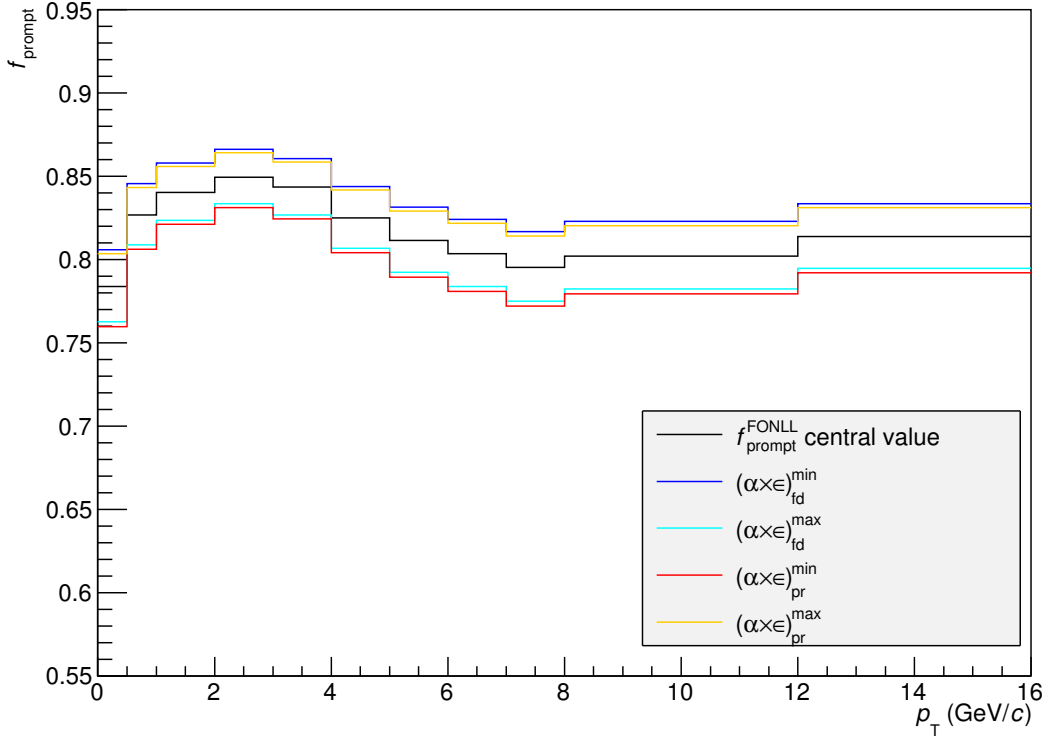
Figure 9.5: Variation of the prompt fraction due to the systematic uncertainties of the $\alpha \times \epsilon$.

Finally the resulting uncertainties are combined in the same way as done for the FONLL approach. The total systematic uncertainties are

$$\Delta \left(f_{\text{prompt}}^{\text{FONLL, syst.}} \right)^{\pm} =$$
$$\sqrt{\left(\Delta f_{\text{sc}\pm}^{\text{FONLL}} \right)^2 + \left(\Delta f_{\text{mb}\pm}^{\text{FONLL}} \right)^2 + \left(\Delta f_{\text{mc}\pm}^{\text{FONLL}} \right)^2 + \left(\Delta f_{\text{PDF}\pm}^{\text{FONLL}} \right)^2 + \left(\Delta f_{\alpha \times \epsilon \pm}^{\text{FONLL}} \right)^2}. \quad (45)$$

The determination of the systematic uncertainties for the prompt fraction in the analysis without topological cuts is performed equivalently only differing by the canceling out of the $\alpha \times \epsilon$ terms.

9.3 Comparison of the prompt fraction derived from the feeddown with PYTHIA and EvtGen

Before the results of this thesis are presented the influence of the choice of the external decayer is examined. For this purpose, the systematic uncertainties are omitted and only the statistical uncertainties are shown. The comparison is performed for the prompt fraction given in Eq. (35) and (37) with the associated statistical uncertainties from Eq. (41) and (42). The comparison is limited to the analysis with topological selection. The different prompt fractions are depicted in Fig. 9.6.
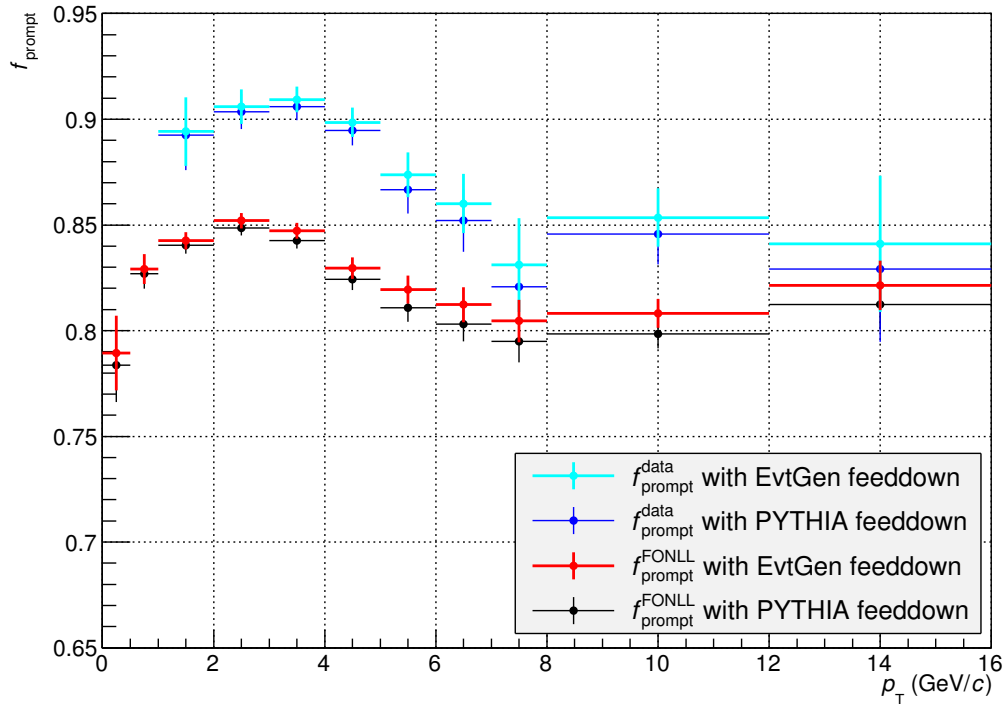
Figure 9.6: The prompt fraction determined with the PYTHIA decayer results are compared to those of the EvtGen package.

The results of both external decayers are consistent within their statistical uncertainties. Nevertheless the prompt fractions show a deviation over the whole p_T range. The results produced with the EvtGen simulation are slightly higher than those produced with PYTHIA. Considering the large systematic uncertainties, this offset is negligible as was stated in [1]. Still, this observation should be kept in mind for the later comparison between the results of this thesis and the published results.

10 Results

10.1 Results of the prompt fraction in the analysis with topological cuts

The prompt fraction computed with the data-based method according to Eq. (35) is shown in Fig. 10.1. The prompt fraction corresponding to the FONLL-based method of Eq. (37) is depicted in Fig. 10.2. The values of the prompt fractions are given in Tab. 10.1

The systematic uncertainties exceed the statistical uncertainties in both distributions. The statistical uncertainties in Fig. 10.1 are dominated by those of the experimental data, while in Fig. 10.2 only the statistical uncertainty of the acceptances times efficiencies is considered. The prompt fraction derived from only the FONLL pQCD predictions lies below the data results. This effect was also observed in [1].

p_{T} range (GeV/c)	$f_{\mathrm{prompt}}^{\mathrm{FONLL}} \pm$ stat. $\pm$ syst.	$f_{\mathrm{prompt}}^{\mathrm{data}} \pm$ stat. $\pm$ syst.
0.0–0.5	$0.784 \pm 0.018 \; {}^{+0.149}_{-0.158}$	
0.5–1.0	$0.827 \pm 0.007 \; {}^{+0.090}_{-0.164}$	
1.0–2.0	$0.840 \pm 0.004 \; {}^{+0.075}_{-0.226}$	$0.893 \pm 0.016 \; {}^{+0.055}_{-0.059}$
2.0–3.0	$0.850 \pm 0.004 \; {}^{+0.058}_{-0.132}$	$0.904 \pm 0.008 \; {}^{+0.041}_{-0.048}$
3.0–4.0	$0.843 \pm 0.004 \; {}^{+0.049}_{-0.073}$	$0.906 \pm 0.006 \; {}^{+0.036}_{-0.044}$
4.0–5.0	$0.825 \pm 0.005 \; {}^{+0.045}_{-0.055}$	$0.895 \pm 0.007 \; {}^{+0.037}_{-0.047}$
5.0–6.0	$0.811 \pm 0.007 \; {}^{+0.041}_{-0.045}$	$0.867 \pm 0.011 \; {}^{+0.043}_{-0.058}$
6.0–7.0	$0.804 \pm 0.008 \; {}^{+0.038}_{-0.040}$	$0.852 \pm 0.015 \; {}^{+0.046}_{-0.061}$
7.0–8.0	$0.795 \pm 0.010 \; {}^{+0.036}_{-0.037}$	$0.821 \pm 0.023 \; {}^{+0.055}_{-0.072}$
8.0–12.0	$0.802 \pm 0.007 \; {}^{+0.031}_{-0.032}$	$0.846 \pm 0.014 \; {}^{+0.045}_{-0.058}$
12.0–16.0	$0.814 \pm 0.012 \; {}^{+0.026}_{-0.027}$	$0.830 \pm 0.034 \; {}^{+0.047}_{-0.057}$

Table 10.1: Values of the prompt fractions $f_{\mathrm{prompt}}^{\mathrm{data}}$ due to Eq. (35), and $f_{\mathrm{prompt}}^{\mathrm{FONLL}}$ due to Eq. (37) for the analysis with topological selection cuts.
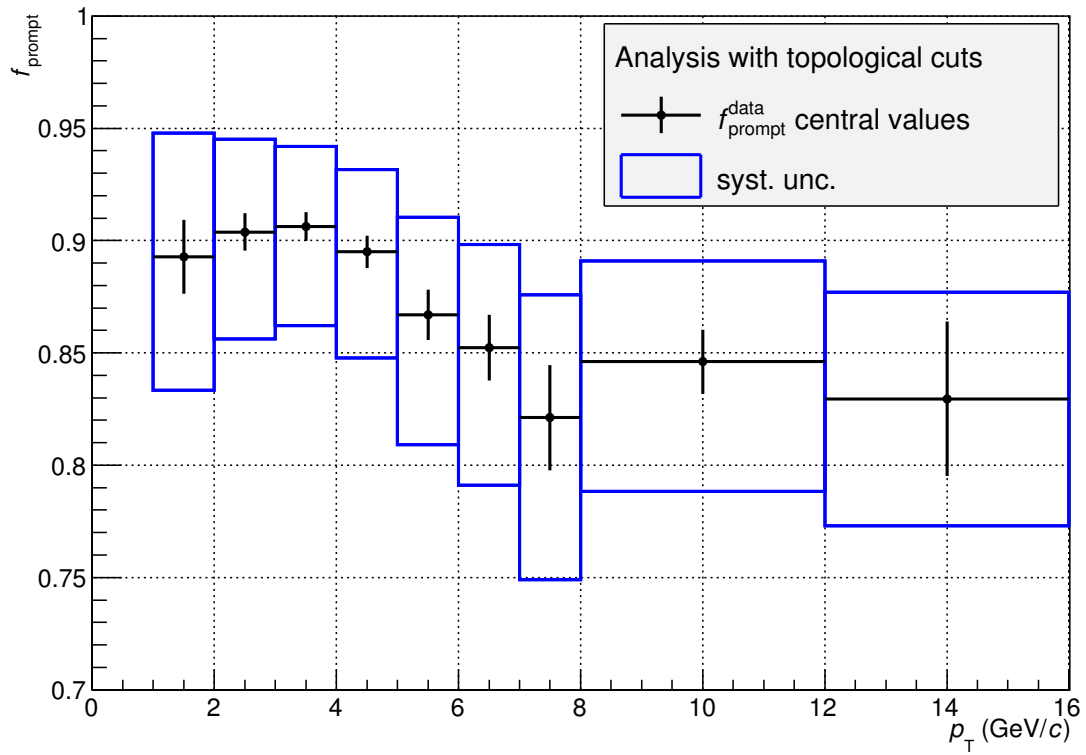
Figure 10.1: The prompt fraction $f_{\text{prompt}}^{\text{data}}$ due to Eq. (35) in the analysis based on real data with topological selection cuts. The prompt fraction ranges between 0.82 and 0.91.
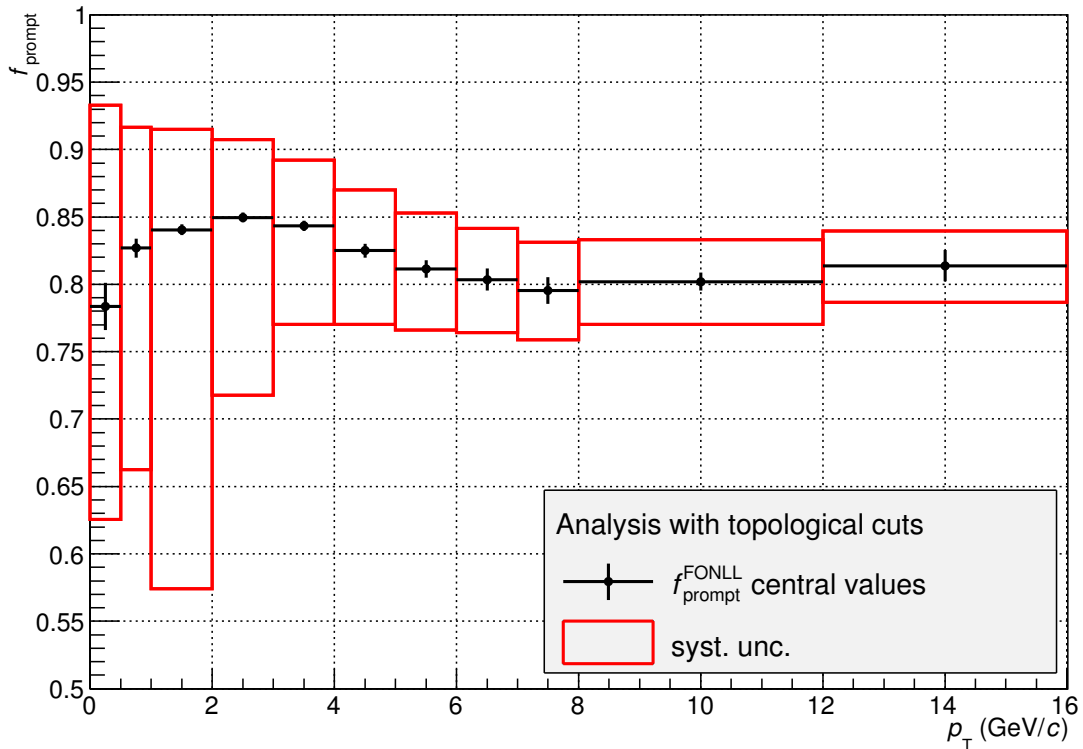
Figure 10.2: The prompt fraction $f_{\mathrm{prompt}}^{\mathrm{FONLL}}$ due to Eq. (37) in the FONLL-based analysis with topological selection cuts. The prompt fraction ranges between 0.78 and 0.85.

10.1.1 Combined results

The prompt fraction of the measured raw yield of D^0 mesons is determined by means of the FONLL pQCD predictions and the feeddown simulation. To account for the total uncertainties that come along with the theoretical predictions the envelope of the uncertainties of both calculation methods for the prompt fraction is chosen. The central values and statistical uncertainties of $f_{\mathrm{prompt}}^{\mathrm{data}}$ combined with this envelope represent the prompt fraction f_{prompt}. It is applied in data analyses to compute the cross sections from the measured raw yields in [1].

Both central predictions with their statistical uncertainties are included in Fig. 10.3. There the systematic deviation of $f_{\mathrm{prompt}}^{\mathrm{FONLL}}$ can be seen. The results for f_{prompt} with the associated uncertainties is depicted in blue and the corresponding values are listed as $f_{\mathrm{prompt}}^{\mathrm{this\ thesis}}$ in Tab. 11.1.
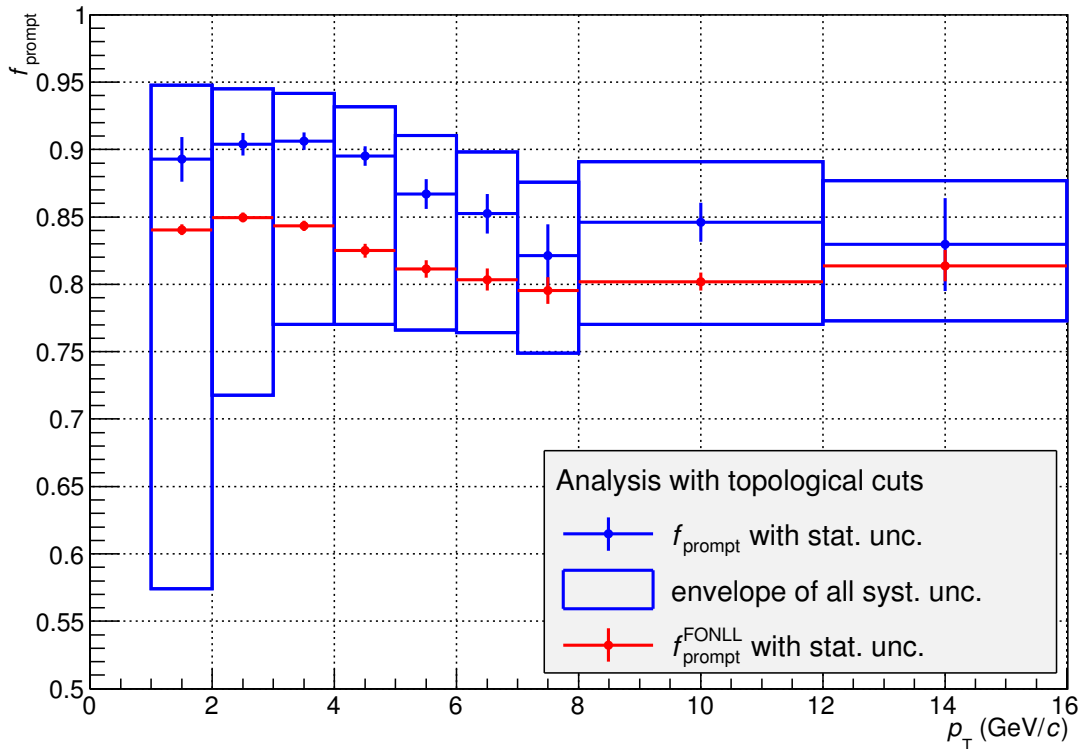
Figure 10.3: Combined results of the prompt fraction f_{prompt} of the analysis using topological selection cuts. The central values and statistical uncertainties of f_{prompt} are directly derived from $f_{\mathrm{prompt}}^{\mathrm{data}}$. The systematic uncertainties of f_{prompt} are the envelope of the systematic uncertainties of $f_{\mathrm{prompt}}^{\mathrm{data}}$ and $f_{\mathrm{prompt}}^{\mathrm{FONLL}}$. The FONLL-based prompt fraction $f_{\mathrm{prompt}}^{\mathrm{FONLL}}$ is depicted to show the systematic offset compared to the data-based prompt fraction.

10.2 Results of the analysis without topological cuts

The prompt fraction computed with the data-based method according to Eq. (35) is shown in Fig. 10.4. The prompt fraction corresponding to the FONLL-based method of Eq. (37) is depicted in Fig. 10.5. The values of the prompt fractions are given in Tab. 10.2.

For the results of the data-based method using Eq. (35) the systematic uncertainties are larger than the statistical uncertainties. The statistical uncertainties are given by those of the efficiency correction $\alpha \times \epsilon$ only. For the FONLL-based method using Eq. (37) the statistical uncertainties are completely neglected.

p_T range (GeV/c)	$f_{\text{prompt}}^{\text{FONLL}} \pm$ syst.	$f_{\text{prompt}}^{\text{data}} \pm$ stat. $\pm$ syst.
0.0–1.0	$0.929 \, ^{+0.041}_{-0.057}$	$0.958 \pm 0.013 \, ^{+0.021}_{-0.022}$
1.0–2.0	$0.935 \, ^{+0.032}_{-0.146}$	$0.957 \pm 0.009 \, ^{+0.021}_{-0.023}$
2.0–3.0	$0.928 \, ^{+0.028}_{-0.073}$	$0.949 \pm 0.010 \, ^{+0.021}_{-0.025}$
3.0–4.0	$0.917 \, ^{+0.026}_{-0.042}$	$0.949 \pm 0.008 \, ^{+0.020}_{-0.025}$
4.0–5.0	$0.907 \, ^{+0.024}_{-0.030}$	$0.921 \pm 0.017 \, ^{+0.028}_{-0.036}$
5.0–6.0	$0.898 \, ^{+0.021}_{-0.024}$	$0.932 \pm 0.012 \, ^{+0.023}_{-0.030}$
6.0–7.0	$0.891 \, ^{+0.019}_{-0.020}$	$0.915 \pm 0.019 \, ^{+0.030}_{-0.038}$
7.0–8.0	$0.885 \, ^{+0.018}_{-0.018}$	$0.917 \pm 0.020 \, ^{+0.028}_{-0.036}$
8.0–12.0	$0.875 \, ^{+0.016}_{-0.015}$	$0.873 \pm 0.029 \, ^{+0.041}_{-0.051}$
12.0–16.0	$0.858 \, ^{+0.013}_{-0.013}$	$0.908 \pm 0.025 \, ^{+0.033}_{-0.037}$

Table 10.2: Values of the prompt fractions $f_{\text{prompt}}^{\text{data}}$ due to Eq. (35), and $f_{\text{prompt}}^{\text{FONLL}}$ due to Eq. (37) for the analysis without topological cuts.
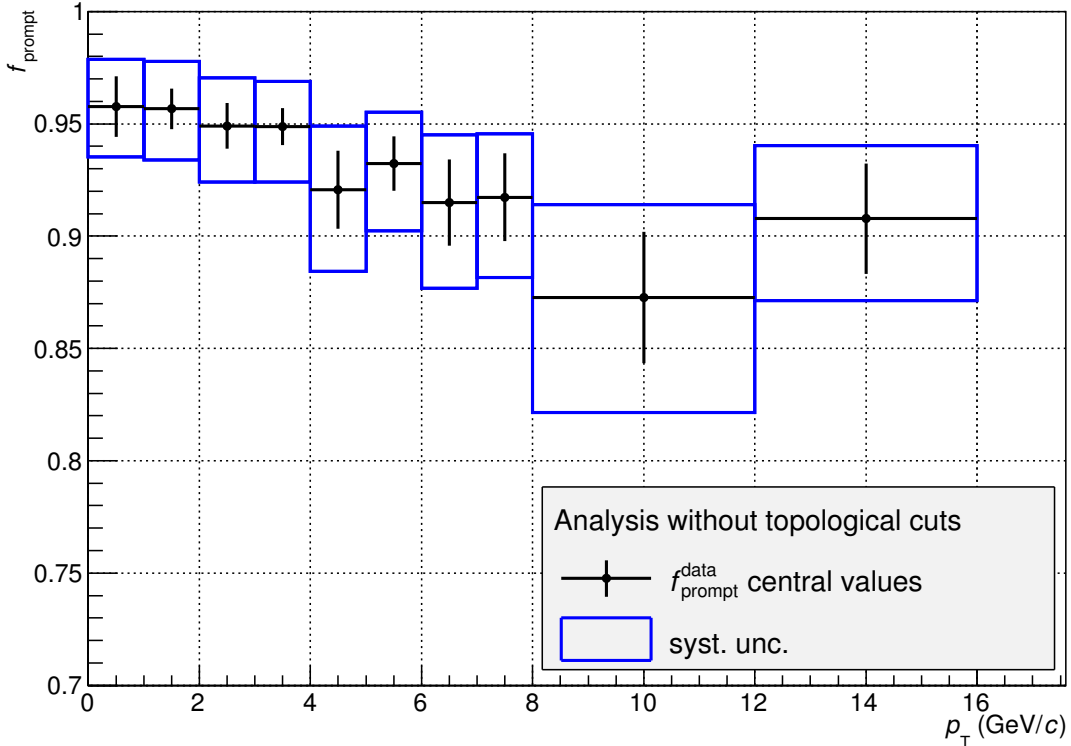
Figure 10.4: Prompt fraction $f_{\text{prompt}}^{\text{data}}$ based on real data (see Eq. (35)) in the analysis without topological selection cuts ranging between 0.87 and 0.96.
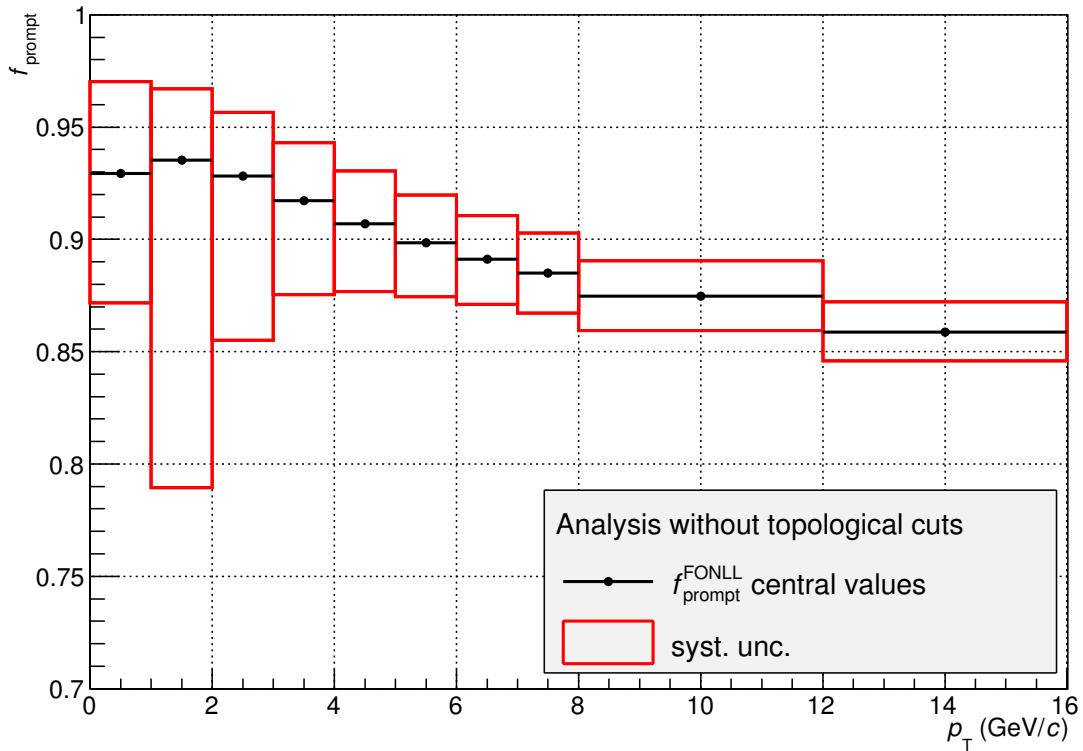
Figure 10.5: The FONLL-based prompt fraction $f_{\text{prompt}}^{\text{FONLL}}$ from Eq. (37) in the analysis without topological selection. The prompt fraction varies between 0.86 and 0.94.

10.2.1 Combined results

The results are combined as before. Again the central values and statistical uncertainties of $f_{\text{prompt}}^{\text{data}}$ together with the envelope of the systematic uncertainties of both methods represent the prompt fraction f_{prompt}. The corresponding values are listed as $f_{\text{prompt}}^{\text{this thesis}}$ in Tab. 11.2.

The central predictions for both f_{prompt} and $f_{\text{prompt}}^{\text{FONLL}}$ are depicted in Fig. 10.6 together with the envelope representing the total systematic uncertainty of f_{prompt}. The central values of $f_{\text{prompt}}^{\text{data}}$ are larger than the FONLL predictions except for the bin at 8–12 GeV.
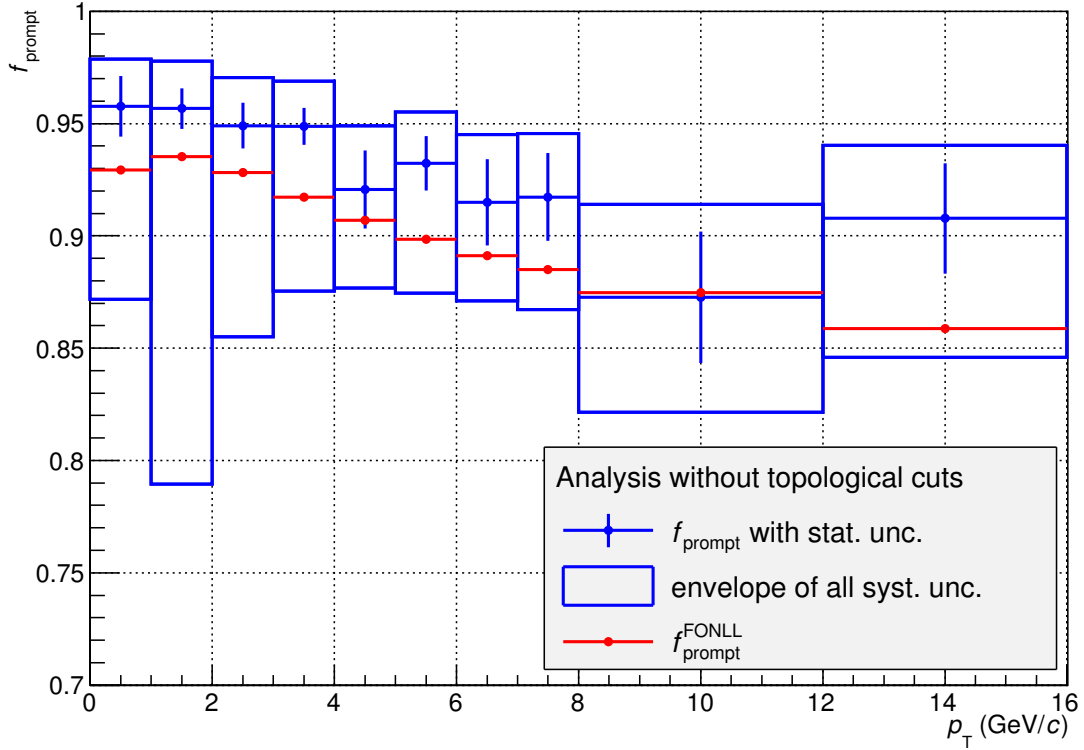
Figure 10.6: Combined results of the prompt fraction f_{prompt} of the analysis without topological selection cuts. The central values and statistical uncertainties of f_{prompt} are directly derived from the data-based method $f_{\mathrm{prompt}}^{\mathrm{data}}$. The systematic uncertainties of f_{prompt} are the envelope of the systematic uncertainties of $f_{\mathrm{prompt}}^{\mathrm{data}}$ and $f_{\mathrm{prompt}}^{\mathrm{FONLL}}$. The FONLL-based prompt fraction $f_{\mathrm{prompt}}^{\mathrm{FONLL}}$ is depicted to show the systematic offset compared to the data-based prompt fraction.

11 Discussion

11.1 Reproduction of the published prompt fraction

As in [1] no values of the result of the prompt fraction and the associated uncertainties are given, they had to be reproduced. The systematic uncertainties of $f_{\text{prompt}}^{\text{FONLL}}$ were propagated in [1] without consideration of the correlations between the particular uncertainty sources due to the theoretical predictions. To propagate the systematic uncertainties of $f_{\text{prompt}}^{\text{FONLL}}$ according to the published prompt fraction, they are defined as

$$\Delta \left(f_{\text{prompt}}^{\text{FONLL, repr., syst.}} \right)^{\pm} = \sqrt{\left(\Delta f_{\text{total}\pm}^{\text{FONLL}} \right)^2 + \left(\Delta f_{\alpha \times \epsilon \pm}^{\text{FONLL}} \right)^2}, \qquad (46)$$

where $\Delta f_{\text{total}\pm}^{\text{FONLL}}$ is derived from the total uncertainty band of the FONLL D^0 feeddown and prompt predictions. For this purpose the prompt and feeddown distributions corresponding to the lower uncertainties are combined to determine the prompt fraction. The same procedure is applied to the upper uncertainties. The difference between the central prompt fraction and the prompt fraction corresponding to the lower FONLL contributions yields $\Delta f_{\text{total}+}^{\text{FONLL}}$ and the difference between the central prompt fraction and the prompt fraction corresponding to the upper FONLL contributions yields $\Delta f_{\text{total}-}^{\text{FONLL}}$.

For a consistency check with the published prompt fraction, the reproduced results are depicted in Fig. 11.1 next to the published results from [1] (see Fig. 11.2). The corresponding values are listed as $f_{\text{prompt}}^{\text{repr. pub.}}$ in Tab. 11.1 and serve as reference values for the comparison between the results of this thesis and the results published in [1].

The results for the prompt fraction given in the publication [1] are depicted in Fig. 11.2. The solid red line corresponds to the data-based method to determine $f_{\text{prompt}}^{\text{data}}$ of this thesis and the dashed red line corresponds to the FONLL-based method to determine $f_{\text{prompt}}^{\text{FONLL}}$ of this thesis. The red boxes show the envelope of the systematic uncertainties of both methods. In contrast to the results of this thesis, the systematic uncertainties were determined without considering the correlations of the systematic uncertainties due to the FONLL predictions of $f_{\text{prompt}}^{\text{FONLL}}$. The black markers in Fig. 11.2 show an impact parameter fit which was only done in [1]. An attempt was made
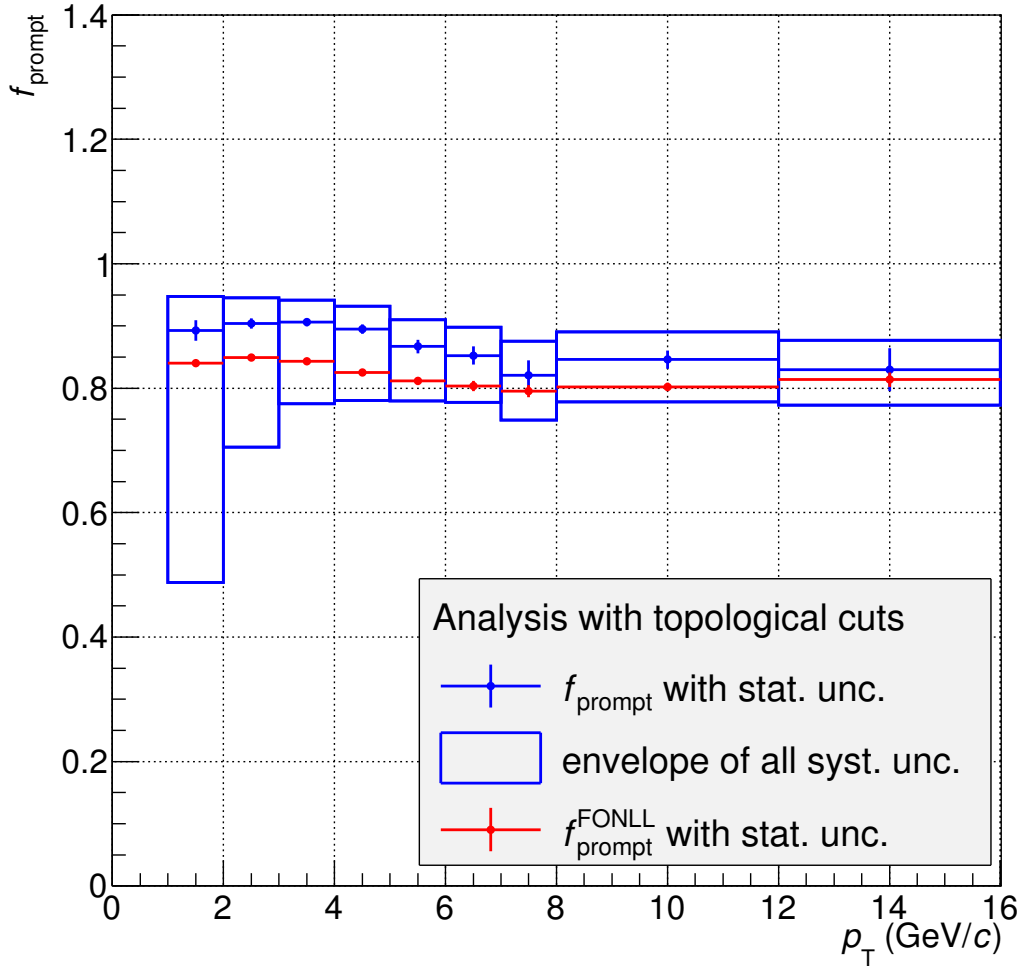
Figure 11.1: Reproduction of the published results [1] with the systematic uncertainties propagated similar to those of this thesis, only differing by the propagation of the systematic uncertainties due to the FONLL predictions of $f_{\mathrm{prompt}}^{\mathrm{FONLL}}$. For a consistency check with the published results see Fig. 11.2.
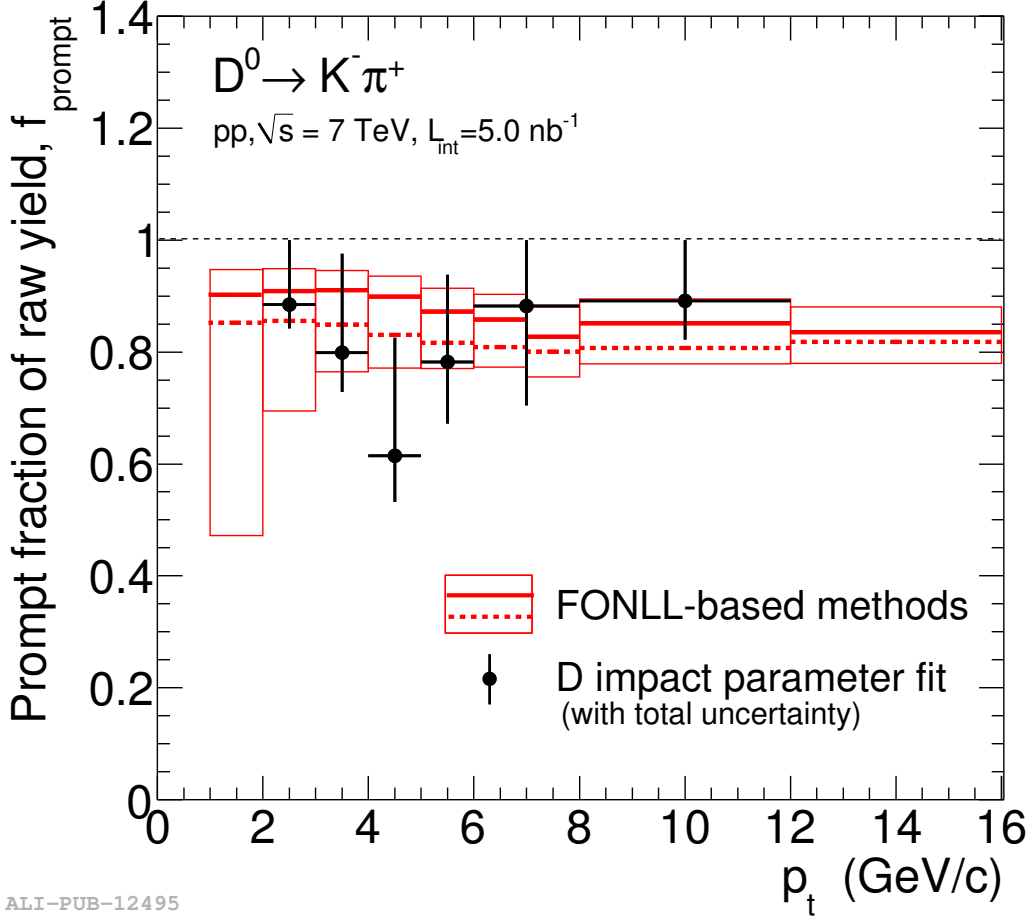
Figure 11.2: Results of the prompt fraction published in and taken from [1]. The solid red line corresponds to the data-based $f_{\text{prompt}}^{\text{data}}$ method given in Eq. (35) of this thesis and the dashed red line corresponds to the FONLL-based $f_{\text{prompt}}^{\text{FONLL}}$ method given in Eq. (37) of this thesis. The red boxes show the envelope of the systematic uncertainties of both methods, but without consideration of the correlations of the systematic uncertainties due to the theoretical FONLL predictions. The black markers show an alternative method to estimate the prompt fraction based on an impact parameter fit. The vertical lines include both statistical and systemtatic uncertainties. This method was used in [1] to check the FONLL-based result.

to determine the prompt fraction of the D^0 mesons experimentally using the impact parameter fit. The prompt D^0 mesons have smaller impact parameters than the feeddown D^0 mesons and the distributions of the impact parameter show different shapes for prompt and feeddown D^0 mesons. This is the basis to distinguish between the data from prompt and feeddown D^0 mesons by applying different impact parameter fit methods to the prompt and feeddown distributions. As can be seen in Fig. 11.2, the impact parameter fit method is affected with large uncertainties. Thus, in [1] it serves only as data-driven check for the FONLL-based methods.

The central values of the prompt fraction of the data applying topological selection cuts in this thesis differ from the published ones by about 1%. This was estimated from the plots shown in Fig. 11.1 and 11.2. The reproduced prompt fraction is slightly smaller than the published results. This systematic deviation is due to the application of different decayers for the feeddown simulation. In this thesis PYTHIA performs the decay routine, while in [1] the EvtGen package was used to simulate the feeddown routine. The comparison between the central values of the prompt fraction for both decayers can be seen in Fig. 9.6. Furthermore there is no information in [1] about the applied fragmentation fraction for the charm quark. It might be slightly different from that used in this thesis and therefore yield also a contribution to systematic deviations that can not be estimated. The branching ratio $\mathcal{B}(D^0 \to K^-\pi^+)$ in this thesis is chosen according to the recently published data [3], while in [1] the branching ratio is set to $3.87 \pm 0.05\%$ [41]. Not only the central values of this thesis differ from the published ones but also the uncertainties of the reproduced results differ slightly from the published uncertainties. The systematic uncertainties assumed for the acceptances times efficiencies in this thesis might differ from the ones applied in the publication, as only information for the lowest and the highest p_T interval was provided. Nevertheless, the resulting deviations are rather small.

In conclusion it can be assumed that the reproduced prompt fraction and the corresponding systematic uncertainties are consistent with the published ones. In the following only the reproduced prompt fraction $f_{\text{prompt}}^{\text{repr. pub.}}$ will be used for comparison with the results of this thesis.

11.2 Analysis with topological selection cuts

One of the principal motivations for this thesis was to propagate the uncertainties due to the FONLL predictions considering the correlations between the particular sources of systematic uncertainty. Therefore, it is sufficient to compare the results of this thesis $f_{\text{prompt}}^{\text{this thesis.}}$ to the reproduced results $f_{\text{prompt}}^{\text{repr. pub.}}$ of [1], although their central values and statistical uncertainties are identical. A comparison with the true prompt fraction of [1] would show a small deviation from the reproduced results due to the different decayer, branching ratio and fragmentation fractions. However, this should not significantly affect the results of the relative systematic uncertainties.

The results for the topological analysis of this thesis are depicted together with the reproduced results of [1] in Fig. 11.3. The corresponding values are listed in Tab. 11.1.
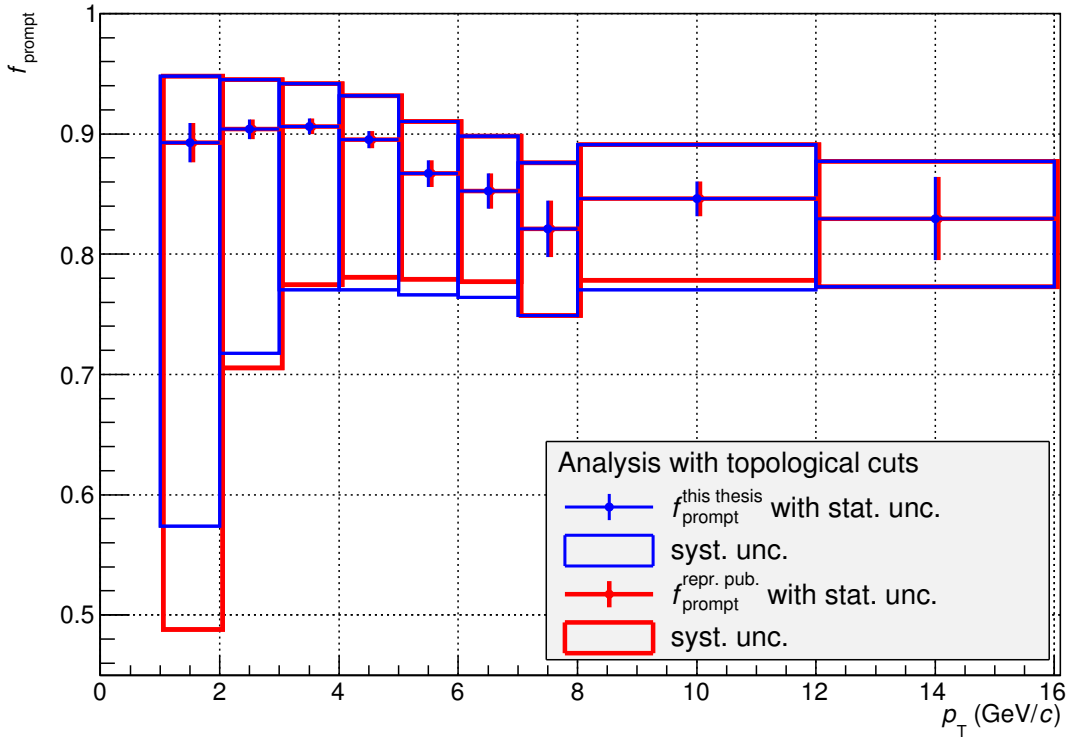

Figure 11.3: Prompt fraction determined in this thesis $f_{\text{prompt}}^{\text{this thesis.}}$ compared to the reproduced results of [1] $f_{\text{prompt}}^{\text{repr. pub.}}$, which are slightly shifted to the right for better visibility. The central values and statistical uncertainties are the same for both results, as they only differ in the propagation of the systematic uncertainties.

p_T range (GeV/c)	$f_\mathrm{prompt}^{\text{this thesis}} \pm$ stat. $\pm$ syst.	$f_\mathrm{prompt}^{\text{repr. pub.}} \pm$ stat. $\pm$ syst.
1.0–2.0	$0.893 \pm 0.016 \; ^{+0.055}_{-0.319}$	$0.893 \pm 0.016 \; ^{+0.055}_{-0.405}$
2.0–3.0	$0.904 \pm 0.008 \; ^{+0.041}_{-0.186}$	$0.904 \pm 0.008 \; ^{+0.041}_{-0.198}$
3.0–4.0	$0.906 \pm 0.006 \; ^{+0.036}_{-0.136}$	$0.906 \pm 0.006 \; ^{+0.036}_{-0.132}$
4.0–5.0	$0.895 \pm 0.007 \; ^{+0.037}_{-0.125}$	$0.895 \pm 0.007 \; ^{+0.037}_{-0.114}$
5.0–6.0	$0.867 \pm 0.011 \; ^{+0.043}_{-0.101}$	$0.867 \pm 0.011 \; ^{+0.043}_{-0.088}$
6.0–7.0	$0.852 \pm 0.015 \; ^{+0.046}_{-0.088}$	$0.852 \pm 0.015 \; ^{+0.046}_{-0.075}$
7.0–8.0	$0.821 \pm 0.023 \; ^{+0.055}_{-0.072}$	$0.821 \pm 0.023 \; ^{+0.055}_{-0.072}$
8.0–12.0	$0.846 \pm 0.014 \; ^{+0.045}_{-0.076}$	$0.846 \pm 0.014 \; ^{+0.045}_{-0.068}$
12.0–16.0	$0.830 \pm 0.034 \; ^{+0.047}_{-0.057}$	$0.830 \pm 0.034 \; ^{+0.047}_{-0.057}$

Table 11.1: Values of the combined results of the prompt fraction from this thesis $f_\mathrm{prompt}^{\text{this thesis}}$ and from the reproduced published results $f_\mathrm{prompt}^{\text{repr. pub.}}$ with the associated total uncertainties for the analysis with topological selection.

The consideration of correlations between the systematic uncertainties due to the theoretical predictions, as done in this thesis, leads to a significant reduction of the lower systematic uncertainties in the low p_T range. The first p_T interval of the reproduced results of [1] has a lower relative systematic uncertainty of 45%, whereas in this thesis it is reduced to 36%. The lower relative systematic uncertainties of the other p_T intervals show only slight differences. They decrease from about 21–22% at the second p_T interval to 7% at the last p_T interval. The lower systematic uncertainty of the second bin is slightly reduced in this thesis, while the lower systematic uncertainties of the bins in the range between 3–7 GeV/c and 8–12 GeV/c slightly increase. The remaining bins are dominated by the systematic uncertainties of $f_\mathrm{prompt}^{\text{data}}$, which are the same for both this thesis and the reproduced results. The contributions of the systematic uncertainties of the data-based method $f_\mathrm{prompt}^{\text{data}}$ also determine the upper systematic uncertainties of the final results. Accordingly the upper systematic uncertainties are the same for both methods of uncertainty propagation.

11.3 Analysis without topological selection cuts

The prompt fraction for the analysis without topological selection cuts was determined by Christian Möhler in [2]. There, the feeddown contributions are directly computed with the FONLL form [42]. Only the data-based method to calculate the prompt fraction $f_{\mathrm{prompt}}^{\mathrm{data}}$, taking into account the feeddown distributions predicted directly by FONLL, provides a basis for the determination of the prompt fraction $f_{\mathrm{prompt}}^{\mathrm{CM}}$. The statistical uncertainties are neglected and the systematic uncertainties are symmetric.

In this thesis the feeddown distribution was not directly computed with the FONLL form but with a decay simulation as described above. To account for the whole uncertainties of the FONLL predictions one must consider the contributions of $f_{\mathrm{prompt}}^{\mathrm{FONLL}}$ irrespectively of the feeddown performance. This was done in this thesis and the prompt fraction $f_{\mathrm{prompt}}^{\mathrm{this\ thesis}}$ is depicted together with the results of [2] in Fig. 11.4 and the corresponding values are listed in Tab. 11.2.

The results of the central values of the prompt fraction of this thesis are marginally smaller than those of [2]. These deviations are all less than 1%. The branching ratio used in this thesis $\mathcal{B}(\mathrm{D}^0 \to \mathrm{K}^-\pi^+) = 3.93 \pm 0.4\%$ [3] is about 1% larger than that used in [2] ($\mathcal{B} = 3.88 \pm 0.5\%$ [43]). In this thesis the small contribution of $\approx 0.01\%$ of the doubly Cabibbo-suppressed decay $\mathrm{D}^0 \to \mathrm{K}^+\pi^-$ is neglected, in [2] it is included. Another difference is that in [2] the feeddown distributions are directly taken from the FONLL form. All differences can account for the marginal deviations. Considering the large systematic uncertainties, the deviations of the central values of the prompt fraction are negligible. In addition, the deviations are all within the statistical uncertainties.

The relative upper systematic uncertainties are approximately the same in this thesis and in [2]. They range between 2 and 5%. The major differences are the lower uncertainty ranges. As this thesis provides combined results of the envelope of the data-based $f_{\mathrm{prompt}}^{\mathrm{data}}$ and only FONLL-based $f_{\mathrm{prompt}}^{\mathrm{FONLL}}$ method, the lower uncertainties are considerably larger than those given in [2]. They reach about 17% for the second p_{T} bin, while they range between 8 and 10% for the first, the third and the fourth p_{T} bin. At $p_{\mathrm{T}} > 4$ GeV/c the relative lower systematic uncertainties of this thesis are about 5–7%.
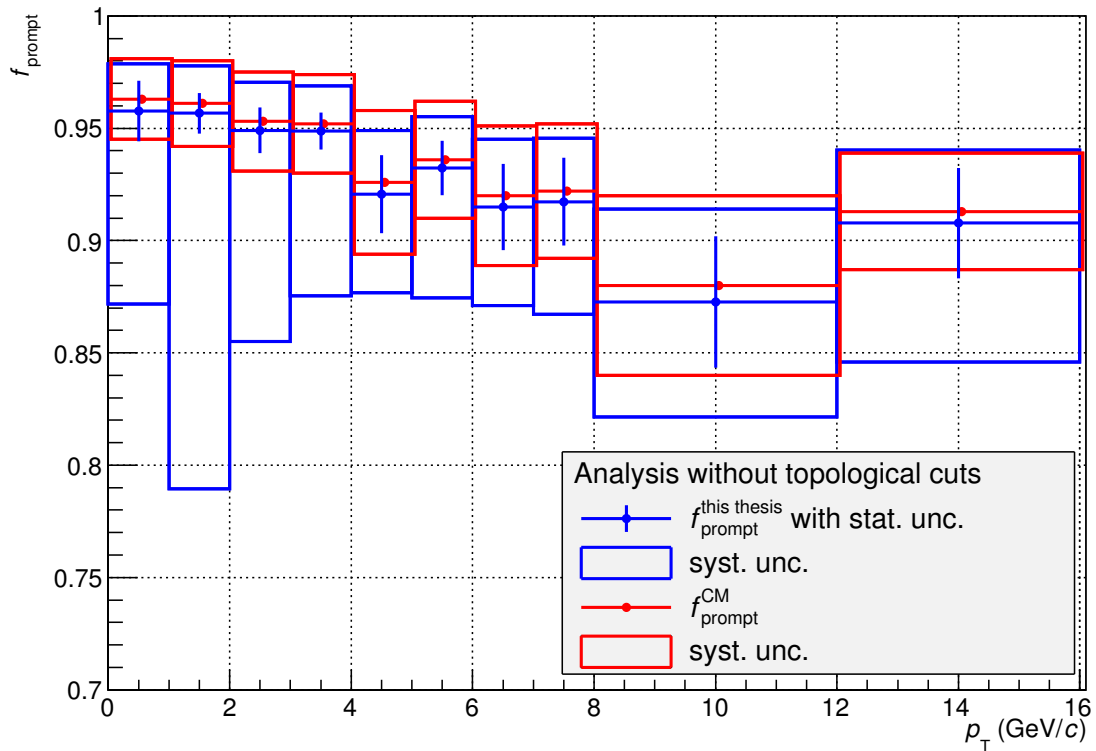
Figure 11.4: Prompt fractions determined in this thesis $f_{\mathrm{prompt}}^{\mathrm{this\ thesis}}$ and in [2] $f_{\mathrm{prompt}}^{\mathrm{CM}}$ for the non-topological analysis. The bin centers of $f_{\mathrm{prompt}}^{\mathrm{CM}}$ are slightly shifted to the right for better visibility.

p_T range (GeV/c)	$f_{\text{prompt}}^{\text{this thesis}} \pm$ stat. $\pm$ syst.	$f_{\text{prompt}}^{\text{CM}} \pm$ syst.
0.0–1.0	$0.958 \pm 0.013 \; {}^{+0.021}_{-0.086}$	0.963 ± 0.018
1.0–2.0	$0.957 \pm 0.009 \; {}^{+0.021}_{-0.167}$	0.961 ± 0.019
2.0–3.0	$0.949 \pm 0.010 \; {}^{+0.021}_{-0.094}$	0.953 ± 0.022
3.0–4.0	$0.949 \pm 0.008 \; {}^{+0.020}_{-0.073}$	0.952 ± 0.022
4.0–5.0	$0.921 \pm 0.017 \; {}^{+0.028}_{-0.044}$	0.926 ± 0.032
5.0–6.0	$0.932 \pm 0.012 \; {}^{+0.023}_{-0.058}$	0.936 ± 0.026
6.0–7.0	$0.915 \pm 0.019 \; {}^{+0.030}_{-0.044}$	0.920 ± 0.031
7.0–8.0	$0.917 \pm 0.020 \; {}^{+0.028}_{-0.050}$	0.922 ± 0.030
8.0–12.0	$0.873 \pm 0.029 \; {}^{+0.041}_{-0.051}$	0.880 ± 0.040
12.0–16.0	$0.908 \pm 0.025 \; {}^{+0.033}_{-0.062}$	0.913 ± 0.026

Table 11.2: Values of the combined results of the prompt fraction from this thesis $f_{\text{prompt}}^{\text{this thesis}}$ and from the results of [2] $f_{\text{prompt}}^{\text{CM}}$ with the associated total uncertainties for the analysis without topological selection.

11.4 Comparison between the results of both analyses

In this section the results of the analysis using topological selection cuts and of the non-topological analysis are compared. First, the similarities are discussed, subsequently, the differences.

The prompt fractions of the only FONLL-based method $f_{\text{prompt}}^{\text{FONLL}}$ are lower than the prompt fractions of the $f_{\text{prompt}}^{\text{data}}$ method including data of the raw yields. This effect was also observed when different measurements of the $c\bar{c}$ cross sections were compared to NLO-predictions assuming the same charm mass of 1.5 GeV/c^2 as the FONLL-predictions (see Fig. 11.5). All experimentally measured cross sections lie above the theoretically predicted cross sections of the pQCD calculation framework MNR [44]. This might indicate that the charm mass of 1.5 GeV/c^2 as assumed in the FONLL calculations is too large and leads to underestimated cross section predictions for the prompt D^0 mesons in this thesis. The actual average of the charm mass is 1.275 ± 0.025 GeV/c^2 [3].
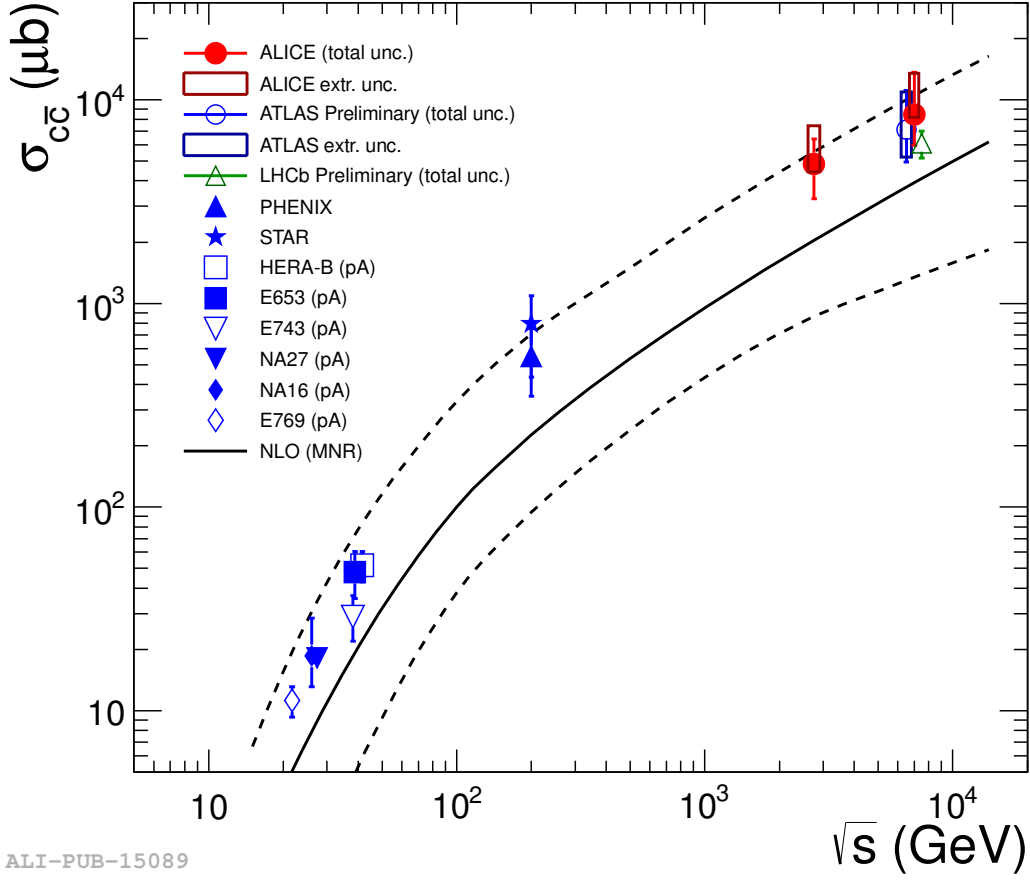
Figure 11.5: Comparison between measured $c\bar{c}$ cross sections at different $\sqrt{s}$ and NLO-predictions of the MNR framework [44] assuming the same charm mass $m_c = 1.5$ GeV/c^2 as the FONLL framework. Figure was taken from [45].

In both the analysis applying topological cuts and the analysis not using them, the prompt fraction decreases with increasing p_T. The B hadrons carry a larger fraction of the initial quark momentum than the prompt D^0 mesons. This can be seen by comparison of Fig. 5.4 and 5.5. The feeddown D^0 mesons carry on this shifting to higher transverse momenta of the B hadrons. This results in the decrease of the prompt fraction of D^0 mesons with increasing p_T.

Finally, the results of this thesis of both the analysis using topological selection $f_{\text{prompt}}^{\text{this thesis, top}}$ and the analysis not using topological selection $f_{\text{prompt}}^{\text{this thesis, non}-\text{top}}$ are depicted together in Fig. 11.6. The prompt fraction of the topologically selected

data is smaller compared to that of the data selected without topological cuts. When the events are selected without topological selections, the acceptance times efficiencies are the same for both feeddown and prompt D^0 mesons. By contrast, in the topological analysis the probability to detect and select a feeddown D^0 meson is up to 3 times higher than to detect and select a prompt D^0 meson. This is considered and corrected by the $\alpha \times \epsilon$ terms, but still the selection of feeddown events seems to be favored in the topological analysis.
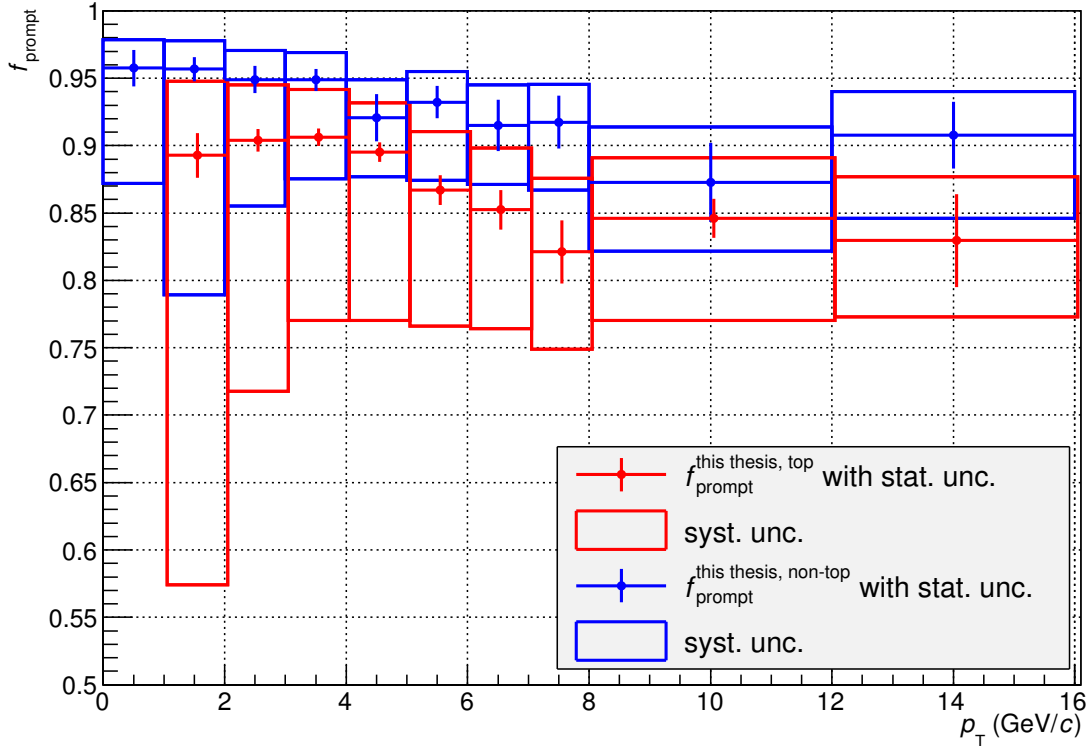
Figure 11.6: Comparison between the results of this thesis of both the topological and non-topological analysis. The bin centers of the prompt fraction $f_{\text{prompt}}^{\text{this thesis, top}}$ is slightly shifted to the right for better visibility.

Comparing the uncertainties of the different p_{T} intervals, the upper relative systematic uncertainties of the topological analysis are up to three times as large as those of the non-topological analysis. This effect is attributed to the higher $(\alpha \times \epsilon)_{\text{fd}}$ that enlarge the systematic uncertainties of the feeddown contributions. The lower relative systematic uncertainties in the p_{T}-range of 1–7 GeV/c in the non-topological analysis are half as large as those in the topological analysis. In this range the ratio

of $\frac{(\alpha \times \epsilon)_{\text{fd}}}{(\alpha \times \epsilon)_{\text{pr}}}$ is about 2. At higher $p_{\text{T}} > 8$ GeV/c, the differences between the relative lower systematic uncertainties of the different analyses slowly subside as the ratio of the different efficiency corrections $\frac{(\alpha \times \epsilon)_{\text{fd}}}{(\alpha \times \epsilon)_{\text{pr}}}$ of the topological analysis decreases.

12 Conclusion and Outlook

This thesis centered on the determination of the prompt fraction of D^0 mesons from data recorded with the ALICE detector in proton-proton collisions at $\sqrt{s} = 7$ TeV. This work focused on the influence and propagation of the different uncertainties of the prompt fraction of D^0 mesons. Special attention was paid to the propagation of the systematic uncertainties due to the FONLL predictions. The correlations between the different FONLL uncertainty sources were considered and the uncertainties were combined consistently with the FONLL uncertainty propagation. The prompt fraction of D^0 mesons was determined for topological and non-topological analyses. For the topological analysis the published results were reproduced to be able to compare them to the results of this thesis.

The reproduced prompt fraction with the associated uncertainties is in good agreement with the published results. The central values and upper systematic uncertainties of the prompt fractions determined in this thesis are consistent with those given in [1] and [2]. The lower systematic uncertainties of the topological analysis could be significantly reduced from 45% to 36% in the p_T-range of 1–2 GeV/c. The systematic uncertainties of the non-topological analysis were propagated consistently with those of the topological analysis. The lower systematic uncertainties of the non-topological analysis were enlarged by this correction compared to those given in [2]. In the overall comparison the prompt fraction of the non-topological analysis in this thesis carried significantly smaller systematic uncertainties than that of the topological analysis in this thesis.

For subsequent determinations of the prompt fraction a consistent uncertainty propagation technique should be chosen to obtain comparable results. Furthermore it would be interesting to perform an alternative topological selection of the data. An upper cut should be implemented to minimize the contribution from the feeddown D^0 mesons as the decay length of the prompt D^0 mesons differs signifcantly from the decay lengths of the B mesons.

A Tables of LCG values of B admixture at different numbers of trials

p_{T} range (GeV/c)	LCG (counts)	ΔLCG (counts)	$\Delta\left(\frac{\mathrm{LCG}}{\mathrm{FONLL}}\right)_{\mathrm{exp}}$ (%)	$\left\|1-\left(\frac{\mathrm{LCG}}{\mathrm{FONLL}}\right)\right\|$ (%)
$0.0-0.5$	13398	115.75	0.86	0.85
$0.5-1.0$	36254	190.40	0.53	0.39
$1.0-1.5$	56939	238.62	0.42	0.15
$1.5-2.0$	67964	260.70	0.38	0.02
$2.0-2.5$	74720	273.35	0.37	0.08
$2.5-3.0$	77385	278.18	0.36	0.64
$3.0-3.5$	75265	274.34	0.36	0.04
$3.5-4.0$	70911	266.29	0.38	0.09
$4.0-4.5$	65206	255.35	0.39	0.11
$4.5-5.0$	58773	242.43	0.41	0.39
$5.0-5.5$	51339	226.58	0.44	0.94
$5.5-6.0$	45414	213.11	0.47	0.08
$6.0-6.5$	39358	198.39	0.50	0.22
$6.5-7.0$	34017	184.44	0.54	0.30
$7.0-7.5$	29435	171.57	0.58	0.01
$7.5-8.0$	25134	158.54	0.63	0.88
$8.0-8.5$	21784	147.59	0.68	0.29
$8.5-9.0$	18980	137.77	0.73	0.76
$9.0-9.5$	16463	128.31	0.78	1.22
$9.5-10.0$	14060	118.57	0.84	0.05
$10.0-10.5$	12157	110.26	0.91	0.29
$10.5-11.0$	10775	103.80	0.96	1.72
$11.0-11.5$	9021	94.98	1.05	2.22
$11.5-12.0$	7963	89.24	1.12	1.15
$12.0-12.5$	7107	84.30	1.19	0.78
$12.5-13.0$	6330	79.56	1.26	2.27
$13.0-13.5$	5475	73.99	1.35	0.53
$13.5-14.0$	4718	68.69	1.46	1.77
$14.0-14.5$	4289	65.49	1.53	1.05
$14.5-15.0$	3791	61.57	1.62	0.85
$15.0-15.5$	3317	57.59	1.74	0.63
$15.5-16.0$	2921	54.05	1.85	1.70

Table A.1: Values for Fig. 7.1. LCG gives the number N of events per bin, ΔLCG gives the $\sqrt{N}$, $\Delta\left(\frac{\mathrm{LCG}}{\mathrm{FONLL}}\right)_{\mathrm{exp}} = \frac{\sqrt{N}}{N}$ gives an approach for the 1σ range of an ideal distribution in percent and $\left|1-\left(\frac{\mathrm{LCG}}{\mathrm{FONLL}}\right)\right|$ is the deviation of the actual LCG/FONLL ratio from 1 in percent. Number of trials: 10^6.

p_T range	LCG	ΔLCG	$\Delta\left(\frac{\mathrm{LCG}}{\mathrm{FONLL}}\right)_{\mathrm{exp}}$	$\left|1-\left(\frac{\mathrm{LCG}}{\mathrm{FONLL}}\right)\right|$
(GeV/c)	(counts)	(counts)	(%)	(%)
$0.0-0.5$	$1.35226E+06$	1162.9	0.086	0.073
$0.5-1.0$	$3.60897E+06$	1899.7	0.053	0.064
$1.0-1.5$	$5.70660E+06$	2388.8	0.042	0.077
$1.5-2.0$	$6.79249E+06$	2606.2	0.038	0.037
$2.0-2.5$	$7.47428E+06$	2733.9	0.037	0.054
$2.5-3.0$	$7.69040E+06$	2773.2	0.036	0.012
$3.0-3.5$	$7.52399E+06$	2743.0	0.036	0.003
$3.5-4.0$	$7.09495E+06$	2663.6	0.038	0.036
$4.0-4.5$	$6.51150E+06$	2551.8	0.039	0.033
$4.5-5.0$	$5.85465E+06$	2419.6	0.041	0.001
$5.0-5.5$	$5.18277E+06$	2276.6	0.044	0.007
$5.5-6.0$	$4.54140E+06$	2131.1	0.047	0.079
$6.0-6.5$	$3.94349E+06$	1985.8	0.050	0.021
$6.5-7.0$	$3.41256E+06$	1847.3	0.054	0.019
$7.0-7.5$	$2.94399E+06$	1715.8	0.058	0.028
$7.5-8.0$	$2.53571E+06$	1592.4	0.063	0.002
$8.0-8.5$	$2.18291E+06$	1477.5	0.068	0.079
$8.5-9.0$	$1.88367E+06$	1372.5	0.073	0.000
$9.0-9.5$	$1.62537E+06$	1274.9	0.078	0.062
$9.5-10.0$	$1.40726E+06$	1186.3	0.084	0.044
$10.0-10.5$	$1.21789E+06$	1103.6	0.091	0.113
$10.5-11.0$	$1.05931E+06$	1029.2	0.097	0.001
$11.0-11.5$	$9.22251E+05$	960.3	0.104	0.041
$11.5-12.0$	$8.06257E+05$	897.9	0.111	0.087
$12.0-12.5$	$7.06008E+05$	840.2	0.119	0.115
$12.5-13.0$	$6.20336E+05$	787.6	0.127	0.221
$13.0-13.5$	$5.44943E+05$	738.2	0.135	0.060
$13.5-14.0$	$4.81189E+05$	693.7	0.144	0.187
$14.0-14.5$	$4.24962E+05$	651.9	0.153	0.123
$14.5-15.0$	$3.75312E+05$	612.6	0.163	0.155
$15.0-15.5$	$3.33345E+05$	577.4	0.173	0.138
$15.5-16.0$	$2.97940E+05$	545.8	0.183	0.260

Table A.2: Values for Fig. 7.2. LCG gives the number N of events per bin, ΔLCG gives the $\sqrt{N}$, $\Delta\left(\frac{\mathrm{LCG}}{\mathrm{FONLL}}\right)_{\mathrm{exp}} = \frac{\sqrt{N}}{N}$ gives an approach for the 1σ range of an ideal distribution in percent and $\left|1-\left(\frac{\mathrm{LCG}}{\mathrm{FONLL}}\right)\right|$ is the deviation of the actual LCG/FONLL ratio from 1 in percent. Number of trials: 10^8.

B Decay tables of the B hadrons from the PYTHIA database

	decay channel	$\mathcal{B}$
semileptonic decays:	$D^- \, e^+ \nu_e$	0.0200
	$D^{*-} e^+ \nu_e$	0.0550
	$D_1^- \, e^+ \nu_e$	0.0050
	$D_0^{*-} e^+ \nu_e$	0.0050
	$D_1^{*-} e^+ \nu_e$	0.0080
	$D_2^{*-} e^+ \nu_e$	0.0120
	$D^- \, \mu^+ \nu_\mu$	0.0200
	$D^{*-} \mu^+ \nu_\mu$	0.0550
	$D_1^- \, \mu^+ \nu_\mu$	0.0050
	$D_0^{*-} \mu^+ \nu_\mu$	0.0050
	$D_1^{*-} \mu^+ \nu_\mu$	0.0080
	$D_2^{*-} \mu^+ \nu_\mu$	0.0120
	$D^- \, \tau^+ \nu_\tau$	0.0100
	$D^{*-} \tau^+ \nu_\tau$	0.0300
two-body decays:	$D^- \, \pi^+$	0.0035
	$D^- \, \rho^+$	0.0110
	$D^- \, a_1^+$	0.0055
	$D^{*-} \pi^+$	0.0042
	$D^{*-} \rho^+$	0.0090
	$D^{*-} a_1^+$	0.0180
	$D^- \, D_s^+$	0.0150
	$D^- \, D_s^{*+}$	0.0185
	$D^{*-} D_s^+$	0.0135
	$D^{*-} D_s^{*+}$	0.0250
	$\eta_c \, K^0$	0.0004
	$\eta_c \, K^{*0}$	0.0007
	$J/\psi \, K^0$	0.0008
	$J/\psi \, K^{*0}$	0.0014
	$\chi_{c1} \, K^0$	0.0019
	$\chi_{c1} \, K^{*0}$	0.0025
more-body decays:	$u \, \overline{d} \, \overline{c} \, d$	0.4291
	$u \, \overline{c} \, \overline{d} \, d$	0.0800
	$c \, \overline{s} \, \overline{c} \, d$	0.0700
	$c \, \overline{c} \, \overline{s} \, d$	0.0200
	$u \, \overline{d} \, \overline{u} \, d$	0.0150
	$c \, \overline{s} \, \overline{u} \, d$	0.0050

Further decays of B^0 decay products producing D mesons or D resonances:

mother particle	decay channel	$\mathcal{B}$
D^{*-}	$\overline{D^0} \, \pi^-$	0.683
	$D^- \, \pi^0$	0.306
	$D^- \, \gamma$	0.011
D_1^-	$\overline{D^{*0}} \, \pi^-$	0.667
	$D^{*-} \pi^0$	0.333
D_0^{*-}	$\overline{D^0} \, \pi^-$	0.667
	$D^- \, \pi^0$	0.333
D_1^{*-}	$\overline{D^{*0}} \, \pi^-$	0.667
	$D^{*-} \pi^0$	0.333
D_2^{*-}	$\overline{D^0} \, \pi^-$	0.300
	$D^- \, \pi^0$	0.150
	$\overline{D^{*0}} \, \pi^-$	0.160
	$D^{*-} \pi^0$	0.080
	$\overline{D^{*0}} \, \pi^- \pi^0$	0.130
	$D^{*-} \pi^- \pi^+$	0.060
	$\overline{D^0} \, \pi^- \pi^0$	0.080
	$D^- \, \pi^- \pi^+$	0.040

Table B.1: Mother particle: B^0, mass in database: 5.2792GeV/c, PDG-code: 511.

	decay channel	$\mathcal{B}$
semileptonic decays:	$\overline{D^0}\ e^+\nu_e$	0.0200
	$\overline{D^{*0}}\ e^+\nu_e$	0.0550
	$\overline{D_1^0}\ e^+\nu_e$	0.0050
	$\overline{D_0^{*0}}\ e^+\nu_e$	0.0050
	$\overline{D_1^{*0}}\ e^+\nu_e$	0.0080
	$\overline{D_2^{*0}}\ e^+\nu_e$	0.0120
	$\overline{D^0}\ \mu^+\nu_\mu$	0.0200
	$\overline{D^{*0}}\ \mu^+\nu_\mu$	0.0550
	$\overline{D_1^0}\ \mu^+\nu_\mu$	0.0050
	$\overline{D_0^{*0}}\ \mu^+\nu_\mu$	0.0050
	$\overline{D_1^{*0}}\ \mu^+\nu_\mu$	0.0080
	$\overline{D_2^{*0}}\ \mu^+\nu_\mu$	0.0120
	$\overline{D^0}\ \tau^+\nu_\tau$	0.0100
	$\overline{D^{*0}}\ \tau^+\nu_\tau$	0.0300
two-body decays:	$\overline{D^0}\ \pi^+$	0.0035
	$\overline{D^0}\ \rho^+$	0.0110
	$\overline{D^0}\ a_1^+$	0.0055
	$\overline{D^{*0}}\pi^+$	0.0042
	$\overline{D^{*0}}\rho^+$	0.0090
	$\overline{D^{*0}}a_1^+$	0.0180
	$\overline{D^0}\ D_s^+$	0.0150
	$\overline{D^0}\ D_s^{*+}$	0.0185
	$\overline{D^{*0}}\ D_s^+$	0.0135
	$\overline{D^{*0}}\ D_s^{*+}$	0.0250
	$\eta_c\ K^+$	0.0004
	$\eta_c\ K^{*+}$	0.0007
	$J/\psi\ K^+$	0.0008
	$J/\psi\ K^{*+}$	0.0014
	$\chi_{c1}\ K^+$	0.0019
	$\chi_{c1}\ K^{*+}$	0.0025
more-body decays:	$u\,\overline{d}\,\overline{c}\,u$	0.4291
	$u\,\overline{c}\,\overline{d}\,u$	0.0800
	$c\,\overline{s}\,\overline{c}\,u$	0.0700
	$c\,\overline{c}\,\overline{s}\,u$	0.0200
	$u\,\overline{d}\,\overline{u}\,u$	0.0150
	$c\,\overline{s}\,\overline{u}\,u$	0.0050

Further decays of B^+ decay products producing D mesons or D resonances:

mother particle	decay channel	$\mathcal{B}$
$\overline{D^{*0}}$	$\overline{D^0}\ \pi^0$	0.619
	$\overline{D^0}\ \gamma$	0.381
$\overline{D_1^0}$	$D^{*-}\ \pi^+$	0.667
	$\overline{D^{*0}}\ \pi^0$	0.333
$\overline{D_0^{*0}}$	$D^-\ \pi^+$	0.667
	$\overline{D^0}\ \pi^0$	0.333
$\overline{D_1^{*0}}$	$D^{*-}\ \pi^-$	0.667
	$\overline{D^{*0}}\ \pi^0$	0.333
$\overline{D_2^{*0}}$	$D^-\ \pi^+$	0.300
	$\overline{D^0}\ \pi^0$	0.150
	$D^{*-}\ \pi^+$	0.160
	$\overline{D^{*0}}\ \pi^0$	0.080
	$D^{*-}\ \pi^+\pi^0$	0.130
	$\overline{D^{*0}}\ \pi^-\pi^+$	0.060
	$D^-\ \pi^+\pi^0$	0.080
	$\overline{D^0}\ \pi^-\pi^+$	0.040

Table B.2: Mother particle: B^+, mass in database: 5.2789 GeV/c, PDG-code: 521.

	decay channel	$\mathcal{B}$
semileptonic decays:	$D_s^-\ e^+\nu_e$	0.0200
	$D_s^{*-}e^+\nu_e$	0.0550
	$D_{s1}^-\ e^+\nu_e$	0.0050
	$D_{s0}^{*-}e^+\nu_e$	0.0050
	$D_{s1}^{*-}e^+\nu_e$	0.0080
	$D_{s2}^{*-}e^+\nu_e$	0.0120
	$D_s^-\ \mu^+\nu_\mu$	0.0200
	$D_s^{*-}\mu^+\nu_\mu$	0.0550
	$D_{s1}^-\ \mu^+\nu_\mu$	0.0050
	$D_{s0}^{*-}\mu^+\nu_\mu$	0.0050
	$D_{s1}^{*-}\mu^+\nu_\mu$	0.0080
	$D_{s2}^{*-}\mu^+\nu_\mu$	0.0120
	$D_s^-\ \tau^+\nu_\tau$	0.0100
	$D_s^{*-}\tau^+\nu_\tau$	0.0300
two-body decays:	$D_s^-\ \pi^+$	0.0035
	$D_s^-\ \rho^+$	0.0110
	$D_s^-\ a_1^+$	0.0055
	$D_s^{*-}\pi^+$	0.0042
	$D_s^{*-}\rho^+$	0.0090
	$D_s^{*-}a_1^+$	0.0180
	$D_s^-\ D_s^+$	0.0150
	$D_s^-\ D_s^{*+}$	0.0185
	$D_s^{*-}D_s^+$	0.0135
	$D_s^{*-}D_s^{*+}$	0.0250
	$\eta_c\ \eta$	0.0002
	$\eta_c\ \eta'$	0.0002
	$\eta_c\ \phi$	0.0007
	$J/\psi\ \eta$	0.0004
	$J/\psi\ \eta'$	0.0004
	$J/\psi\ \phi$	0.0014
	$\chi_{c1}\ \eta$	0.0010
	$\chi_{c1}\ \eta'$	0.0009
	$\chi_{c1}\ K^{*0}$	0.0025
more-body decays:	$u\ \bar{d}\ \bar{c}\ s$	0.4291
	$u\ \bar{c}\ \bar{d}\ s$	0.0800
	$c\ \bar{s}\ \bar{c}\ s$	0.0700
	$c\ \bar{c}\ \bar{s}\ s$	0.0200
	$u\ \bar{d}\ \bar{u}\ s$	0.0150
	$c\ \bar{s}\ \bar{u}\ s$	0.0050

Further decays of B_s^0 decay products producing D mesons or D resonances:

mother particle	decay channel	$\mathcal{B}$
D_s^{*-}	$D_s^-\ \gamma$	0.940
	$D_s^-\ \pi^0$	0.060
D_{s1}^-	$\overline{D^{*0}}\ K^-$	0.500
	$D^{*-}\ \overline{K^0}$	0.500
D_{s0}^{*-}	$D^-\ \overline{K^0}$	0.500
	$\overline{D^0}\ K^-$	0.500
D_{s1}^{*-}	$\overline{D^{*0}}\ K^-$	0.500
	$D^{*-}\ \overline{K^0}$	0.500
D_{s2}^{*-}	$\overline{D^0}\ K^-$	0.400
	$D^-\ \overline{K^0}$	0.400
	$\overline{D^{*0}}\ K^-$	0.100
	$D^{*-}\ \overline{K^0}$	0.100

Table B.3: Mother particle: B_s^0, mass in database: 5.3693 GeV/c, PDG-code: 531.

	decay channel	$\mathcal{B}$
semileptonic decays:	$\Lambda_\mathrm{c}^+ \ \mathrm{e}^- \overline{\nu_\mathrm{e}}$	0.1050
	$\Lambda_\mathrm{c}^+ \ \mu^- \overline{\nu_\mu}$	0.1050
	$\Lambda_\mathrm{c}^+ \ \tau^- \overline{\nu_\tau}$	0.0400
two-body decays:	$\Lambda_\mathrm{c}^+ \ \pi^-$	0.0077
	$\Lambda_\mathrm{c}^+ \ \rho^-$	0.0200
	$\Lambda_\mathrm{c}^+ \ \mathrm{a}_1^-$	0.0235
	$\Lambda_\mathrm{c}^+ \ \mathrm{D}_\mathrm{s}^-$	0.0285
	$\Lambda_\mathrm{c}^+ \ \mathrm{D}_\mathrm{s}^{*-}$	0.0435
	$\eta_\mathrm{c} \ \Lambda^0$	0.0011
	$\mathrm{J}/\psi \ \Lambda^0$	0.0022
	$\chi_\mathrm{c1} \ \Lambda^0$	0.0044
more-body decays:	$\overline{\mathrm{u}} \ \mathrm{d} \ \mathrm{c} \ \mathrm{ud}_0$	0.4291
	$\overline{\mathrm{u}} \ \mathrm{c} \ \mathrm{d} \ \mathrm{ud}_0$	0.0800
	$\overline{\mathrm{c}} \ \mathrm{s} \ \mathrm{c} \ \mathrm{ud}_0$	0.0700
	$\overline{\mathrm{c}} \ \mathrm{c} \ \mathrm{s} \ \mathrm{ud}_0$	0.0200
	$\overline{\mathrm{u}} \ \mathrm{d} \ \mathrm{u} \ \mathrm{ud}_0$	0.0150
	$\overline{\mathrm{c}} \ \mathrm{s} \ \mathrm{u} \ \mathrm{ud}_0$	0.0050

Table B.4: Mother particle: Λ_b^0, mass in database: 5.641 MeV/c, PDG-code: 5122.

References

[1] ALICE Collaboration, B. Abelev et al. „Measurement of charm production at central rapidity in proton-proton collisions at $\sqrt{s} = 7$ TeV". In: *JHEP* **01**, 128 (2012). DOI: `10.1007/JHEP01(2012)128`. arXiv: `1111.1553`.

[2] C. Möhler. „D-meson production at ultra-low transverse momentum in proton-proton collisions with ALICE at the LHC". Master Thesis. University of Heidelberg, 2014. URL: `http://www.physi.uni-heidelberg.de//Publications/master_thesis_Moehler.pdf`.

[3] Particle Data Group, K. A. Olive et al. „Review of Particle Physics". In: *Chin. Phys.* **C38**, 090001 (2014). and 2015 update.

[4] M. Thomson. *Modern particle physics.* Cambridge University Press, 2013. ISBN: 978-1-107-03426-6.

[5] R. Averbeck. „Heavy-flavor production in heavy-ion collisions and implications for the properties of hot QCD matter". In: *Prog. Part. Nucl. Phys.* **70** (2013), pp. 159–209. DOI: `10.1016/j.ppnp.2013.01.001`.

[6] ALICE Collaboration. „Performance of the ALICE Experiment at the CERN LHC". In: *Int. J. Mod. Phys.* **A 29**, 1430044 (2014), p. 120. DOI: `10.1142/S0217751X14300440`. arXiv: `1402.4476v3 [nucl-ex]`.

[7] ALICE Collaboration, B. Alessandro et al. „ALICE: Physics Performance Report, Volume II". In: *J. Phys.* **G32**, 10 (2006), p. 1295. DOI: `10.1088/0954-3899/32/10/001`.

[8] ALICE Collaboration, K. Aamodt et al. „The ALICE experiment at the CERN LHC". In: *J. Inst.* **3**, S08002 (2008). DOI: `10.1088/1748-0221/3/08/S08002`.

[9] Particle Data Group, C. Amsler et al. „Review of Particle Physics". In: *Phys. Lett.* **B667**, 1 (2008). and 2009 partial update for the 2010 edition.

[10] Particle Data Group, C. Amsler et al. „Fragmentation functions in e$^+$e$^-$ annihilation and lepton-nucleon DIS". In: *Phys. Lett.* **B667** (2008), pp. 202–211.

[11] LHCb Collaboration, R. Aaij et al. *Measurements of prompt charm production cross-sections in pp collisions at $\sqrt{13}$ TeV.* 2015. arXiv: `1510.01707 [hep-ex]`.

[12] M. Lisovyi, A. Verbytskyi, and O. Zenaiev. *Combined analysis of charm-quark fragmentation-fraction measurements.* 2015. arXiv: `1509.01061v1 [hep-ex]`.

[13] K. Schweda. „Prompt production of D mesons with ALICE at the LHC". Habilitation Thesis. University of Heidelberg, 2013. arXiv: `1402.1370` [`nucl-ex`].

[14] M. Cacciari. *FONLL Heavy Quark Production*. URL: `http://www.lpthe.jussieu.fr/~cacciari/fonll/fonllform.html`.

[15] H. Cakir. „Precise Determination of the $c\bar{c}$ Cross Section in proton-proton Collision at $\sqrt{s} = 7$ TeV". Bachelor Thesis. University of Heidelberg, 2013. URL: `http://www.physi.uni-heidelberg.de//Publications/cakir_bachelor_thesis.pdf`.

[16] P. Nason, S. Dawson, and R.K. Ellis. „The total cross section for the production of heavy quarks in hadronic collisions". In: *Nucl. Phys.* **B303** (1988), pp. 607–633.

[17] P. Nason, S. Dawson, and R.K. Ellis. „The one particle inclusive differential cross section for heavy quark production in hadronic collisions". In: *Nucl. Phys.* **B327** (1989). pp. 49-92. Erratum, Nucl. Phys. B335 pp. 260 ff (1990).

[18] M. Cacciari et al. S. P. Baranov. *Heavy Quarks: Summary Report. Theoretical review of various approaches in heavy quark production.* 2006. arXiv: `hep-ph/0601164`.

[19] M. Cacciari and M. Greco. „Large p_T hadroproduction of heavy quarks". In: *Nucl.Phys.* **B421** (1994), pp. 530–544. arXiv: `hep-ph/9311260`.

[20] M. Cacciari, M. Greco, and P. Nason. „The p_T spectrum in heavy-flavour hadroproduction". In: *JHEP* **007**, 9805 (1998). DOI: `10.1088/1126-6708/1998/05/007`. arXiv: `hep-ph/9803400`.

[21] M. Cacciari, M. Greco, and P. Nason. „The p_T spectrum in heavy-flavour photoproduction". In: *JHEP* **006**, 0103 (2001). arXiv: `hep-ph/0102134`.

[22] V. G. Kartvelishvili, A. K. Likhoded, and V. A. Petrov. „On the fragmentation functions of heavy quarks into hadrons". In: *Phys. Lett.* **B78**, 615 (1978). DOI: `doi:10.1016/0370-2693(78)90653-6`.

[23] M. Cacciari, P. Nason, and C. Oleari. „A Study of Heavy Flavoured Meson Fragmentation Functions in e+ e- annihilation". In: *JHEP* **006**, 0604 (2006). DOI: `10.1088/1126-6708/2006/04/006`. arXiv: `hep-ph/0510032v1`.

[24] ALEPH Collaboration, R. Barate et al. „Study of Charm Production in Z Decays". In: *Eur.Phys.J.* **C16** (2000), pp. 597–611. DOI: `10.1007/s100520000421`. arXiv: `hep-ex/9909032`.

[25] E. Braaten et al. „Perturbative QCD Fragmentation Functions as a Model for Heavy-Quark Fragmentation". In: *Phys.Rev.* **D51** (1995), pp. 4819–4829. DOI: 10.1103/PhysRevD.51.4819. arXiv: hep-ph/9409316.

[26] E. Braaten, K. Cheung, and T. C. Yuan. „QCD fragmentation functions for B_c and B_c^+ production". In: *Phys. Rev.* **D48**, R5049 (1993).

[27] M. Cacciari et al. „Theoretical predictions for charm and bottom production at the LHC". In: *JHEP* **1210**, 137 (2012). arXiv: 1205.6344 [hep-ph].

[28] M. Cacciari and P. Nason. „Charm Cross Sections for the Tevatron Run II". In: *JHEP* **0309**, 006 (2003). DOI: 10.1088/1126-6708/2003/09/006. arXiv: hep-ph/0306212.

[29] Particle Data Group, K. Hagiwara et al. „Review of Particle Physics". In: *Phys. Rev.* **D66**, 010001 (2002).

[30] M. Figueredo. *private communication.*

[31] K. Schweda. *private communication.*

[32] F. Prino. *private communication.*

[33] F. James. „A review of pseudorandom number generators". In: *Comput. Phys. Commun.* **60** (1990), pp. 329–344. DOI: 10.1016/0010-4655(90)90032-V.

[34] A. Rathi, D. Sharma, and T. Bhardwaj. *A Dissection of Pseudorandom number Generators.* 2nd International Conference on Signal Processing and Integrated Networks (SPIN), 2015. DOI: 10.1109/SPIN.2015.7095369.

[35] M. Matsumoto and T. Nishimura. „Mersenne Twister: A623-dimensionally equidistributed uniform pseudo-random number generator". In: *ACM Trans. Model. Comput. Simul.* **8**, 1 (1998), pp. 3–30.

[36] *ROOT framework Reference Guide, subversion 6.04.* URL: https://root.cern.ch/root/html604/ClassIndex.html.

[37] T. Sjöstrand et al. „Pythia 6.4 physics and manual". In: *JHEP* **0605**, 026 (2006). LU TP 06-13, FERMILAB-PUB-06-052-CD-T. arXiv: hep-ph/0603175.

[38] G. Marsaglia, A. Zaman, and W. W. Tsang. „Toward a universal random number generator". In: *Stat. Prob. Lett.* **9**, Issue 1 (1990), pp. 35–39. DOI: 10.1016/0167-7152(90)90092-L.

[39] F. B. Schäfer. „Polarization Effects on Detector Acceptance in D^{*+}(2010) $\rightarrow$ D^0(K$^-\pi^+$)+π^+". Bachelor Thesis. University of Heidelberg, 2012. URL: http://www.physi.uni-heidelberg.de//Publications/120912_BA_fs.pdf.

[40] D. J. Lange. „The EvtGen particle decay simulation package". In: *Nucl. Instrum. Meth.* **A462** (2001), pp. 152–155.

[41] Particle Data Group, K. Nakamura et al. „Review of Particle Physics". In: *J. Phys.* **G37**, 075021 (2010). and 2011 partial update for the 2012 edition.

[42] C. Möhler. *private communication.*

[43] Particle Data Group, K. A. Olive et al. „Review of Particle Physics". In: *Chin. Phys.* **C38**, 090001 (2014). DOI: 10.1088/1674-1137/38/9/090001.

[44] M. Mangano, P. Nason, and G. Ridolfi. „Heavy-quark correlations in hadron collisions at next-to-leading order". In: *Nucl. Phys.* **B373** (1992), pp. 295–345. DOI: 10.1016/0550-3213(92)90435-E.

[45] ALICE Collaboration, B. Abelev et al. „Measurement of charm production at central rapidity in proton-proton collisions at $\sqrt{s} = 2.76$ TeV". In: *JHEP* **07**, 191 (2012). DOI: 10.1007/JHEP07(2012)191. arXiv: 1205.4007.

Acknowledgements

Erklärung

Ich versichere, dass ich diese Arbeit selbstständig verfasst und keine anderen als die angegebenen Quellen und Hilfsmittel benutzt habe.

Heidelberg, den _____,